CHARACTERIZING TURBULENT EXCHANGE OVER A HETEROGENEOUS URBAN LANDSCAPE

by

Caitlin Iris Semmens

B.A., The University of British Columbia, 2015

A THESIS SUBMITTED IN PARTIAL FULFILLMENT OF

THE REQUIREMENTS FOR THE DEGREE OF

MASTER OF SCIENCE

in

THE FACULTY OF GRADUATE AND POSTDOCTORAL STUDIES

(Geography)

THE UNIVERSITY OF BRITISH COLUMBIA

(Vancouver)

August 2017

Abstract

Much of the world's population now resides within cities where altered energy use, building distributions, transportation networks, and surface characteristics influence land-atmosphere interactions, energy and water budgets, and carbon cycles, relative to rural areas. Knowledge of the surface properties that affect exchanges of energy and mass, as well as how exchanges change over time, is critical for accurate local weather and climate forecasting, and pollution dispersion modelling. One way of measuring flows of energy and mass over cities is through the use of eddy covariance (EC). This stationary approach has been implemented in many cities globally, and has contributed greatly to knowledge of the exchange between the urban surface and the urban atmosphere. However, EC was developed for ecosystems like forests, where source/sink distributions are horizontally homogeneous; This surface uniformity does not usually pertain to cities, where sources of heat, water, momentum, and trace gases exhibit spatial heterogeneity.

Eight years (2008 - 2016) of continuous EC flux measurements over a residential neighbourhood in Vancouver, BC, Canada, were used to characterize the relationship between surface source/sink heterogeneity and the efficiency of turbulent exchange of heat, water vapour, momentum, and carbon dioxide (CO_2) (represented by the correlation coefficients r_{wT}, r_{wh}, r_{uw}, and r_{wc}, respectively). Using a combination of remotely-sensed satellite and light detection and ranging (LiDAR) imagery, geospatially-referenced land cover data, traffic densities, and source area modelling, exchange efficiencies were examined seasonally, diurnally, as a function of atmospheric stability, and in terms of distinct, spatially-variable surface cover attributes.

Transport of momentum and scalars exhibited varied dependencies that resulted in dissimilar exchange efficiencies; r_{wT} was primarily moderated by stability, time of day and year, and surface patchiness, r_{uw} was mostly affected by stability and surface roughness, and r_{wh} and r_{wc} were mostly

affected by surface patchiness. As source/sink heterogeneity increased, exchange became less efficient. Competing sources and sinks acting simultaneously on a turbulent entity resulted in an exchange efficiency closer to zero. Under stable conditions, r_{wT}, r_{wh}, r_{uw}, and r_{wc} depended mostly on stability, while surface heterogeneity contributed more to dissimilarities between momentum and scalar exchange efficiencies under unstable conditions.

Lay Summary

Surface distributions of sources and sinks of heat, water, momentum, and carbon dioxide (CO_2) are patchy in cities compared to rural areas. This patchiness creates dissimilarities in how efficiently these entities are transported in the atmosphere. However, models that predict and forecast urban weather and pollution dispersion assume that these turbulent entities are transported equally efficiently. Furthermore, the eddy covariance method used to measure their flow in the atmosphere assumes that sources and sinks are uniformly distributed at the surface, which is not typical of cities. The goal of this research is to characterize the relationship between the efficiency with which heat, moisture, momentum, and CO_2 are transported in the atmosphere, and the temporally and spatially-variable sources and sinks of these entities at the surface of an urban area. This will enhance knowledge of the complex surface-atmosphere interactions over cities, and inform better weather and pollution models.

Preface

The original work presented in this thesis was made possible through contributions by researchers involved in the Environmental Prediction in Canadian Cities (EPiCC) project, and through funding from the Canadian Foundation for Climate and Atmospheric Sciences (CFCAS) and the NSERC DG "Direct measurement of greenhouse gas exchange in urban ecosystems" (PI: A. Christen). LiDAR and satellite imagery used in the calculation of plan area cover for the study site was provided by Goodwin et al. (2009), Tooke et al. (2009), and van der Laan et al. (2010). Soil water content and vegetation data was collected by Christen et al. (2013) and Liss et al. (2010). Traffic count data was measured by the City of Vancouver and compiled and gridded by Christen et al. (2011). Aerodynamic roughness lengths were determined based on a previous study conducted in the Vancouver-Sunset study area by Grimmond et al. (1998). And the zero-plane displacement height used in the calculation of atmospheric stability was based on LES simulations of Vancouver-Sunset by Giometto et al. (2017).

The eddy covariance (EC) tower and instrumentation which provided the flux data used in this work was implemented by T.R. Oke, and A. Christen. The code that calculates the source area was written by A. Christen (Christen et al., 2011), and adapts the analytical flux footprint model created by Kormann and Meixner (2001). Further, the program that calculates the footprint-averaged surface cover fraction was written by A. Christen. The code used to read meteorological and flux data from the study site (Vancouver-Sunset), process raw data into 30-minute aggregated averages, and select and stratify for certain conditions was written by A. Christen, with some additional processes incorporated by me. Subsequent programs that use this code to perform the analyses and output the graphics presented in this thesis were written by me, with occasional input and supervision by A. Christen. My supervisor, A. Christen, was primarily responsible for conception of the broader research topic, and I established the scope and focus of the research presented herein. All data analyses were performed by me, and all figures and table (unless otherwise stated), are solely my work.

Table of Contents

List of Tables

List of Figures

List of Symbols and Acronyms

Symbol	Definition	Units
a.g.l.	Above ground level	
A_i	Normalized standard deviation of some turbulent entity (i)	
a_i	MOS-predicted semi-empirical constant	
B	Bowen ratio	
BC	British Columbia	
b_i	MOS-predicted semi-empirical constant	
c	Instantaneous carbon dioxide mixing ratio	μmol mol^{-1}
c'	Fluctuation of carbon dioxide mixing ratio	μmol mol^{-1}
Ca-VSu	Fluxnet ID for the EC tower at the Vancouver-Sunset study site	
c_i	MOS-predicted semi-empirical constant	
CNF	Cumulative normalized contribution to flux measurements	
CO_2	Carbon dioxide	
c_p	Specific heat of air	J kg^{-1} K^{-1}
ΔS_0	Difference of flux fraction of sweeps and flux fraction of ejections	
EC	Eddy covariance	
F_C	Carbon dioxide flux density	μmol m^{-2} s^{-1}
ϕ	Source area weighting	%
g	Acceleration due to gravity	m s^{-2}
GHG	Greenhouse gas	
h	Atmospheric water vapour density	g m^{-3}
h'	Fluctuation of water vapour density	g m^{-3}
H	Hole size	
H_b	Mean building height	m
HDD	Heating Degree Day	°C
IDL	Interactive Data Language (programming language)	
IPCC	International Panel on Climate Change	
ISL	Inertial sublayer	

κ	von Karman constant	
K_{down}	Incoming (downwelling) shortwave radiation	W m^{-2}
L	Obukhov length	m
λ	Plan-area cover	%
LCZ	Local Climate Zone	
LES	Large eddy simulation	
LiDAR	Light Detection and Ranging	
L_v	Latent heat of vapourization	J kg^{-1}
MOS	Monin-Obukhov similarity theory	
Q_E	Latent heat flu density	W m^{-2}
Q_H	Sensible heat flux density	W m^{-2}
R_{net}	Net all-wave radiation	W m^{-2}
RSL	Roughness sublayer	
r_{Th}	Correlation coefficient for temperature and humidity	
r_{uw}	Correlation coefficient for momentum	
r_{wc}	Correlation coefficient for CO_2	
r_{wh}	Correlation coefficient for water vapour	
r_{wT}	Correlation coefficient for sensible heat	
ρ	Density of dry air	kg m^{-3}
ρ_{CO_2}	Density of carbon dioxide	kg m^{-3}
PST	Pacific Standard Time	
ρ_v	Density of water vapour	kg m^{-3}
σ_i	Standard deviation of some turbulent entity (i)	
T	Air temperature (acoustic) from sonic anemometer	ºC
T_a	Flux averaging period	
T'	Fluctuation of acoustic air temperature	ºC
θ_*	Frictional temperature	ºC
u_*	Friction velocity	m s^{-1}
u	Instantaneous horizontal wind velocity component	m s^{-1}
u'	Fluctuation of horizontal wind velocity component	m s^{-1}
u_E	Instantaneous easting wind velocity component	m s^{-1}
u_N	Instantaneous northing wind velocity component	m s^{-1}

UHI	Urban heat island	
UN	United Nations	
$\overline{u'w'}$	Covariance of u' and w'	$m^2\ s^{-1}$
v	Instantaneous lateral wind velocity component	$m\ s^{-1}$
v'	Fluctuation of lateral wind velocity component	$m\ s^{-1}$
$\overline{v'w'}$	Covariance of v' and w'	$m^2\ s^{-1}$
w	Instantaneous vertical wind velocity component	$m\ s^{-1}$
w'	Fluctuation of vertical wind velocity component	$m\ s^{-1}$
$\overline{w'c'}$	Covariance of w' and c'	$\mu mol\ m^{-2}\ s^{-1}$
$\overline{w'h'}$	Covariance of w' and h'	$g\ m^{-2}\ s^{-1}$
$\overline{w'\rho'_{CO_2}}$	Covariance of w' and ${\rho_{CO_2}}'$	$kg\ m^{-2}\ s^{-1}$
$\overline{w'\rho_v{}'}$	Covariance of w' and ${\rho_v}'$	$kg\ m^{-2}\ s^{-1}$
$\overline{w'T'}$	Covariance of w' and T'	$K\ m^{-2}\ s^{-1}$
z	Measurement height	m
z'	Effective measurement height	m
z_d	Zero-plane displacement height	m
z_0	Roughness length	m
3D	Three-dimensional	

Acknowledgements

This thesis was made possible through contributions and support of many individuals. I am grateful to the Natural Sciences and Engineering Research Council of Canada (NSERC) for funding my work as a graduate student. Research funding was further supported by NSERC through a Discovery Grant to Andreas Christen. Funding from the Canadian Foundation for Climate and Atmospheric Sciences (CFCAS), NSERC, and the Canada Foundation for Innovation (CFI/BCKDF) made long-term data collection from the eddy covariance (EC) tower possible. I acknowledge BC Hydro for kindly hosting and granting access to the tower.

Long-term maintenance of the tower and data collection would not have been achieved without the expert technical and logistical support of the project manager, Rick Ketler, who was instrumental in ensuring accurate and continuous tower function and data acquisition. Invaluable technical support was also provided by B. Crawford, M. Giacchetto, C. Lefrancois, K. Liss and C. Siemens in helping to run the tower over the 2008 – 2016 period. The high-resolution remotely-sensed surface cover data used in this research was generously provided by N. Coops, N. Goodwin, R. Tooke, and M. van der Laan.

I am deeply grateful to my MSc supervisor, Andreas Christen, for his knowledgeable and devoted guidance throughout my post-graduate journey. Through his encouragement and inspiration, Andreas challenged me to expand my understanding of the physical sciences, and afforded me the opportunity to learn more in these past years than I ever would have imagined possible. His continuous support and patience as I learned how to use programming languages and work with massive datasets was of major benefit to me, and is sincerely appreciated. I was also very fortunate to receive thoughtful feedback and direction from Ian McKendry during the formation of my thesis topic.

Dedication

I dedicate this thesis to my parents, whose unwavering support throughout my academic journey has allowed me to get to this point. To my mother, who always reminded me to recognize my strengths and overcome my weaknesses, and to my father, who taught me to never stop being curious and never stop moving forward, thank you.

Chapter 1: Introduction

Research on atmospheric turbulence has been ongoing for over 100 years. The intention of such research is to better understand the mechanisms and processes by which energy and mass moves, and the relationships between the surface and the atmosphere (Roth 2000). Less common are studies of the same genre over urban surfaces, although these are crucially important as over 54% of the world's population now lives within cities (UN 2014). Urban areas are not the focus of most turbulence research primarily because field experiments in these areas are inherently difficult but also because generalizations about turbulence in one city is not easily applicable to another (Roth 2000). Nevertheless, identifying the impact of urban areas on the local climate, and the global environment is becoming increasingly relevant.

A major portion of the anthropogenically enhanced greenhouse gases (GHG) in the global atmosphere originates from cities, and despite urban areas accounting for only 2% of all land, 30-40% of the world's anthropogenic emissions of CO_2 comes from cities (Satterthwaite 2008, Canadell et al., 2009, Gioli et al., 2012). In addition to alterations of the carbon cycle, surface-atmosphere interactions are significantly modified relative to rural areas, resulting primarily from energy use, building distribution, transportation networks, and altered surface characteristics (Velasco and Roth 2010). Within urban ecosystems, exchanges of heat, moisture, trace gases, and momentum are affected by urban form and function. Understanding what factors influence these properties, and how these exchanges change over time is essential for local weather forecasting, air pollution modelling, and predicting urban climates (Nordbo et al., 2013).

One way of directly measuring land-atmospheric interactions, and the movement, or flux, of the turbulent entities relevant to cities is to use the eddy covariance (EC) method. This stationary, tower-based approach has become the standard tool for monitoring the terrestrial carbon cycle, trace gas emissions, and the water balance, with over 500 towers in use globally, and at least 30 within urban areas (Moriwaki and Kanda 2006, Velasco and Roth 2010, Chen et al., 2011, Crawford 2014).

EC utilizes very fast measurements of momentum, heat, water vapour, and CO_2 fluxes, and couples two of these turbulent entities to determine the net flux between the turbulent source area and the atmosphere (Crawford and Christen 2015). However, the EC method was initially developed for ecosystems like forests, where the source area has a uniform, or homogeneous, distribution of sources and sinks at the surface (Moriwaki and Kanda 2006). This is not the case in urban ecosystems, where emission sources of heat, water, momentum, and trace gases vary both spatially and temporally (Crawford and Christen 2015). Nevertheless, properly describing the unique surface-atmosphere exchanges of heat, momentum, water vapour, and trace gases in cities is critical for urban-scale weather and air pollution forecasting, and to inform more energy-efficient urban planning processes (Nordbo et al., 2013, Crawford and Christen 2015).

1.1 Eddy covariance

1.1.1 Eddy covariance in an urban environment

The atmospheric boundary layer over cities is different compared to rural areas; Urban form influences the energetic characteristics of the surface due to the different radiative and moisture-holding properties of the materials, and differential exposure of the 3-dimensional (3D) surface to the sun. Urban function creates spatially and temporally variable sources and sinks of energy and mass distributions over the course of the day, and throughout the seasons. A well-documented example of how urban areas modify the atmosphere and climate is the urban heat island (UHI), where differences in land cover type, material, morphometry, and surface roughness in cities, compared to their rural counterparts, alter energy and radiation budgets at the surface (Oke 1982, Arnfield 2003, Stewart and Oke 2009).

Unlike rural areas, where the distribution of sources and sinks in the source area are more homogeneous and smooth, urban areas exhibit heterogeneity characterized by an array of roughness elements, such as tall buildings, urban canyons, and trees, and a spatially and temporally variable distribution of gases, heat, and water. This roughness, in conjunction with the urban heat island,

significantly influences turbulence over cities (Roth 2000). In pioneering work by Roth and Oke (1995), the spatial heterogeneity of heat and water was discussed, and the notion that while every surface may be a source of heat, not all surfaces are sources of water, was highlighted. This distinction emphasizes the need to better understand intra-urban variation of sources and sinks of energy, mass, and momentum at the surface.

The ability to pair turbulent statistics and observe their relationships provides a significant amount of information, and this is critical for accurate weather, climate, and air pollution models. Additionally, because EC towers are stationary, information on how, for example, heat and moisture vary can be analyzed in terms of time, representing not only a directional (spatial) analysis, but a temporal one as well (Stull 1988).

1.1.2 Current objectives of urban eddy covariance

Urban areas have seen an increase in flux tower use in an effort to better understand surface-atmosphere interactions and altered energy and mass budgets (Chen et al., 2011). Grimmond and Christen (2012) have identified the four main objectives of urban flux tower measurements:

1) Basic understanding of surface physics and energetics
2) Basic understanding of turbulence in cities
3) Verification of urban canopy parameterizations in weather forecast and air pollution models
4) Verification of GHG, pollutants, and anthropogenic heat emission inventories.

Urban EC typically focusses on the flux of sensible heat, water vapour, momentum, and in more recent years, CO_2 (Roth 2000). Studies on heat flux aim to understand and quantify the UHI, since its implications for heat stress, thermal comfort, and its contribution toward global-scale phenomena like climate change are significant (Hansen et al., 2001, Arnfield 2003, Stewart and Oke 2009, Mazhar et al., 2015). Studies on the urban water balance are also prevalent, especially as the impermeability of many

urban surfaces has consequences for storm-water management and flooding risks (Grimmond and Christen 2012).

Of further interest in urban studies is wind dynamics and urban design; Data on momentum exchange can be used to determine wind loads on buildings, and inform future urban development. Cermak et al. (1995) emphasized the importance of understanding thermal properties and turbulent flow processes in cities for considerations in urban design and management, as well as the effects of light winds on the transportation of traffic-related pollution or toxic gas spills.

The desire to understand and model pollution dispersion in cities has increased in recent years (Steyn 1992, Masson et al., 2002, Giometto et al., 2017). With CO_2 having the largest radiative forcing, and approximately 40% of global CO_2 coming from cities, the desire to properly monitor and quantify emissions is strong (Satterthwaite 2008, IPCC 2013). Subsequent near-surface dispersion modelling has been the focus of many studies, since people live within the urban canopy layer where most pollutants are found (Christen et al., 2007).

Despite the prevalence of urban eddy covariance studies, and their contributions toward informing strategies to mitigate climate change, informing sustainable urban design, understanding controls on pollution, and reducing health risks to urban inhabitants, there exist some limitations when deploying EC studies in urban areas.

1.2 Limitations of EC in cities

Eddy covariance relies on three main assumptions (Nordbo et al., 2013):

1) Flow in the atmosphere is stationary (turbulent characteristics are independent of time)
2) The surface is horizontally homogeneous
3) Fluxes are constant with height in the inertial sublayer (ISL), where measurements are made.

Over urban surfaces and within the roughness sublayer (RSL) these assumptions generally do not hold true. Turbulence in urban areas is affected by the formation of wakes and form drag from roughness

elements, and heterogeneous distributions of sources and sinks which results in spatial and temporal mismatch between momentum and scalars (heat, water vapour, and trace gases) (Roth 2000). For example, vegetation may act as a net sink for CO_2 during the day and during certain seasons when it is photosynthetically active, but may act as a net source of CO_2 at night when solely respiration is at work. Similarly, traffic emissions from one wind direction may enhance CO_2 flux, while photosynthesizing vegetation from an urban park in another wind direction may deplete CO_2. Figure 1.1 provides an example of the effects of changing seasons on the availability and distribution of water sources at the surface. This spatial and temporal heterogeneity of sources and sinks of turbulent entities like CO_2, water vapour, heat, and momentum will affect flux tower measurements.

Figure 1.1: A SW view from atop the EC flux tower used in this research of the adjacent residential area, during each month of the year from 2008 – 2009. Changes in water availability and distributions over the course of the year are visible (for example, the presence of broadleaf foliage, droughts, and snow cover). Photos provided by the automatic system (UBC Geography).

1.2.1 Tower placement

To capture the aggregated effects of the source area, or the area at the surface that influences EC measurements, towers need to be placed in the inertial sublayer (ISL), the layer directly above the roughness sublayer (RSL) where the effects of the underlying surface are well mixed, and heterogeneity is assumed to be averaged away (Arnfield 2003). This height depends on surface properties of the measurement area, as roughness elements will determine the depth of the RSL (Feigenwinter et al., 2012). Consequently, to characterize urban areas with very high buildings, flux towers need to be extremely tall (Al-Jiboori 2008). Since the scale of the measured source area will increase with tower height, consideration of both vertical and horizontal extents is also required (Velasco and Roth 2010).

Furthermore, towers need to be set up in the source area of the turbulent entities of interest. For example, some studies have set up EC towers either directly in an urban park, or on the periphery of one to isolate the relative contributions of biogenic and anthropogenic CO_2 emissions to the urban atmosphere (Kordowski and Kuttler 2010, Park et al., 2013). Thus, tower placement requires knowledge of how the spatial distribution of sources and sinks may affect flux measurements.

1.2.2 Monin-Obukhov similarity theory

As turbulent transfer of heat, mass, and momentum is dissimilar and highly source area-dependent in cities, widely accepted similarity theories, such as the Monin-Obukhov similarity theory (MOS), usually do not apply. MOS states that mean flow and temperature in the bottom 10% of the surface layer depend only on a stability parameter (z'/L), with $z' = z - z_d$, where z' is the effective measurement height of the EC tower, z is the height of the EC equipment above the zero-plane displacement height (z_d), and L is the Obukhov Length, or the theoretical height where buoyant and frictional forces are equal (see Equation 2 in Section 2.2).

Under MOS, it is expected that the structures responsible for transferring heat and water vapour act equally on both scalars (Roth and Oke 1995). In the roughness sublayer (RSL), most turbulence is

created locally, and influenced by individual roughness elements rather than their blended effects, which would be present in the inertial sublayer (ISL) above. Therefore, MOS is not useful for determining the transport of eddies produced in the RSL (Al-Jiboori 2008, Wang et al., 2014). Nevertheless, many studies still use MOS in flow and diffusion models despite its inappropriateness when describing the atmosphere close to urban surfaces (Feigenwinter et al., 1999).

The MOS-predicted normalized standard deviations (see Section 2.2) under neutral conditions are generally considered to apply in the ISL over cities, but results from Roth and Oke (1995) show variability in these entities, invalidating MOS under unstable atmospheric conditions when the source area is closer to the tower, and over rough, heterogeneous surfaces (Roth and Oke 1995, Al-Jiboori 2008, Arnfield 2003). While the reliability of similarity theories like MOS in the urban boundary layer may be questionable, the normalized standard deviations of wind velocities (Section 2.2) and temperature do provide a neutral limit with which to evaluate the effects of surface heterogeneity on turbulent exchange (Oke et al., 2017).

1.3 Tools for investigating turbulent exchange

1.3.1 Correlation coefficients

Eddy covariance (EC) provides information on the movement, or flux, of momentum and scalars over time. Using EC flux measurements, correlation coefficients, which provide a way of determining the efficiency with which heat, mass, and momentum are exchanged, can be calculated. Correlation coefficients are calculated as the covariance of a turbulent entity, or the flux, divided by the respective standard deviation of both fluctuating components in the covariance term (see Equations 8 – 12 in Section 2.2 for calculations of the correlation coefficients).

Turbulent exchange efficiency, represented by the correlation coefficients, has been the focus of many urban turbulence studies, and Roth and Oke (1995) were among the first researchers to explore the idea of relative exchange efficiency between different scalars. They used ratios of correlation coefficients

of different quantities to observe whether, over a suburban area, the transfer of heat, water vapour, and momentum behave similarly. Additionally, they considered how different atmospheric stabilities affect these transfer efficiency ratios, and found that sensible heat is transferred more efficiently than water over urban surfaces. Figure 1.2 gives an example of how spatial variability of water sources at the surface can manifest in higher or lower exchange efficiencies of water vapour. If sources of a turbulent entity are spatially patchy, it is expected that only some eddies will be able to transfer that entity, resulting in a lower correlation coefficient, or a smaller exchange efficiency. Conversely, if sources at the surface are uniformly distributed or abundant in the source area, more eddies will be able to transfer the turbulent entity, resulting in a much larger exchange efficiency.

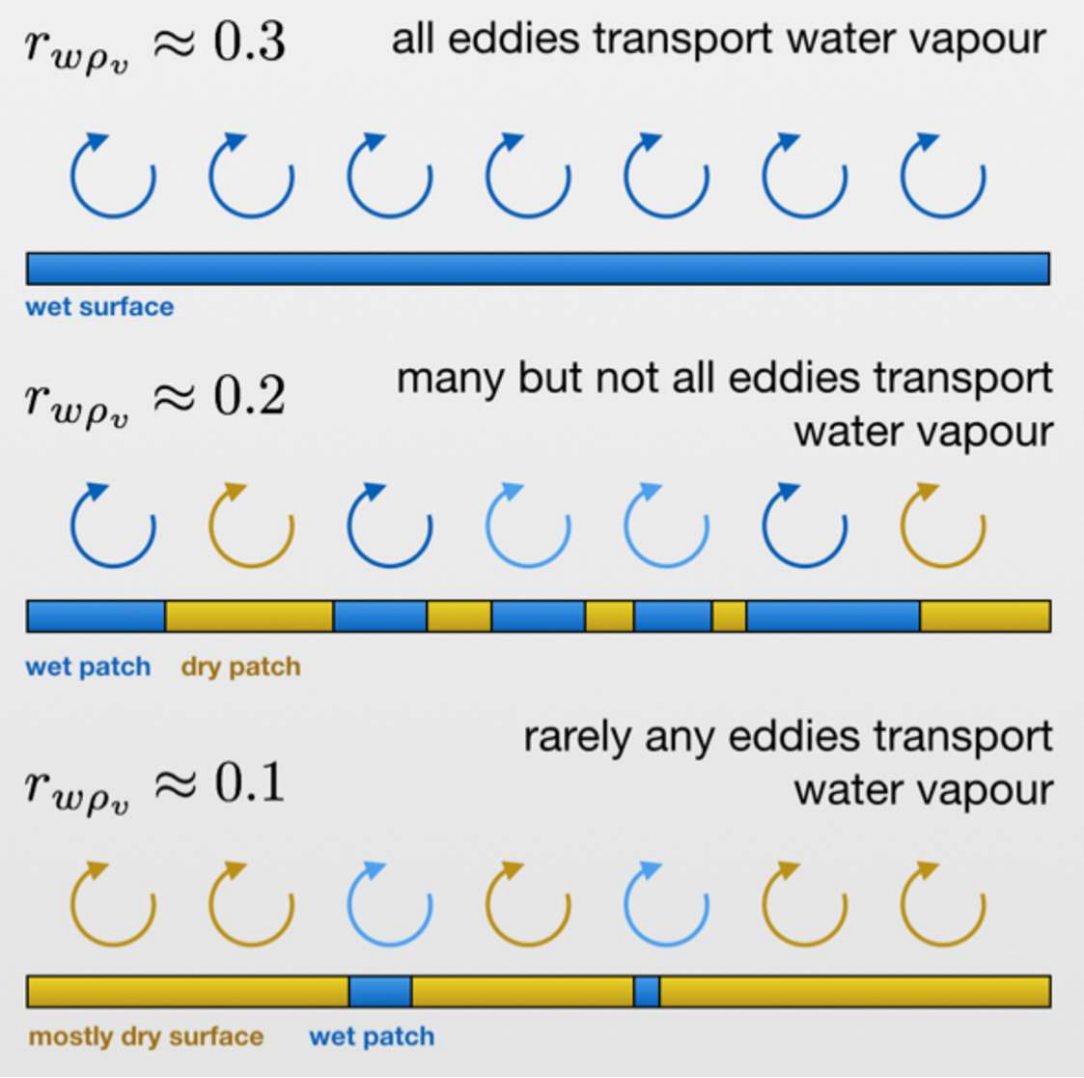

Figure 1.2: Example of how different surfaces with varying levels of source/sink heterogeneity may influence turbulent exchange efficiency of water vapour (represented in this image by the variable $r_{w\rho_v}$). When a surface is uniformly wet (top case), all eddies can transfer water vapour, and the resultant $r_{w\rho_v}$ is large (here, $r_{w\rho_v}$ is equal to approximately 0.3). As sources of water at the surface become patchier, however, fewer and fewer eddies are able to transport water vapour, and $r_{w\rho_v}$ decreases (see Section 2.2). Image provided with permission from A. Christen (2017).

1.3.2 Coherent structures

Coherent turbulent structures are responsible for much of the motion involved in the flux of momentum and scalars (Wang et al., 2014). Analysis of turbulence within and above vegetated canopies has revealed much about the existence and characteristics of large-scale coherent structures within the roughness sublayer (Raupach 1981, Gao et al., 1989, Finnigan et al., 2009, Dupont and Patton 2012, Francone et al., 2012). A number of studies have investigated whether these structures exist within the urban roughness sublayer (Rotach 1999, Roth 2000, Feigenwinter and Vogt 2005, Moriwaki and Kanda 2006, Christen et al., 2007, Wang et al., 2014) and have subsequently shown turbulent structures to vary with, and depend on stability, urban morphology and source/sink heterogeneity (Roth 2000, Grimmond and Oke 2002, Feigenwinter and Vogt 2005). While many studies focus on Reynold's stress (momentum), increasingly, studies that explore the motion of scalars have sought to better understand dissimilarity between heat, moisture, and trace gas exchange over urban areas (Moriwaki and Kanda 2006, Wang et al., 2014).

Coherent, or "organized", motion of momentum and scalars can be investigated via quadrant analysis. Quadrant analysis uses EC measurements to provide information on the vertical motion of turbulent transfer. By separating instantaneous flux measurements into one of four quadrants defined by a Cartesian plane, information on the fractional contribution of events in quadrant 2 and events in quadrant 4 to total fluxes, can be established (Katul et al., 2006). Instantaneous fluxes are allocated into each quadrant based on the sign of both components of the covariance term (Katsouvas et al., 2007).

Furthermore, since EC measurements are taken at a fixed location, the signals of different eddies passing by can be represented as a function of time (Stull 1988); By introducing a function that omits small-scale structures from analysis, the time it takes for the larger structures to contribute to a portion of a flux can be examined (Paw U et al., 1992). This provides a measure of intermittency of a flux, and a way of analyzing the temporal influences of spatial heterogeneity.

Wang et al. (2014) found that there is a strong dependence of turbulent structures on the stability condition of the atmosphere. Their analysis suggests that under a neutral or stable atmosphere, and within the urban RSL, momentum and scalars are transferred most efficiently by sweeps, while ejections are characteristic in both the RSL and the ISL under unstable conditions. Notably, however, most urban studies on turbulent motion and the relative contribution of sweeps and ejections have been in relation to vertical profiles in urban canopies (Roth and Oke 1993, Oikawa and Meng 1995, Feigenwinter et al., 1999). Few studies have analyzed the effects of temporal and spatial heterogeneity on the motion of momentum and scalars.

1.3.3 Footprint modelling

The flux footprint is the area upwind of the EC tower that influences the point measurement made at the tower (Leclerc and Foken 2014). Footprint modelling quantitatively establishes spatially-referenced turbulent exchanges (Schmid 2002). The size, shape, and orientation of a footprint is dependent on the height of the tower, surface roughness length, wind speed and direction, and the stability of the atmosphere (Chen et al., 2011, Feigenwinter et al., 2012). Some examples of footprint models include Large Eddy Simulation (LES) models, cumulative normalized contribution to flux measurements (CNF) models, Lagrangian stochastic models, and Eulerian models (Flesch 1996, Leclerc et al., 1997, Gockede et al., 2004, Grimmond 2004, Burba 2013).

Unfortunately, the spatial distribution of contributing sources within the footprint must be estimated, and a source weighting function has to be applied for it to be modeled (Schmid 1997, Schmid and Lloyd 1999). To alleviate this, some studies have used remote sensing to resolve some of the heterogeneity in surface source/sink distributions (Schmid and Lloyd 1999, Chen et al., 2011, Crawford and Christen 2015).

1.3.4 Remote sensing

Attributing spatially-accurate surface characteristics to turbulent fluxes using remotely-sensed imagery (airborne, tower-mounted, or satellite), is becoming a widely-used tool for quantifying the spatial scale and properties of structures at the surface (Grimmond 2006). Urban areas, with complex 3D form, are the prime location for such imagery (Soux et al., 2003). Thermal remote sensing uses aircraft thermography close enough to the surface to resolve structures like roads, roofs, and walls (Arnfield 2003). Goodwin et al. (2009), Tooke et al. (2009), and Liss et al. (2010) used satellite imagery in conjunction with aircraft-mounted LiDAR (Light Detection and Ranging) data to derive surface land cover types, aggregated into a gridded surface (Figure 1.3) (Christen et al., 2010). Remotely-sensed surface data can be categorized into many different land cover types, allowing source/sink distributions to be analyzed in more detail (Gockede et al., 2004).

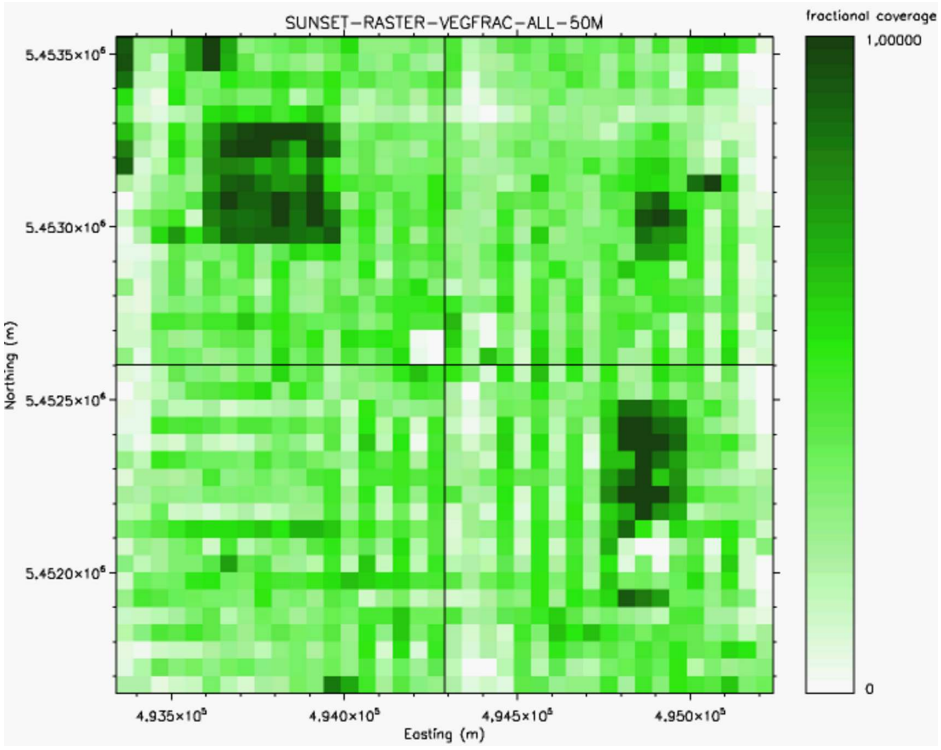

Figure 1.3: Remotely-sensed image of plan area coverage of total vegetation in a suburban area based on satellite and LiDAR-derived surface data (Goodwin et al., 2009, Tooke et al., 2009, Christen et al., 2010, Liss et al., 2010).

Remote sensing can effectively augment surface-measured flux data and footprint models to better describe urban surface heterogeneity. However, surface complexities may impede acquisition of such data; Vertical surfaces like building walls interact with the atmosphere and influence turbulent structures that carry heat, mass and momentum, but these surfaces may not always be seen by the sensors. This problem is exacerbated by the fact that different cities have different solar regimes, meaning different surfaces will receive varying amounts of radiation (Soux et al., 2003).

1.4 Knowledge gaps

Methods of characterizing heterogeneity to assess the quality of flux data have been proposed and employed by a few studies (Lloyd 1995, Foken and Wichura 1996, Gockede et al., 2004, Grimmond 2006, Velasco and Roth 2010, Crawford and Christen 2015). These studies explore the combined use of footprint models, remote sensing, and emission inventories to investigate the relationship between surface heterogeneity and flux measurements. For example, Christen et al. (2011) combined remote sensing data, emissions inventories, land use data, population density, and traffic count data into a model that determined CO_2 emissions using top-down and bottom-up approaches, and compared model outputs to actual measured CO_2 from an EC tower in the source area.

Of the studies that investigate dissimilarities between momentum and scalar exchange, and dissimilarity between different scalars, most focus on the effects of measurement heights, or stability (Table 1.1). These studies have shown a strong dependence on stratifying data by particular atmospheric conditions, indicative of the influence of urban areas on stability regimes.

Table 1.1: Select studies on surface heterogeneity and its effects on exchange efficiency. The location of the study, the duration, whether geospatially-referenced surface data was linked to exchanges, the focus, and the correlation coefficients of interest are also listed for each study.

Reference	Ecosystem	Duration	Geospatial attribution	Focus	Correlation coefficient
McBean 1970	Rural	2 days (August)	None	Stability	r_{wT}, r_{wh}, r_{uw}
Roth & Oke 1995	Urban	8 days (July)	None	Stability	r_{wT}, r_{wh}, r_{uw}
Moriwaki and Kanda 2006	Urban	1 month (July - daytime hours only)	None	Stability	r_{wT}, r_{wh}, r_{uw}, r_{wc}
Al-Jiboori 2008	Urban	10 days (April)	None	Stability	r_{wT}, r_{wh}, r_{uw}
Detto et al., 2008	Forest	2.5 years	Satellite images (land cover type)	MOS, entrainment effects	r_{wT}, r_{wh}, r_{uw}, r_{wc}
Li and Bou-Zeid 2011	Vineyard	3 months (August – October)	None	Coherent structures	r_{wT}, r_{wh}, r_{uw}
Francone et al., 2012	Vineyard	6 months (May-October)	None	Coherent structures	r_{wT}, r_{uw}
Nordbo et al., 2013	Urban	1 year	Directionally-isolated discrete land-use types	MOS and surface roughness	r_{wT}, r_{wh}, r_{uw}, r_{wc}
Wang et al., 2014	Urban	4 months (May - August)	None	Stability, effects of measurement height	r_{wT}, r_{wh}, r_{uw}, r_{wc}

Notably, while these studies acknowledge and seek to understand the effects of surface source/sink heterogeneity on turbulent exchange, there is a severe lack of studies that directly relate measured exchange efficiencies to detailed, remotely-sensed geospatial information on the distribution of those sources and sinks. Moreover, very few studies span longer than a month, but those that do usually take place in summer and during daytime hours only. Even the long-term studies generally do not consider diurnal and seasonal changes in surface characteristics in relation to turbulent exchange.

The efficiency with which heat, water vapour, momentum, and CO_2 are exchanged in complex urban environments depends on the temporally-changing spatial distributions of sources and sinks at the surface, as well as atmospheric stability, which is also temporally variable.

1.5 Research objectives

The goal of this research is to characterize the relationship between surface heterogeneity and the efficiency of turbulent exchange of momentum and scalars over an urban landscape. Specifically, the aim is to:

1) Characterize the efficiency of momentum, sensible heat, water vapour, and CO_2 exchange over a heterogeneous urban landscape using eight years of continuous flux data
2) Investigate how these exchange efficiencies change seasonally and diurnally, under different atmospheric stabilities, and from different wind directions
3) Relate these exchange efficiencies to remotely-sensed and geospatially-referenced source area patchiness.

Chapter 2: Methods

2.1 Study site

Eight years of eddy covariance (EC) data (May 5, 2008 - May 5, 2016) was attained from a triangular lattice EC tower located within a residential area in the City of Vancouver, BC, Canada, also known as Vancouver-Sunset (49.2ºN, Fluxnet ID "Ca-VSu"). The tower, colloquially named “Sunset Tower”, is situated in the southeast corner of a BC Hydro substation (Figure 2.1). This site was originally chosen as an ideal location for EC tower measurements, as it is representative of typical Vancouver neighbourhoods, and was considered relatively spatially homogeneous at the time of selection; However, subsequent studies have shown that small-scale spatial variability in the source area of the tower contributes to heterogeneity in flux measurements (Schmid et al., 1991).

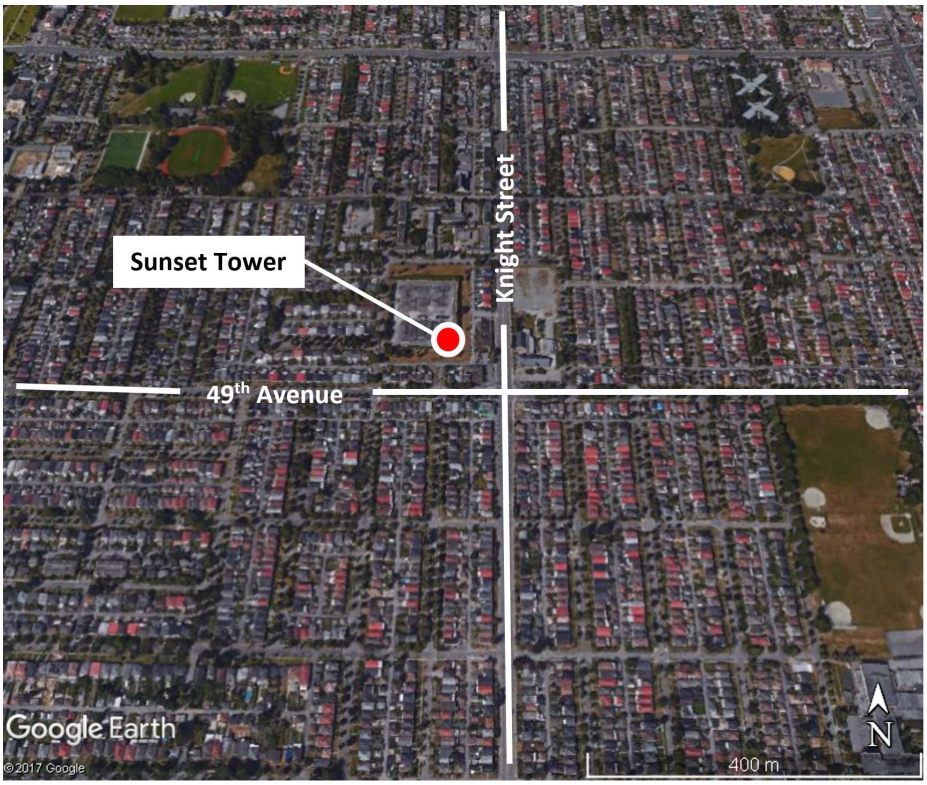

Figure 2.1: Oblique areal image of the study site and surrounding neighbourhood. The location of the eddy covariance tower is indicated by the red dot, and the two busiest major streets in the vicinity of the tower, 49th Avenue and Knight Street, are indicated by the white lines. Image taken from Google Earth.

The 500-m radius surrounding the tower is representative of a typical urban setting with a mix of detached single-family homes (averaging in height at 5.3 m), major roads and residential streets, urban green spaces and parks, and tree coverage of 17.1 stems / ha comprised of primarily deciduous trees (see Table 2.1 below for a detailed list of site characteristics) (Goodwin et al., 2009, Tooke et al., 2009, Liss et al., 2010). The dwellings in the study area are primarily heated via natural gas which, when combusted, emits carbon dioxide into the atmosphere (Christen et al., 2010). The study site falls under the local climate zone category of "open low-rise", or "LCZ 6", which is characteristic of most North American cities (Stewart and Oke 2012). The exact coordinates of the tower are 123.0784°W, and 49.2261°N (WGS-84). This tower has been in operation since 1978, and has since contributed to a number of urban eddy covariance studies that span the decades (Schmid et al., 1991, Roth and Oke 1995, Grimmond and

Oke 2002, Crawford and Christen 2015, Giometto et al., 2017). Changes in land-use and land cover type within the tower's source area are minimal over the eight-year period from which the flux data was acquired.

Table 2.1: Characteristics of Sunset Tower and the surface plan area fractions in the surrounding 500 m radius. "Plan area" refers to the fraction of the surface in the 500 m radius of the tower for which the relevant surface characteristic occupies. Note that "plan area of ground vegetation" does not consider vegetation underneath trees.

Coordinates (longitude, latitude)	123.078ºW, 49.226ºN
Tower Height	28 m a.g.l.
Average Roof Height	5.3 m
Maximum Building Height	7.9 m
Plan Area of Buildings	29%
Plan Area of Trees	12%
Plan Area of Ground Vegetation	22%
Plan Area of Impervious Ground	37%
Building Density	12.8 buildings / ha
Tree Density	17.1 trees / ha
Population Density	64.1 people / ha

2.1.1 Instrumentation

The EC system that operated during the study period (2008 – 2016) is mounted at a height of 28.8 m above ground level (a.g.l.), with an effective measurement height of 24.8 m a.g.l, and is composed of a 3D sonic anemometer (CSAT 3D, Campbell Scientific, Logan, UT, USA), and an open-path infrared gas analyzer (Li-7500, Licor Inc., Lincoln, NE, USA) (Figure 2.2). Turbulence data acquired from this tower was derived from wind vector measurements (u, v, w) taken by the ultra-sonic anemometer at 60 Hz. The wind vectors were aligned into the direction of mean flow using a double-rotation approach during post-processing.

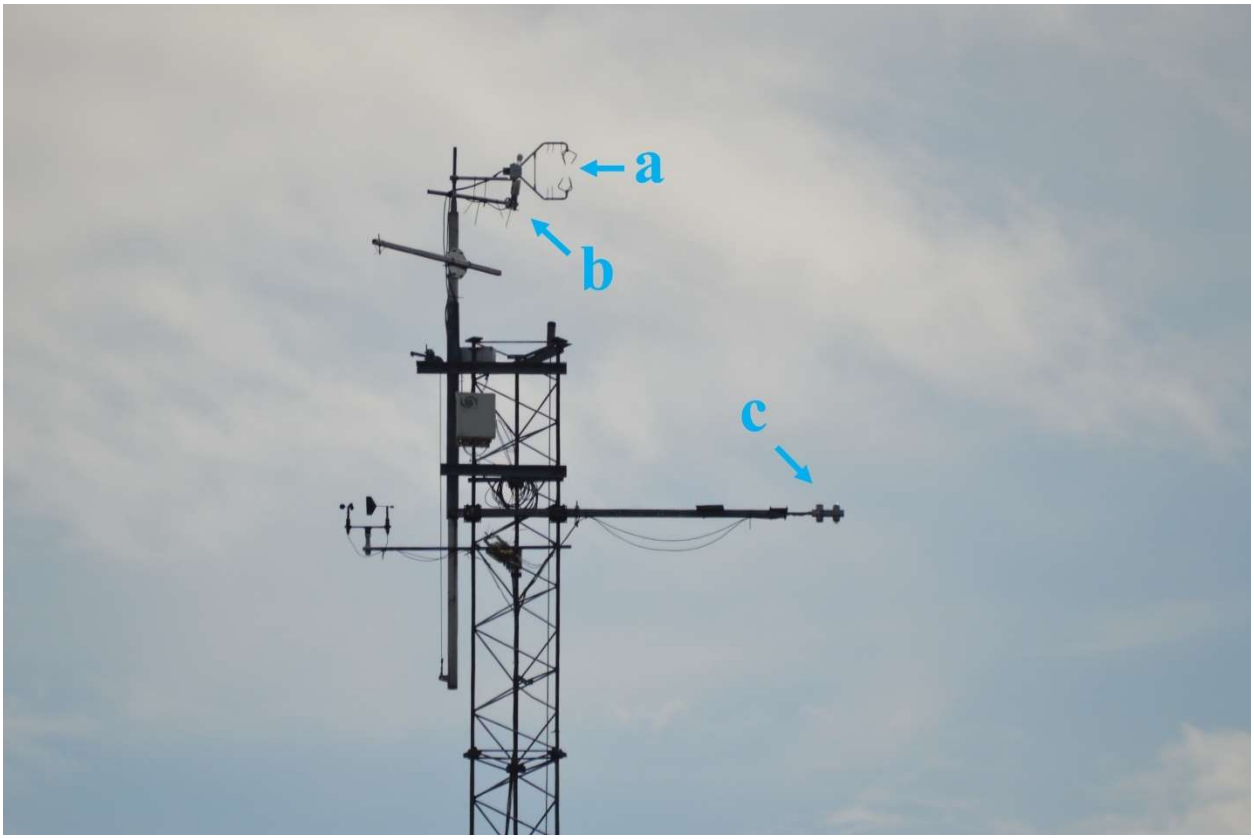

Figure 2.2: View of the instrumentation mounted at the top of Sunset Tower as seen from the West. The (a) 3D sonic anemometer, the (b) infrared gas analyzer, and the (c) net radiometer are pictured here.

Fluxes of water vapour, sensible heat, CO_2, and momentum were recorded, stored at a frequency of 20 Hz, and block-averaged into 30-minute subsets. Radiation data, such as incoming and net solar radiation (K_{down}, R_{net}) was also obtained from a net radiometer mounted at a height of 22 m (CNR-1, Kipp and Zonen, Delft, Netherlands) on the tower. Precipitation data was recorded using a rain gauge about a meter (horizontally) from the base of the tower, air temperature was obtained acoustically from the sonic anemometer on the EC tower, and soil moisture was obtained from 30-minute aggregated soil volumetric water content readings using water content reflectometers (CSI616, Campbell Scientific, Logan, UT, USA) continuously operating in eight representative lawns within the study area (Christen et al., 2009, Christen et al., 2013).

2.2 Data processing

In order to easily stratify data and select for certain conditions during analysis, a number of parameters and variables were first calculated using the compiled meteorological and climatological data.

2.2.1 Stability

The ability to stratify 30-minute block-averaged flux data into different stability classes was critical to isolate certain atmospheric conditions during analysis. Stability was calculated as z'/L, where $z' = (z - z_d)$, and L is the Obukhov Length (m) measured at the tower. z is the measuring height of the tower (24.8 m) and z_d is the displacement height (7.48 m) based on the average of the summer and winter roughness values derived from Large Eddy Simulation (LES) models of the study site (Equation 1) (Giometto et al., 2017):

$$\frac{summer\left(\frac{z_d}{H_b}\right)(H_b) + winter\left(\frac{z_d}{H_b}\right)(H_b)}{2} = z_d, \quad (1)$$

where H_b refers to the mean building height (6.8 m), modeled summer (z_d/H_b), equal to 1.0 m, and modeled winter (z_d/H_b), equal to 1.26.

L is calculated using Equation 2, where T is the acoustic air temperature measured by the sonic anemometer in Kelvin, u_* is the friction velocity calculated as $u_* = (\overline{u'w'}^2 + \overline{v'w'}^2)^{0.25}$, κ is the von Karman constant (0.40), g is the acceleration due to gravity (9.81 m s^{-2}), and θ_* is the frictional temperature calculated as $\theta_* = -\overline{w'T'}/u_*$.

$$L = \frac{Tu_*}{\kappa g \theta_*}. \quad (2)$$

Unstable conditions occur when z'/L is negative, and are further considered to range from very unstable (approximately -1 to -10) to weakly unstable (-0.1 to -1). When z'/L is close to zero, the atmosphere is dynamically neutral (between -0.1 and 0.1). Finally, the atmosphere is considered stable when z'/L is positive; a weakly stable atmosphere ranges between 0.1 and 1, and a strongly stable atmosphere ranges from 1 to 10.

2.2.2 Roughness length

The roughness length (z_0) is the height above the displacement height (z_d) where mean wind becomes zero in the ISL above a city according to the logarithmic law. Within the RSL, the logarithmic law is invalid, as wind does not become zero here. Roughness lengths used in this research were calculated following Equation 3

$$z_0 = (z - z_d) \exp\left(-\frac{u\,\kappa}{u_*}\right), \tag{3}$$

where u is equal to $\sqrt{{u_E}^2 + {u_N}^2}$ in which u_E is the easting wind velocity component, and u_N is the northing wind velocity component.

2.2.3 Flux density calculations

Calculations of sensible and latent heat flux densities (Q_H and Q_E, respectively) used in subsequent analyses are pre-processes by the EC system and stored at high frequency. For reference, calculations of Q_E and Q_H are given by Equations 4 and 5.

$$Q_E = L_v \overline{w'\rho_v'}, \tag{4}$$

$$Q_H = \rho c_p \overline{w'T'}, \quad (5)$$

where L_v is the latent heat of vapourization (J kg^{-1}), $\overline{w'\rho_v'}$ is the covariance between vertical wind (w) (m s^{-1}), and water vapour density (ρ_v) (kg m^{-3}), which is mostly presented as ($w'h'$) in this study. ρ refers to the density of air (kg m^{-3}), and c_p is the specific heat of air (J kg^{-1} K^{-1}). Carbon dioxide (CO_2) fluxes (F_C) (μmol m^{-2} s^{-1}) are also calculated by the EC system as

$$F_C = \overline{w'\rho_{CO_2}'}, \quad (6)$$

where ρ_{CO_2}' is the density of carbon dioxide (kg m^{-3}).

The Bowen ratio is given as the fraction of sensible heat flux divided the fraction of latent heat flux (Equation 7)

$$B = \frac{Q_H}{Q_E}. \quad (7)$$

2.2.4 Correlation coefficients

Exchange efficiency of sensible heat, water vapour, momentum, and CO_2 are given by the linear correlation coefficients, r_{wT}, r_{wh}, r_{uw}, and r_{wc}, respectively, defined by

$$r_{wT} = \overline{w'T'} / \sigma_w\sigma_T, \quad (8)$$

$$r_{wh} = \overline{w'h'} / \sigma_w\sigma_h, \quad (9)$$

$$r_{uw} = \overline{u'w'} / \sigma_u\sigma_w, \quad (10)$$

$$r_{wc} = \overline{w'c'} / \sigma_w\sigma_c, \quad (11)$$

$$r_{Th} = \overline{T'h'} \,/\, \sigma_T \sigma_h, \tag{12}$$

where u and w are the longitudinal and vertical velocities (m s^{-1}), and σ_i refers to the standard deviation of the respective flux variable (i). r_{Th} is the correlation coefficient of temperature and humidity. Correlation coefficients range in value from -1 (perfectly negative correlation) to 1 (perfectly positive correlation). A value of zero means the variables exhibit no net variation together, and indicates that exchange is very inefficient (Stull 1988).

To compare calculated exchange efficiency values based on the derived flux data to the MOS-predicted values derived from aggregated datasets over multiple cities, normalized standard deviations of wind velocities and semi-empirical constants are used (Roth 2000). The MOS-predicted normalized standard deviations (A_i) are defined as:

$$A_i = \sigma_i \,/\, u_* \quad (i = u, v, w, T), \tag{13}$$

with σ being the standard deviation, u, v, w being the horizontal, lateral, and vertical wind velocities, respectively, and T representing the mean air temperature. For unstable conditions,

$$A_i = a_i\{1 - b_i(z'/L)\}^{c_i}, \tag{14}$$

where a_i, b_i, and c_i are semi-empirical constants (Panofsky and Dutton 1984, and DeBruin et al., 1993). For urban sites, A_i can be calculated using the MOS-predicted values of semi-empirical constants given in Table 2.2 below:

Table 2.2: Predicted semi-empirical constants (a_i, b_i, c_i) for horizontal (u), vertical (w), and lateral (v) wind components, as well as temperature (T) (Roth 2000).

i	a_i	b_i	c_i
u	1.98	0.33	0.56
v	1.64	2.84	0.30
w	1.12	2.48	0.33
T	-3.03	24.4	-0.33

Multiplying the calculated A_i value for one turbulent component (u, w, v, T) by a value of A_i for another turbulent component, yields the predicted correlation coefficient of those turbulent components, for a specific stability.

2.2.5 Intermittency

A hyperbolic hole of size H defines the area within the quadrant plane that separates large-scale, rare contributions of a flux, $|w'a'|$, from smaller, frequent ones:

$$|w'a'| = H|\overline{w'a'}|. \tag{15}$$

The fractional contribution of each quadrant to the total flux is defined as

$$S(i,H) = \ w'a'_{\,i,H} \,/\, \overline{w'a'}, \tag{16}$$

where a' is equal to the instantaneous horizontal velocity (u) fluctuation for the case of momentum, or some scalar quantity (T, h, c), and

$$\overline{w'a'}_{i,H} \ = \frac{1}{T_a} \int_0^{T_a} w'a' \, I_{i,H}\,(t)\, dt, \tag{17}$$

where T_a is the flux averaging period (30 minutes was used in this research), i refers to the respective quadrant (i = 1, 2, 3, 4), and $I_{i,H}$ is equal to 1 if $w'a'$ is in quadrant i and $|w'a'| \geq H|\overline{w'a'}|$, or equal to 0 if otherwise. The hole size (H) above which half of the flux occurs (Raupach et al., 1986) is defined by

$$\sum_{i=1}^{4} S(i,H) = \frac{1}{2}, \tag{18}$$

and the time fraction outside of this hole, (above which half of the flux occurs) is

$$T(i,H) = \frac{1}{T_a} \int_0^{T_a} I_{i,H}\,(t)\,dt. \tag{19}$$

The time fraction above which half of the total flux in a given averaging period occurs is a measure of the intermittency of exchange, or the rarity of events that contribute to the majority of a flux (Christen et al., 2007). A large time fraction is an indication that many, frequently-occurring events are contributing to half of the flux. Time fraction values less than Gaussian turbulence (0.1) are considered more intermittent, and thus only a few, rare events are contributing greatly to the total flux.

2.2.6 Sweeps and ejections

Quadrant analysis provides information on the characteristic size and time occupied by the flux of a turbulent entity, as well as whether upward or downward flux motion is most dominant. Quadrants 2 and 4 of the Cartesian plane (Figure 2.3) reflect coherent (organized) motion (Katsouvas et al., 2007). For momentum fluxes, ejections refer to low-momentum upward transport (events in quadrant 2), and sweeps denote high-momentum downward transport (events in quadrant 4). Events that occur in quadrants 1 and 3 are considered to be unorganized structures, and are referred to as outward and inward interactions,

respectively. These unorganized structures produce fluxes that are counter-gradient, and thus reduce the magnitude of the net flux.

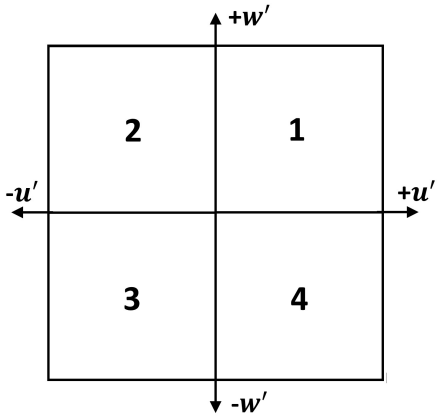

Quadrant 1: $u' > 0$, $w' > 0$, outward interactions,
Quadrant 2: $u' < 0$, $w' > 0$, ejections,
Quadrant 3: $u' < 0$, $w' < 0$, inward interactions,
Quadrant 4: $u' > 0$, $w' < 0$, sweeps.

Figure 2.3: The Cartesian plane used in the allocation of momentum fluxes, and the associated conditions under which an event is classified as occurring in quadrants 1, 2, 3, or 4 (Wang et al., 2014).

Quadrant analysis can also be used to investigate the movement of scalars by coupling a wind component (vertical, lateral or horizontal) with heat, water vapour, or CO_2 (Moriwaki and Kanda 2006). For example, ejections of sensible heat refer to warm, upward-moving eddies, and sweeps refer to cool, downward-moving eddies (Christen et al., 2007). This is done by making an adjustment to the Cartesian plane as depicted in Figure 2.4.

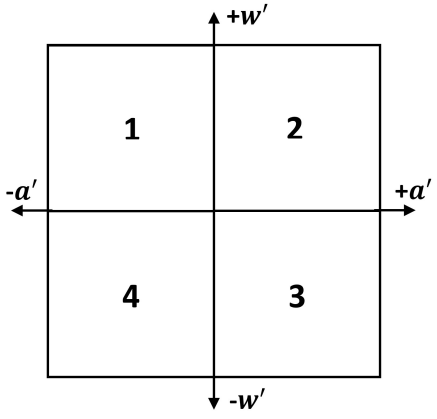

Figure 2.4: Cartesian plane with coordinates of the quadrants redistributed for use when defining the motion of scalar fluxes. By changing the coordinates of the plane, definitions of ejections, sweeps, outward, and inward interactions are consistent for momentum and scalar motion.

A sweep is defined as an event that occurs in quadrant 4, and an ejection is an event that occurs in quadrant 2. In the case of momentum flux, an occurrence in quadrant 4 means that the instantaneous horizontal wind component (u') is greater than zero, and the instantaneous vertical wind component (w') is less than zero, thus the motion of the flux is downward and fast. The opposite is true for events in quadrant 2, where u' is negative and w' is positive. In either case, the product of u' and w' is negative in these quadrants, and net momentum exchange is toward the surface.

The relative fraction of sweeps minus the fraction of ejections is called ΔS_0, and provides information on whether a flux is dominated by sweeps or ejections. ΔS_0 is calculated as

$$\Delta S_0 = S_4 - S_2, \tag{20}$$

where S_4 refers to the fraction of events happening in quadrant 4 (sweeps), and S_2 is the fraction of events happening in quadrant 2 (ejections). Analysis of the difference in fractional contributions between sweeps and ejections can also describe scalar motion.

2.3 Tools to select and stratify data

An advantage as well as a challenge to working with such an extensive dataset is the ability to conditionally select a set of criteria to isolate the effects of time and space on turbulent exchange. To easily perform temporal, geospatial, and quadrant analyses, as well as stratify data by hours, days, months, wind directions, and stabilities, an Interactive Data Language (IDL) program version 8.5.1 (Harris Geospatial, Inc., Colorado, USA) was used. The program directly reads tower-measured turbulent and climatological data from a database, and performs any necessary preliminary calculations (see previous section). Subsequent IDL programs that make use of the main program were written to perform each specific analysis, and output graphics.

Analyses were performed by first stratifying data by wind direction or sector (to isolate areas of distinct surface properties), atmospheric stability (to differentiate the effects of stability on exchange efficiency from the effects of surface patchiness), and time.

Daytime hours were considered to range from 6:00 – 17:59 PST, and nighttime from 18:00-5:59 PST. Seasonal analyses were performed by isolating data into summer (June to August), spring (March to May), fall (September to November), and winter (December to February) months. Leaves-off season was considered to be from November to March, based on previous studies in the area (Grimmond and Oke 1998, Voogt and Grimmond 2000), leaves-on season was considered to range from May to September, and the two transition periods between leaves on and off were April and October.

Heating degree day (HDD) was calculated as the threshold temperature for an area minus the average daily air temperature. The average daily temperature was calculated based on 30-minute aggregated air temperature data from the flux tower, averaged into 24 hour periods. The threshold temperature used in this study was 15°C.

Unstable conditions, unless otherwise stated, were taken to range from $-0.1 > z'/L > -10$. Neutral conditions are considered to range from $-0.1 < z'/L < 0.1$, and stable conditions range from $0.1 < z'/L < 10$.

Data was often isolated to consider the SW wind sector only; Preliminary results indicated correlation coefficients are generally reduced in magnitude from the NE wind sector (0-90°), and enhanced in the SW (180-270°). A previous study that examined the location bias of the footprint-averaged land cover fractions found the tower measurements from the SW sector to be most representative of the entire study domain, and therefore, the least biased (Crawford and Christen 2015). The SW is considered to be ideal, as the NE sector has an empty gravel lot which reduces momentum exchange, the SE (90-180°) has an unusually tall building and a busy intersection, and the NW (270-360°) contains the BC Hydro substation within which the EC tower is situated, potentially introducing wake

effects. Furthermore, the SW sector is representative of most neighbourhoods in Vancouver, and in other North American cities (Stewart and Oke 2012, Giometto et al., 2017).

2.4 Geospatial data

2.4.1 Flux footprint modelling

Using flux data from the EC tower, the flux footprint (source area) was determined for each 30-minute averaging period over the full eight years, using a two-dimensional crosswind and gradient dispersion model (Kormann and Meixner 2001, Crawford and Christen 2015). The footprint model is an inverse model that works by taking the variables measured at the tower, and inverting time so that the original surface source strength can be determined.

The model calculates the source area of the flux based on the input parameters, rotates the output into the direction of mean wind, and renders one netCDF file for each half-hour period, for the entire eight years of flux data (this code is provided at https://github.com/achristen/Gridded-Turbulent-Source-Area). The resultant geographically-referenced raster files contain coloured grid cells of 25 m by 25 m resolution, within a total domain of 2025 m by 2025 m, that show the source-area weighted (ϕ) vertical flux at the surface within the cell for each unit point source measurement made at the tower (Figure 2.5).

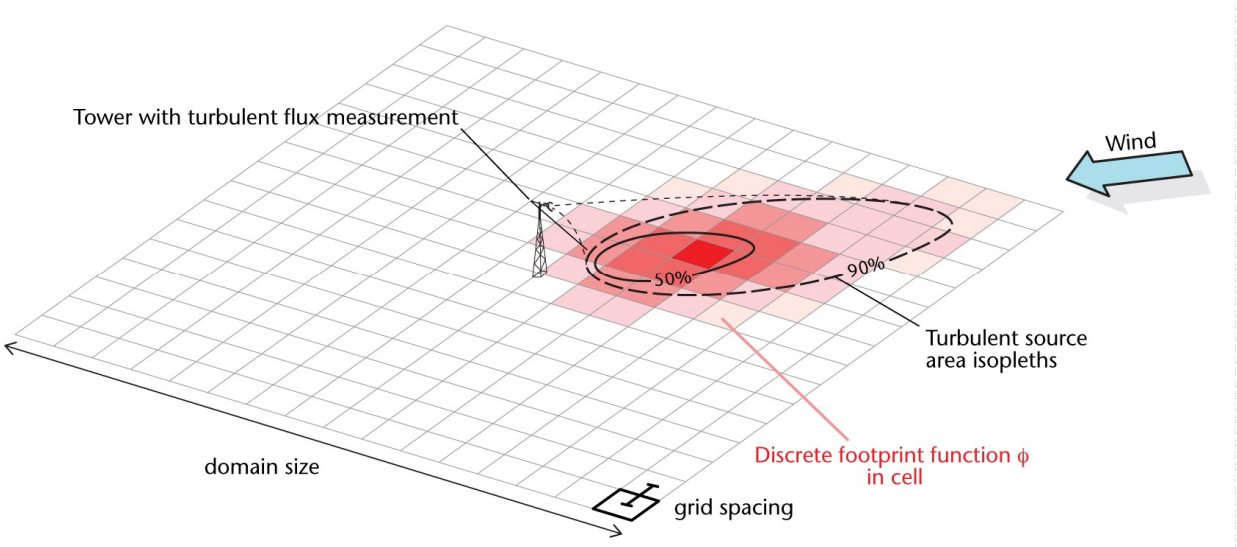

Figure 2.5: Schematic diagram of the flux footprint produced by the analytical footprint model (Kormann and Meixner 2001). The relative contribution from each cell is defined by the source area weighting (ϕ), and is represented here by the intensity of the colour within contributing cells. The image (used with permission) was produced by Andreas Christen (2010).

Input parameters used in the model include time-averaged wind directions, standard deviations of lateral wind (σ_v) velocities, and atmospheric stability (L) (see Table 2.3). This model accounts for the effects of the aerodynamic roughness imposed by leaves during leaves-on seasons versus leaves-off seasons, which influences the effective measurement height of the tower (z').

Table 2.3: Input parameters used in the calculation of the flux footprint (Kormann and Meixner 2001). The codes given in quotations refer to the name of the corresponding variable, as it appears in the database (see also http://ibis.geog.ubc.ca/~epicc/database/ST.html).

Input Parameter	Value	Units	Description
z'	24.8	m	Effective measuring height
z_d	7.48	m	Zero-plane displacement height
g	9.81	m s^{-2}	Acceleration due to gravity
κ	0.40	--	von Karman's constant
Resolution	25 x 25	m	Cell size
Domain	2025 x 2025	m	Domain size
Wind Direction	--	degrees	"STWDA1" value at each time (t)
u	--	m s^{-1}	"STUSA1" the longitudinal (u) wind component at each time (t)
v	--	m s^{-1}	"STVSA1" the lateral (v) wind component at each time (t)
T	--	^{o}C	"STATA1" the acoustic temperature measured by the CSAT3 ultrasonic anemometer at each time (t)
σ_v	--	m s^{-1}	"STYSS1" the standard deviation of the v (lateral) wind component at each time (t)
$u'w'$	--	m^2 s^{-2}	"STUWC1" covariance of easting and vertical wind components at each time (t)
$v'w'$	--	m^2 s^{-2}	"STVWC1" covariance of northing and vertical wind components at each time (t)
$w'T'$	--	m^2 s^{-2}	"STZTC1" covariance of vertical wind and acoustic temperature at each time (t)
u_*	--	m s^{-1}	Friction velocity
L	--	m	Obukhov length

2.4.2 Resampling surface cover data and creating footprint-averaged fractions

The remotely-sensed data utilized in this thesis was provided by previous studies which used multispectral Quickbird satellite images (2.4 m resolution) and joined them with 1 m resolution LiDAR (Light Detection and Ranging) data to derive surface plan-area cover (λ) (Goodwin et al., 2009, Tooke et al., 2009, Liss et al., 2010) (Figure 2.6). Plan-area cover (λ) refers to the percent coverage of a surface type within some domain. The product was one plan-area land cover geoTIFF raster for each land-cover type, at a resolution of 1 m, and a domain of 1900 m by 1900 m with the tower centered at the intersection of four grid cells (Crawford and Christen 2015).

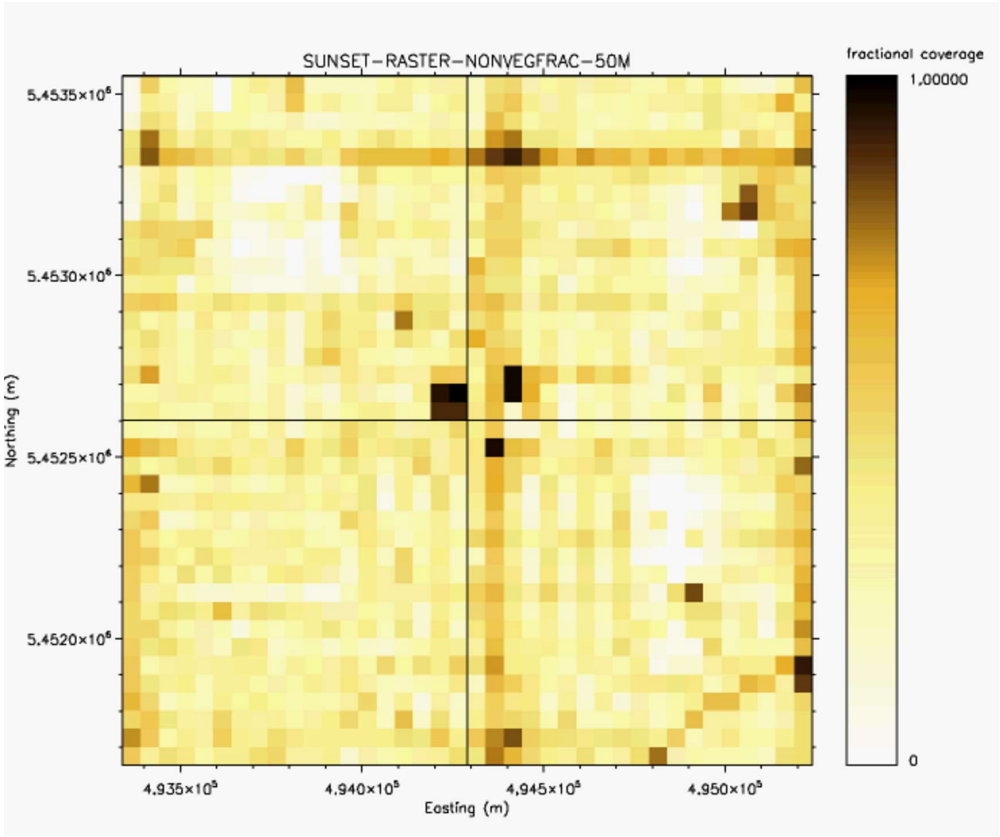

Figure 2.6: Example of the satellite imagery and LiDAR-derived surface plan-area coverage of the 1900 m by 1900 m domain, with the tower (not pictured) centered in the middle. Impervious ground fraction is shown here (Goodwin et al., 2009, Tooke et al., 2009, Liss et al., 2010).

Along with surface cover data, traffic data was also used to assess the effects of the temporally-changing contributions of vehicle emissions to measured fluxes of CO_2 in the study area. Directional traffic counts were measured by the City of Vancouver 13 times along the two major roads in the study area (49th Avenue and Knight Street), including nine counts of intersection traffic movement, and one or more 24-hour weekday counts (Christen et al., 2011). This data was used to produce a profile of weekday traffic trends and amounts for the entire study area. Monthly traffic estimates based on available five-year averaged traffic counts (BC Ministry of Transportation and Infrastructure) were also used to determine annual trends in the study area. Surface cover data used in this research (including traffic data) is listed in Table 2.4.

For the calculated footprint of the tower to be merged with the surface-cover data (see below), these raster files had to be resampled to represent the appropriate tower coordinates and domain. The first step was to reposition the tower's location to the center of one grid cell in the middle of the domain, rather than at the intersection of four grid cells. To do this, the geoTIFF file of interest was read into IDL, and the resolution was doubled from 1 m to 0.5 m. Next, the outer-most 0.5 m on the east and north sides of the grid were trimmed away, and the resolution was recalculated back to 1 m (now offset by 0.5 m). This process placed the EC tower in the correct position.

A new, empty raster was then created, with a resolution of 1 m, and a domain of 2025 m by 2025 m. The resampled land-cover raster was centered within this empty grid, and the resolution was reduced from 1 m to 25 m, for a total of 81 x 81 pixels within the 2025 m by 2025 m domain. The output was one geo-referenced surface plan-area land cover (λ) raster, with the same domain and resolution as was used in the Kormann and Meixner analytical footprint model. This was done for each surface plan-area cover raster.

Using these resampled surface plan-area land coverages, the source area weighting (ϕ) derived from the footprint model for each 30-minute period over the entire eight years was multiplied by each plan-area type (λ), for each grid cell over the entire domain. The resultant footprint-averaged surface

cover fraction (%) gives the fractional contribution of each land cover type within each cell, based on its calculated source area weighting (see Figure 2.7).

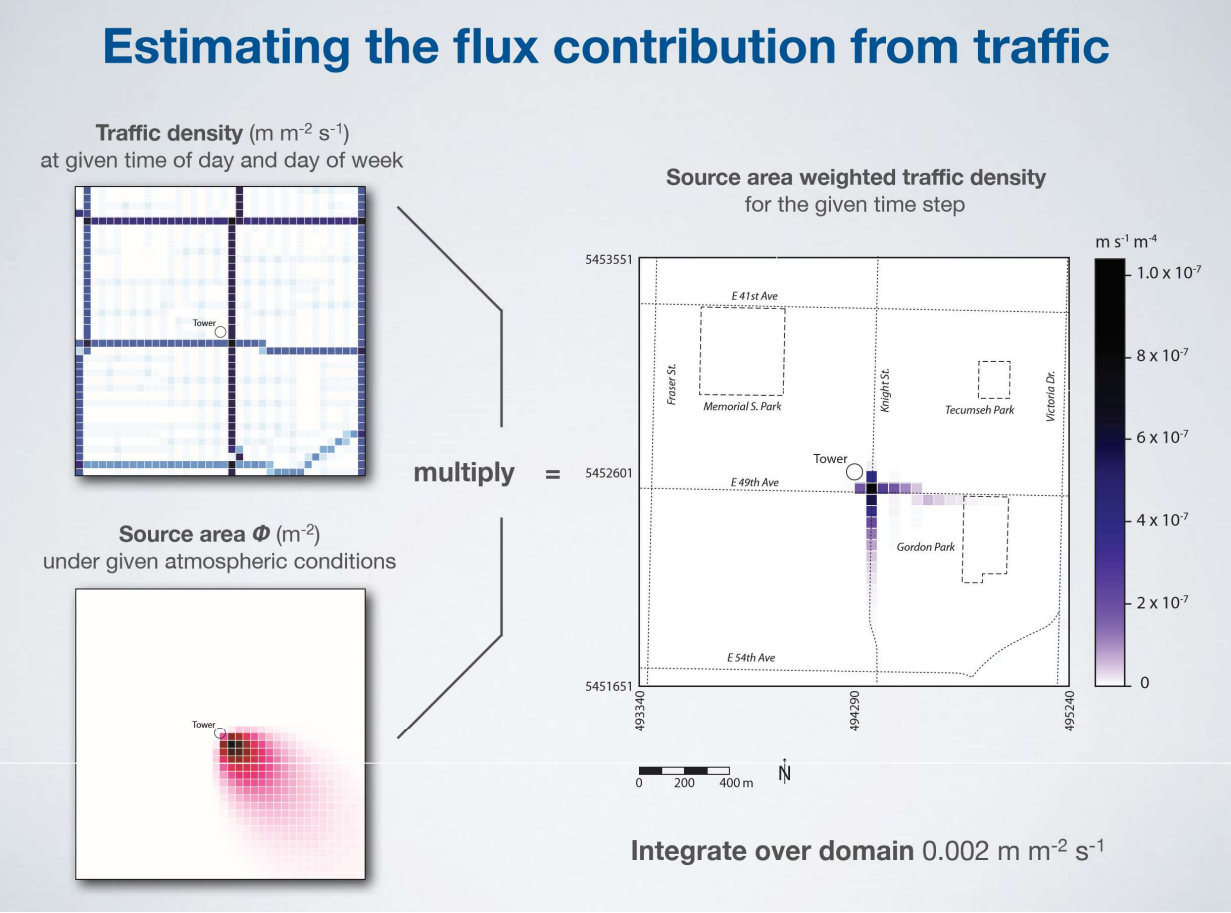

Figure 2.7: An example schematic diagram of the process of combining the surface plan-area coverage (traffic density is pictured here) with the footprint model-derived source area weighting (ϕ) for one 30-minute period, and the resultant footprint-averaged surface cover fraction (in this example, the footprint-averaged traffic density). This image, created by Andreas Christen (2012), was used with permission.

Footprint-averaged land cover fractions for the plan-area cover types used in this research, as well as traffic amounts are provided in Table 2.4. If the flux footprint exceeded the boundaries of the domain, the fraction of the plan-area coverage outside the domain was set to the average value of that land cover type within the entire domain (Christen et al., 2011, Crawford et al., 2014).

Table 2.4: Footprint-averaged land cover elements, based on remotely-sensed surface data, manual traffic counts, and flux footprint modelling. Values represent the long-term footprints over the May 5, 2008 – May 5, 2016 study period measured at Vancouver-Sunset.

Land cover element	Footprint-averaged value	Units
Total vegetation (ground vegetation and trees)	29.51	%
Building plan area fraction	22.09	%
Impervious ground plan area fraction	34.57	%
Building height	4.22	m
Traffic amount	4.94	m (driven) m^{-2} h^{-1}

Chapter 3: Results and discussion

3.1 Site characteristics and climatology

3.1.1 Source area surface characteristics

Typical surface characteristics within the source area of the tower vary greatly with wind direction. To quantify and visualize the spatial variability provided by the satellite imagery and LiDAR-derived surface cover properties within the source area, footprint-averaged surface fractions were plotted against wind direction around the tower (Figure 3.1).

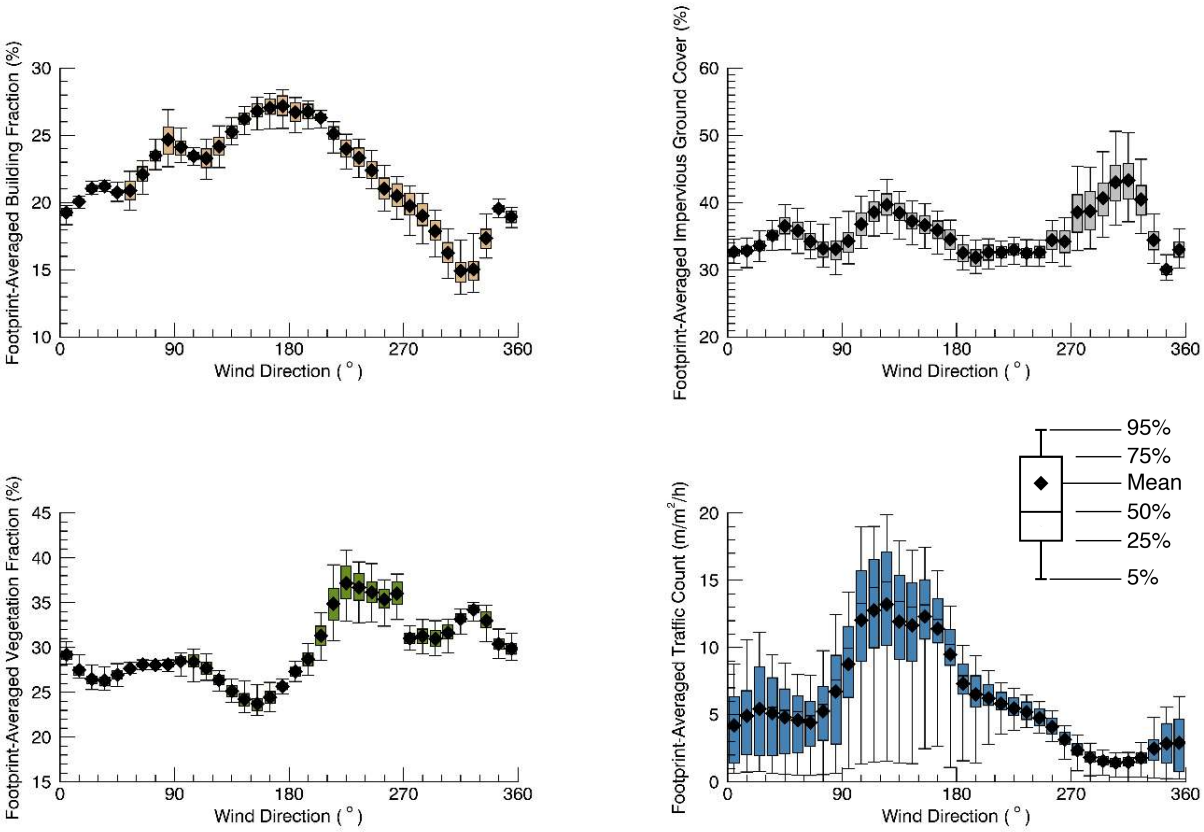

Figure 3.1: Footprint-averaged land-cover fractions and traffic amounts as a function of wind direction, for unstable conditions (z'/L < -0.1). (See Figure B.1 in Appendix B for the stable version).

Figure 3.1 shows footprint-averaged surface cover fractions of impervious ground (arterial roads, residential streets, sidewalks, driveways), total vegetation (trees, lawns, shrubs), buildings, and traffic counts as a function of wind direction.

Impervious ground fractions fluctuate about a mean of 35.6%, with one notable peak in the NW attributable to the grounds of the power substation where the flux tower is located. In contrast, traffic counts are highly spatially-dependent, with highest values in the SE wind direction (averaging at 11.6 m (driven) m^{-2} h^{-1} for this sector), and lowest in the SW and NW (average of 3.7 m (driven) m^{-2} h^{-1}). This demonstrates the effects of busy arterial roads compared to residential streets on the spatial variability of emission sources.

Total vegetation fractions are highest in the SW-NW (180-360^{o}) (32.7% on average), and lowest in the NE-SE (0-180^{o}) (26.6% average) wind sectors, where a large impervious lot exists, as well as the presence of many commercial buildings along Knight Street. Not surprisingly, peaks in vegetation fractions correspond with lower impervious ground and building fractions, and troughs correspond with higher impervious ground and building fractions. The highest building fractions are in the SE-SW wind sectors, averaging at 24.7%, and the lowest fractions are found in the NW (17.5% average), as this sector contains the impervious grounds of the BC Hydro substation within which the EC tower is situated (in the SE corner), and where no buildings exist.

The footprint-averaged surface fractions were also plotted for stable conditions (Figure B.1 in Appendix B). Under stable conditions, flux footprints extend further from the tower, and potentially allow the tower to measure surface characteristics not detected under unstable conditions. However, Figure B.1 shows that footprint-averaged surface fractions change very little, both in magnitude and in direction, for stable conditions compared to unstable conditions. This is useful, as it means analysis of certain wind directions can be directly linked to surface characteristics in that direction, regardless of stability regimes.

3.1.2 Climatology

The study site is located in the coastal city of Vancouver, Canada, approximately 10 km from the ocean. Characteristic climate regimes for the area include mild, wet winters and dry summers. The dry summers regularly manifest in water budget deficits, which encourages lawn irrigation in many yards (Jarvi et al., 2011, Oke et al., 2017). Differential heating during the summer also promotes a strong temperature gradient between the ocean and the land, creating land and sea breezes. These are apparent in the wind roses (Figure 3.2); Strong winds from the SW are common during day, particularly in summer when ocean breezes are prominent (Steyn and Falkner 1986, van der Kamp and McKendry 2010, Leroyer et al., 2014, Crawford and Christen 2015). In the morning and at night, SE flows are common, and occur likely as a result of colder, land breezes. The nighttime winds from the NE are evident, and may indicate land breezes or, more likely, drainage flows as NE winds occur more frequently in winter when the sea and land breeze system is weaker or entirely absent. Average monthly wind speeds typically fall between 2 – 3 m s^{-1}. Winter winds are typically from the NE, and summer winds are commonly from the SE, which has been found by other studies for this site (Figure 3.2) (Crawford and Christen 2015).

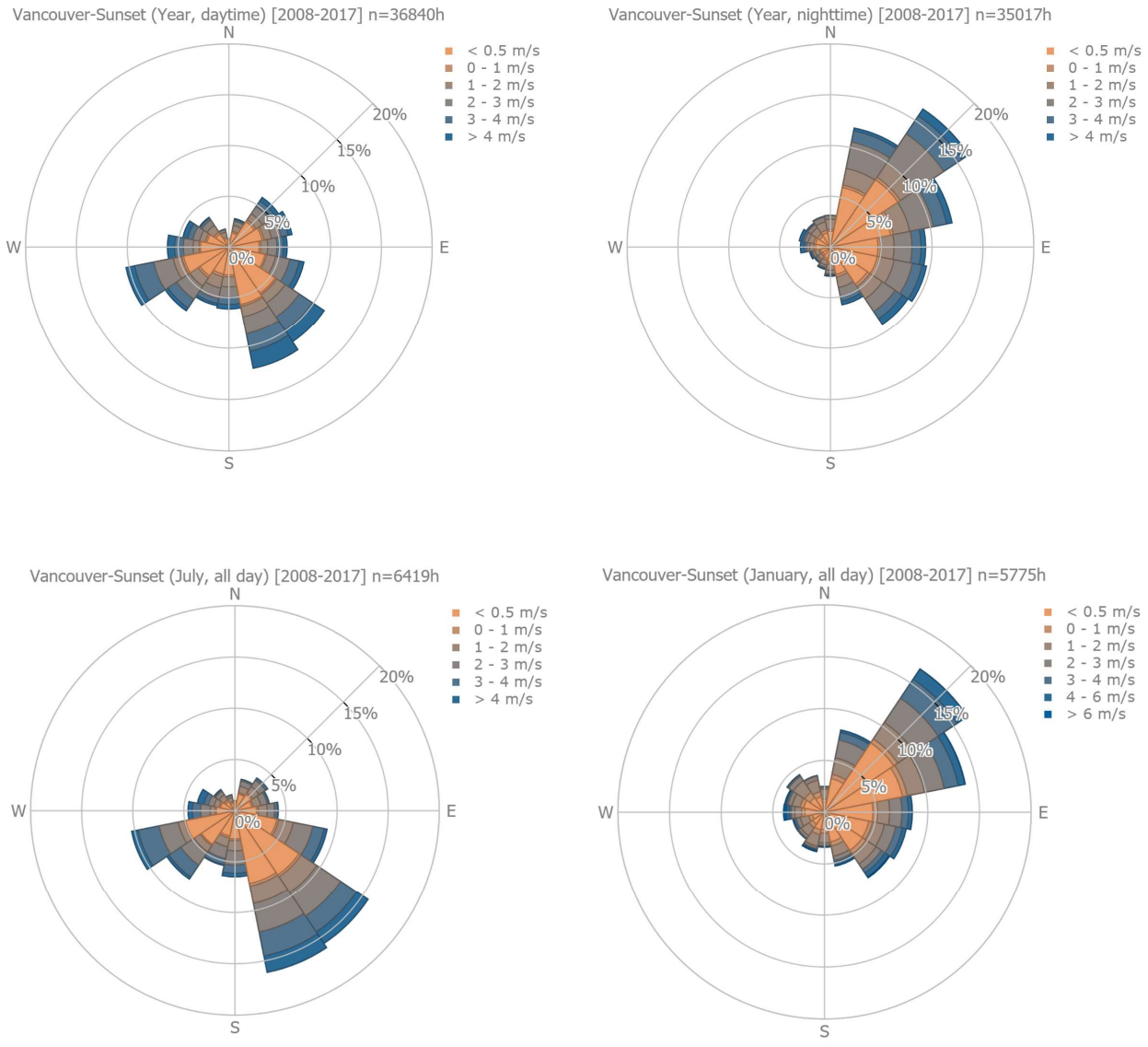

Figure 3.2: (Top) Annual wind roses generated for the study area for the daytime (left), and nighttime (right) cases. (Bottom) Average daily wind roses for the summer month of July (left), and the winter month of January (right). (Image created by Andreas Christen and taken with permission from http://ibis.geog.ubc.ca/~achristn/data/windroses/ST/index.html)

Table 3.1 provides average air temperatures, average monthly precipitation amounts, and averaged soil water content over the 2008 – 2016 study period, grouped by month. Highest air temperatures occur in the summer months of June, July, and August, and lowest temperatures are during winter (December, January, and February). Precipitation is highest between October and March. Soil water content follows a similar trend as precipitation, with slightly less variation as anthropogenic emissions like irrigation add moisture in the dryer months (Oke et al., 2017). The minimum Bowen ratio (based on daily mean Q_H and Q_E) of 0.72 occurs in December, when there is an abundance of water at the surface, and temperatures are low. The maximum Bowen ratio of 3.11 is during July, when conditions are dry and hot. Largest heating degree day (HDD) temperatures occur during winter, when daily net radiation and temperatures are lowest.

Table 3.1: Monthly and annual statistics for the May 5, 2008–May 5, 2016 period of which 77.94% of data was valid, measured at Vancouver-Sunset. Values are not stratified by wind direction or atmospheric stability. Acoustic air temperature measurements made at the top of the tower are used for the air temperature and HDD values. Note the annual total precipitation is given, rather than the annual average. The Bowen ratio values are based on average daily fluxes of Q_H and Q_E.

Month	Mean daily air temperature (ºC)	Mean precipitation (mm month^{-1})	Mean soil water content (%)	Bowen Ratio	HDD (ºC)	Mean daily net radiation (W m^{-2})
January	3.95	130.46	37.53	1.12	11.05	2.49
February	5.23	83.19	37.07	1.58	9.78	23.71
March	6.98	136.46	38.01	1.64	8.02	59.53
April	10.31	85.36	32.78	2.20	4.80	108.84
May	13.82	65.97	26.57	2.15	2.02	144.87
June	16.49	41.96	21.07	2.28	0.49	153.26
July	19.65	21.27	13.54	3.11	0.03	165.10
August	19.46	38.08	12.00	3.04	0.02	130.92
September	16.06	67.27	17.67	2.18	0.54	86.92
October	11.29	106.30	27.71	1.56	3.82	36.29
November	6.03	130.56	35.52	1.37	8.97	7.22
December	3.38	132.47	36.62	0.72	11.61	-4.36
Annual Average [annual total]	11.05	[1039.35 mm year^{-1}]	28.00	1.91	5.10	76.23

3.1.3 Fluxes

3.1.3.1 Wind direction

Fluxes vary as a function of surface processes, which can have spatial and temporal dependencies. To explore temporal and spatial variation, Figure 3.3 presents the fluxes, Q_H, Q_E, $u'w'$, and F_C, as a function of wind direction for both the daytime and nighttime cases.

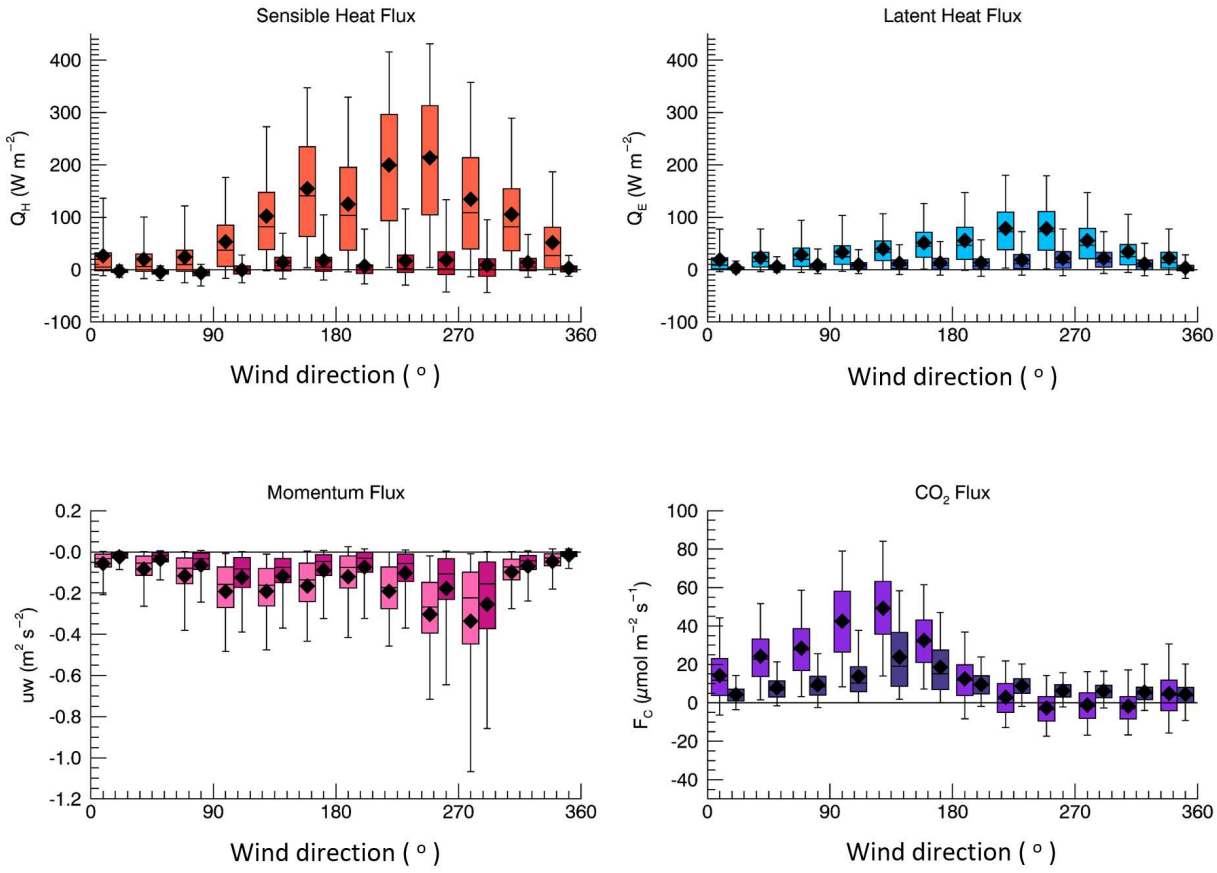

Figure 3.3: Changes in daytime (50.18% valid data) and nighttime (49.81% valid data) Q_H, Q_E, $u'w'$, and F_C as a function of wind direction. In each case, the lighter orange, light blue, pink, and violet boxes show the daytime (6:00 – 18:00 PST) Q_H, Q_E, $u'w'$, and F_C, respectively, while the darker boxes represent the nighttime (18:00 – 5:00 PST) values. All stabilities are considered.

Sensible heat flux (Q_H) is highest in the SW during the day, and lowest in the NE. The average annual daytime value over all wind directions is 100.9 W m^{-2}, with an average maximum value of 213.6 W m^{-2}. Lowest values occur at night, when the atmosphere is stably stratified, and no solar energy is available, facilitating longwave (heat) energy loss which often results in negative Q_H values. Latent heat flux (Q_E) follows a similar trend to Q_H, with largest values from the SW and west directions. The magnitude of flux is much smaller for Q_E compared to Q_H, with an average annual daytime Q_E value of 43.3 W m^{-2}, and a nighttime value of 11.8 W m^{-2}.

Momentum flux is nearly always toward the surface (negative values), with the largest fluxes in the west. The smallest values are in the NE, where an empty gravel lot is located, decreasing the friction velocity (u_*) at the surface, and, therefore, the momentum flux.

The highest CO_2 fluxes (F_C) originate from the SE wind direction (90-180°), which was similarly found by Walsh (2005), Christen et al. (2011), and Crawford and Christen (2015) for this site. Under unstable atmospheric conditions, the average F_C from this wind sector is 35 µmol m^{-2} s^{-1}, which is on average 59% higher than the NE, 89% higher than the SW, and 99% higher than the NW wind sectors.

Seasonal trends show sensible heat fluxes vary significantly between seasons (Figure 3.4). Spring and summer have the largest fluxes, and the greatest variation in range with wind direction. Winter and fall vary to a lesser extent. Latent heat follows a similar trend, with much lower fluxes. Momentum fluxes are larger in spring and summer, resulting from drag imposed by vegetation.

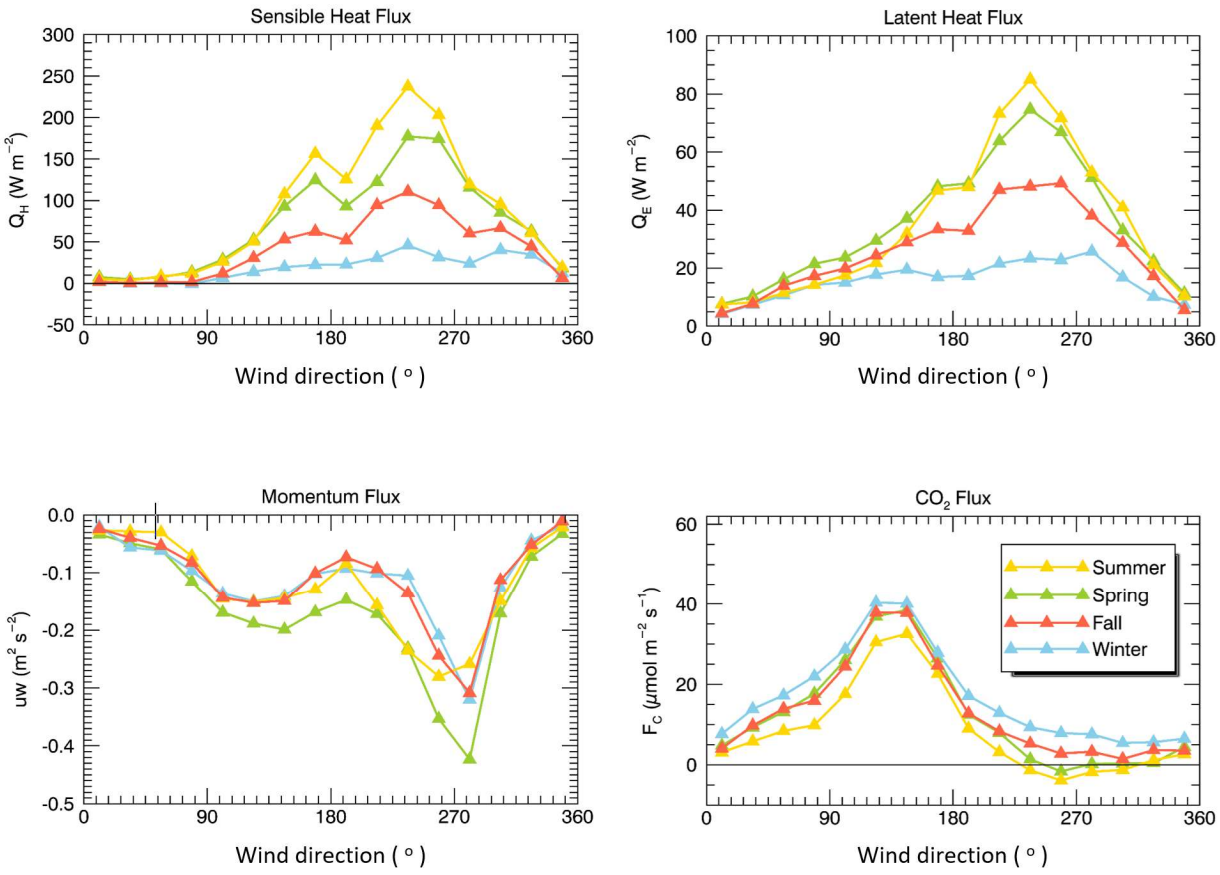

Figure 3.4: Fluxes of Q_H, Q_E, $u'w'$, and F_C as a function of wind direction, for daytime hours (50.18% of all valid data), and broken into seasons. All stabilities are considered. Note the different y-axes.

Greater seasonal variation in F_C is observed in the SW and NW sectors compared to the SE and NE. The higher F_C values in the SE correspond with higher footprint-averaged traffic counts for this sector, and the lower (and more seasonally-variable) F_C in the SW-NW correspond with higher vegetation amounts, which act as a net sink of CO_2 particularly during the spring and summer when leaves are present (refer to Figure 3.1 above for footprint analysis).

3.1.3.2 Diurnal trends

Diurnally, sensible heat fluxes are close to zero at night and steadily increase over the course of the day, reaching a maximum average of 252.90 W m^{-2} around 13:00 PST, as the sun heats surfaces

(Figure 3.5). Unlike sensible heat, average latent heat fluxes remain, on average, positive at night. This may be attributable to a reduction in dewfall that has been observed to occur in cities relative to rural areas, which maintains a surplus of moisture in the urban atmosphere (Oke et al., 2017); Proposed explanations for this reduction in dewfall include the retention of heat over cities resulting from the nocturnal surface UHI, which prevents sufficient cooling of urban surfaces and impedes condensation, and the increased sheltering of the urban canopy layer which inhibits deposition of atmospheric water vapour at the surface (Oke et al., 2017). Further, anthropogenic injections of water vapour, like vehicle emissions and irrigation, may also maintain net positive water vapour fluxes over cities at night. The midday peak of 93.67 W m^{-2}, smaller in magnitude compared to sensible heat, occurs at the same time as the peak in sensible heat. This is expected as water vapour is a passive scalar, relying partly on thermally-produced eddies to transport it to the atmosphere, and because of a lack of surface water in urban environments.

Momentum flux is nearly always negative, and depends greatly on wind speed and the roughness of the surface (Nordbo et al., 2013). CO_2 fluxes tend to be lower at night, particularly in the very early hours of the morning. Two prominent peaks in the upward transfer of CO_2 are evident at around 08:00 and 17:00 PST. At midday, mean upward flow declines, and some downward fluxes are visible.

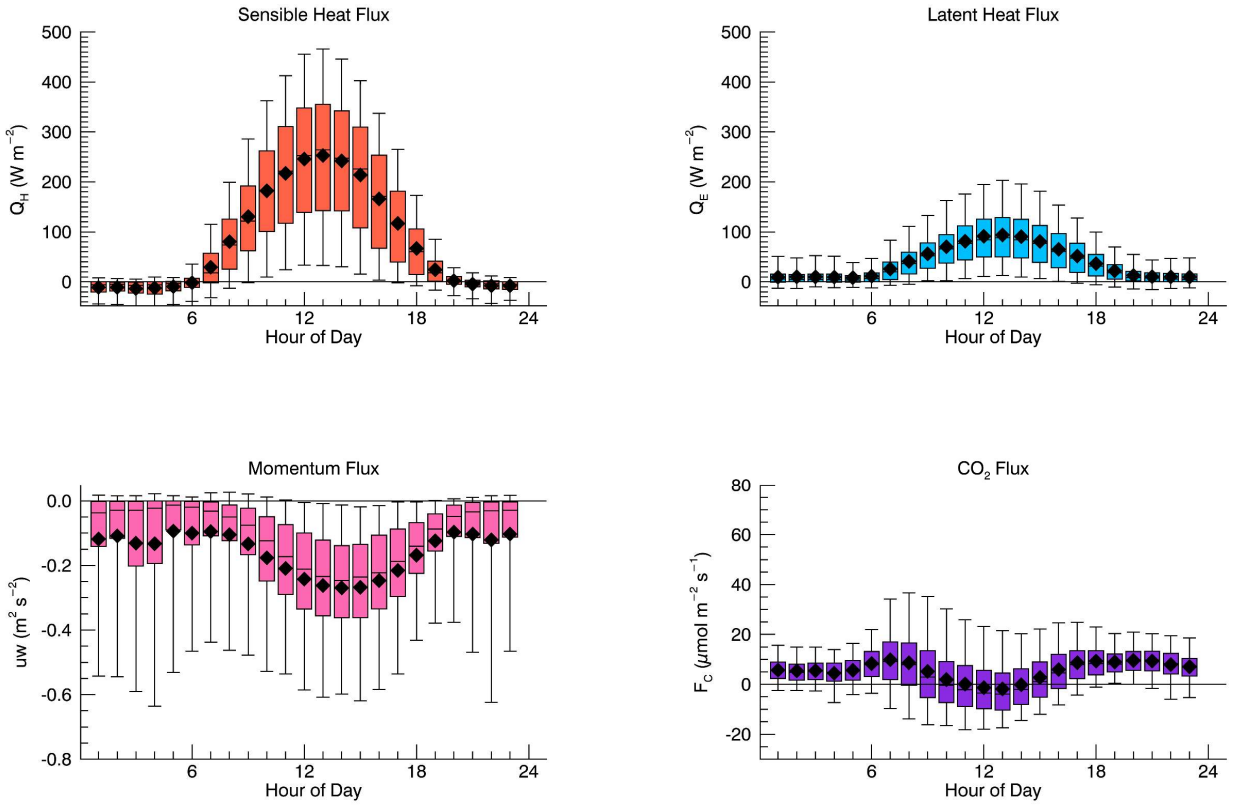

Figure 3.5: Fluxes of Q_H, Q_E, $u'w'$, and F_C over the day, for all stabilities, and the SW wind sector only (21.82% of valid data).

As fluxes are subject to the complex spatial and temporal variation of sources and sinks at the surface, identifying the processes that influence daily fluxes is speculative. The morning and evening peaks in CO_2 flux are likely a product of rush-hour traffic, and the downward fluxes around noon are indicative of photosynthetic uptake by vegetation (Jarvi et al., 2012).

Weekday (Monday-Friday) fluxes of CO_2 were compared to weekend (Saturday-Sunday) fluxes (Figure 3.6). Average weekday fluxes for all wind directions (7.2 µmol m^{-2} s^{-1}) are 47% higher than weekend fluxes. In the SE wind sector, weekday fluxes are 81% higher than the average NE, NW, and SW sectors, and 30.4% higher than weekend fluxes for the SE. These results are consistent with previous

analyses of F_C for this site (Walsh 2005, Crawford and Christen 2015).

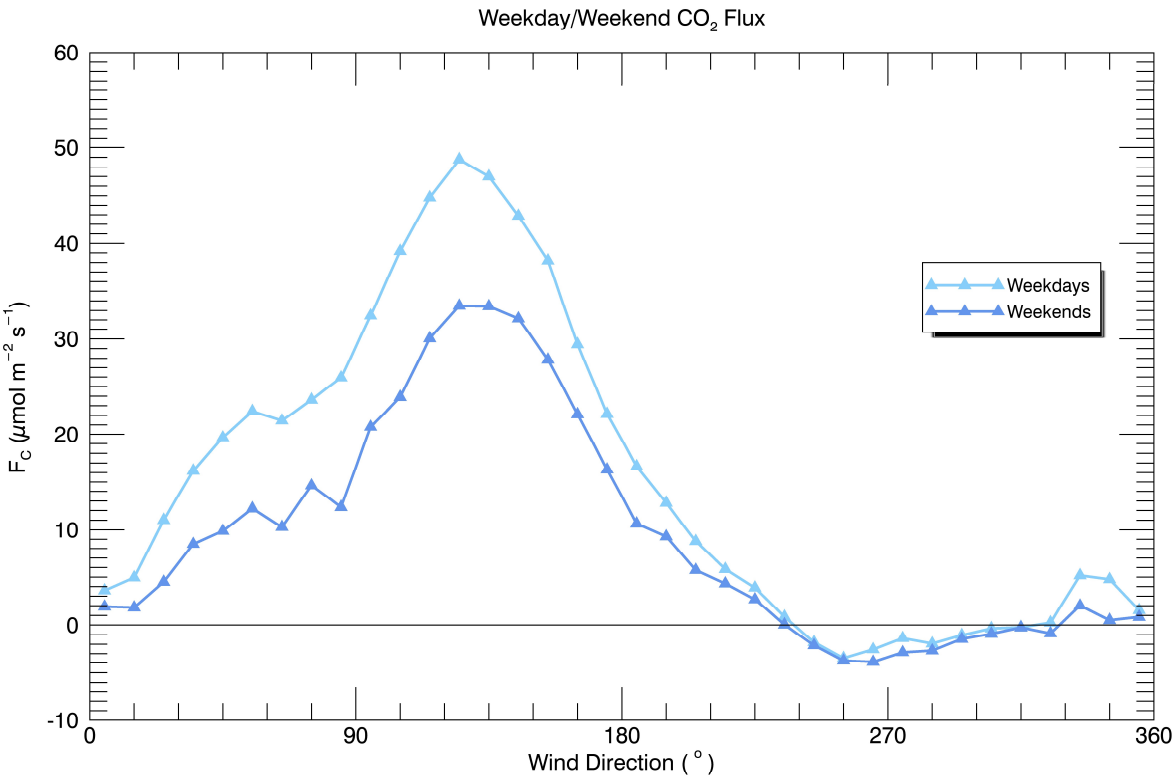

Figure 3.6: Weekend and weekday F_C under unstable conditions, plotted against wind direction.

3.1.3.3 Annual trends

Long-term annual trends in sensible heat flux (Q_H), latent heat flux (Q_E), CO_2 flux (F_C), and momentum flux ($u'w'$) were explored. Table 3.2 presents average monthly fluxes for sensible and latent heat, momentum, and CO_2, based on the full eight years of flux data, and Figure 3.7 examines the annual trend in Q_H, Q_E, $u'w'$, and F_C after stratifying data to consider the SW wind sector only.

Table 3.2: Average daily fluxes of sensible heat (Q_H), latent heat (Q_E), momentum ($u'w'$), and CO_2 (F_C) for each month, over the eight-year study period (based on the 77.94% of valid data). Annual daily averages are presented at the bottom. All stabilities and wind sectors are considered in this table.

Month	Q_H (W m^{-2})	Q_E (W m^{-2})	$\overline{u'w'}$ (m^2 s^{-1})	F_C (µmol m^{-2} s^{-1})
January	15.73	14.60	-0.10	17.83
February	33.46	22.34	-0.14	17.56
March	60.76	30.82	-0.17	15.49
April	86.69	39.07	-0.17	13.17
May	100.98	44.48	-0.16	13.66
June	113.86	43.00	-0.16	13.81
July	109.28	37.25	-0.14	13.63
August	79.04	31.58	-0.11	13.48
September	45.02	25.92	-0.10	14.05
October	19.88	19.70	-0.11	16.37
November	7.27	14.88	-0.11	18.82
December	5.96	12.21	-0.10	19.12
Annual Average	56.49	27.99	-0.13	15.58

For the SW wind sector, increased fluxes of sensible heat are observed in summer (June – August), when days are longer and the zenith of the sun is such that the three-dimensional urban surface is more exposed to solar radiation and heating. Peak Q_H occurs in July, reaching an average maximum of 238.16 W m^{-2}. Fall (September – November) and winter (December – February) values are the lowest, when days are shorter.

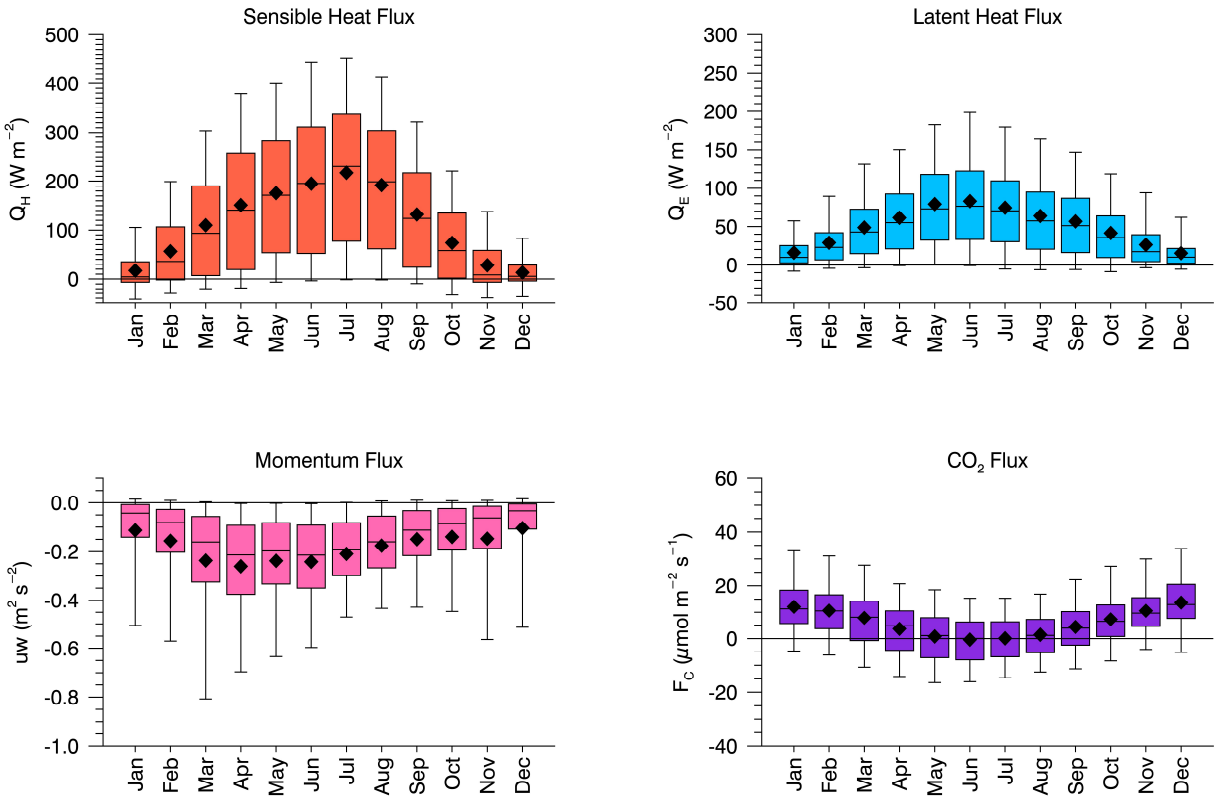

Figure 3.7: Monthly fluxes of Q_H, Q_E, $u'w'$, and F_C over the eight-year study period, and stratified to consider only the SW wind sector (all stabilities are considered) (21.82% of valid data).

Highest Q_E values are observed in the spring (March – May), and lowest values are during winter. During spring, leaves are out and evapotranspiration is possible, enhancing the upward flux of water vapour. This is augmented by high springtime precipitation amounts (see Table 3.1 above). While winter precipitation is high, Q_E fluxes are low, likely resulting from the reduced energy available, limiting the amount of transported water vapour to the atmosphere.

Momentum flux is toward the surface at all times of the year, and highest in spring and early summer, with lowest values in late fall and winter. In spring, increased drag caused by leaves on vegetation may increase momentum flux. During summer when increased occurrence of winds from this SW sector are present, the urban form, in part consisting of a large percentage of buildings, leads to the

enhanced downward flux.

F_C values show less monthly variation over the year, and values are similar to those listed in Christen et al. (2011) for the same site, based on two years (2008 – 2010) of flux data. There is a slight increase in the upward flux during winter, particularly in December. The cold temperatures in the wintertime result in more homes switching on their natural-gas heating systems, which emit additional CO_2 when combustion occurs (Christen et al., 2011).

3.1.4 Stability

Atmospheric stability in urban areas tends to behave differently compared to rural areas, and exhibits variation over space, even within the same city, resulting from surface characteristics and spatial-temporal distributions of heat sources (Nordbo et al., 2013). Of the eight years of data, stabilities that fell between $-10 < z'/L < -0.1$ (unstable) occurred 41.83% of the time, $0.1 < z'/L < 10$ (stable) occurred 24.67% of the time, and $-0.1 < z'/L < 0.1$ (neutral) conditions occurred 18.93% of the time. Unstable conditions, or $z'/L < -0.01$, being found most often supports previous findings by Grimmond et al. (2004) for urban areas.

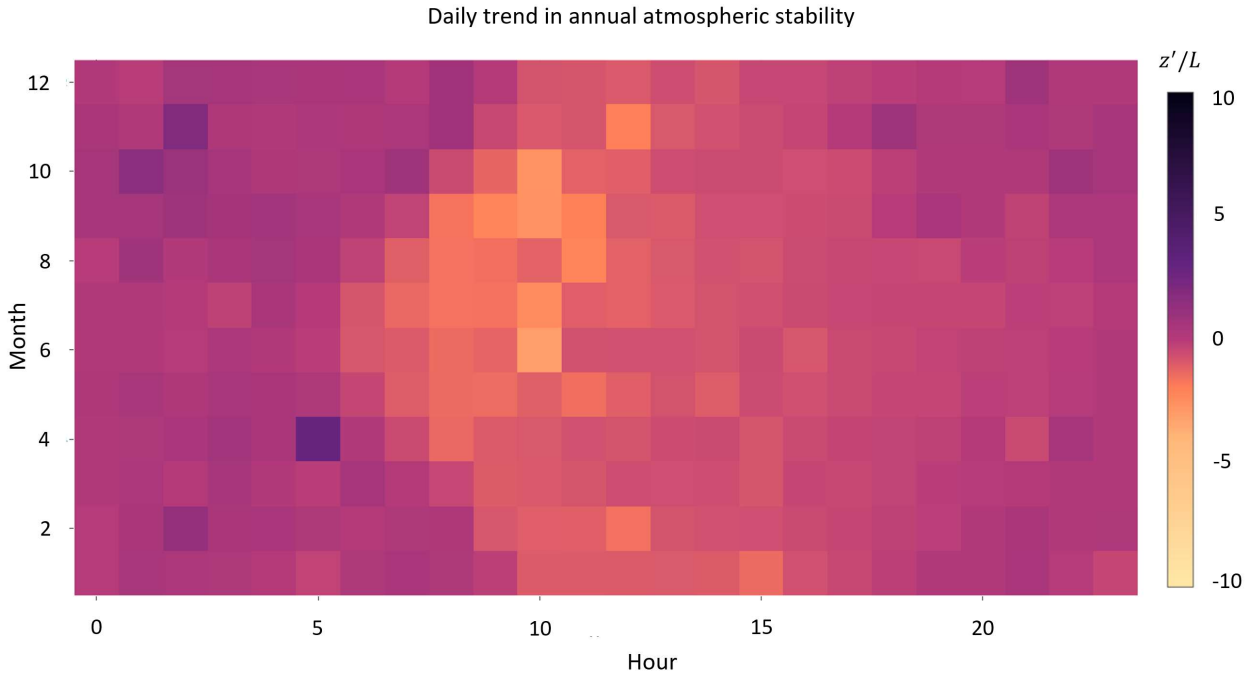

Figure 3.8: Stability (z'/L) as a function of hour of the day (x-axis) and day of the year (y-axis), for all wind directions. Unstable conditions are shown in orange, while stable conditions are in dark violet.

Figure 3.8 shows stable conditions, or $z'/L > 0.1$, mostly occur at night. Instances of stabilities greater than 1 or 2 are rare, with neutral or unstable stratification occurring most commonly over the year and over the day. Unstable conditions occur mostly during the day, resulting from solar heating of the surface which results in buoyant and shear production (Li and Bou-Zeid 2011). These results are in keeping with previous studies on atmospheric stability in urban areas (Arnfield 2003, Nordbo et al., 2013).

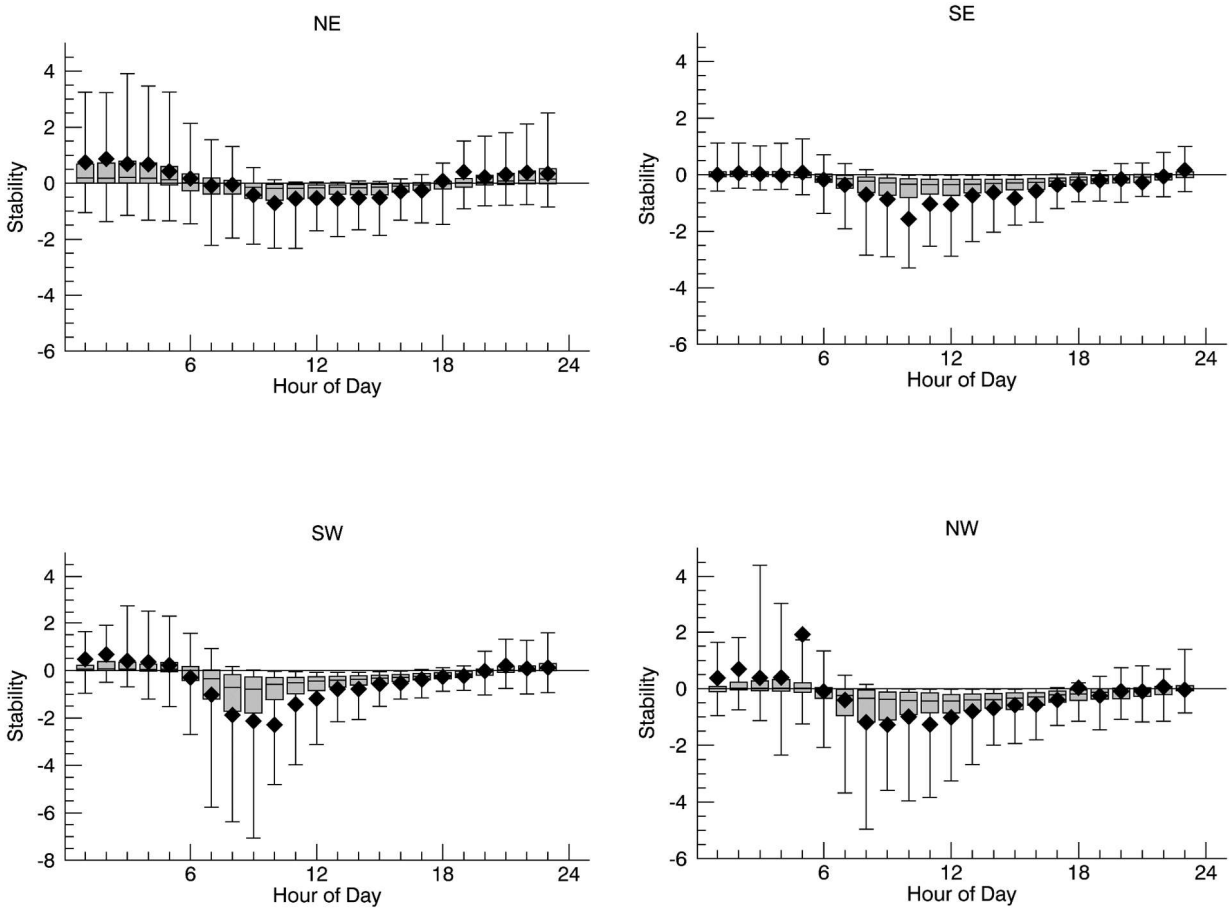

Figure 3.9: Diurnal trend in stability regimes for each wind sector using all eight years of data. Note stability has not been log-transformed.

Figure 3.9 shows that even during the night, there are instances of neutral and unstable conditions which was similarly found by Christen and Vogt (2004). The SE wind sector exhibits the least diurnal variation in stability, while the SW and NW sectors show the greatest variation.

Figure 3.10 (a) presents a breakdown of the percent occurrence of each stability regime (b) for each wind sector over the eight years.

a)

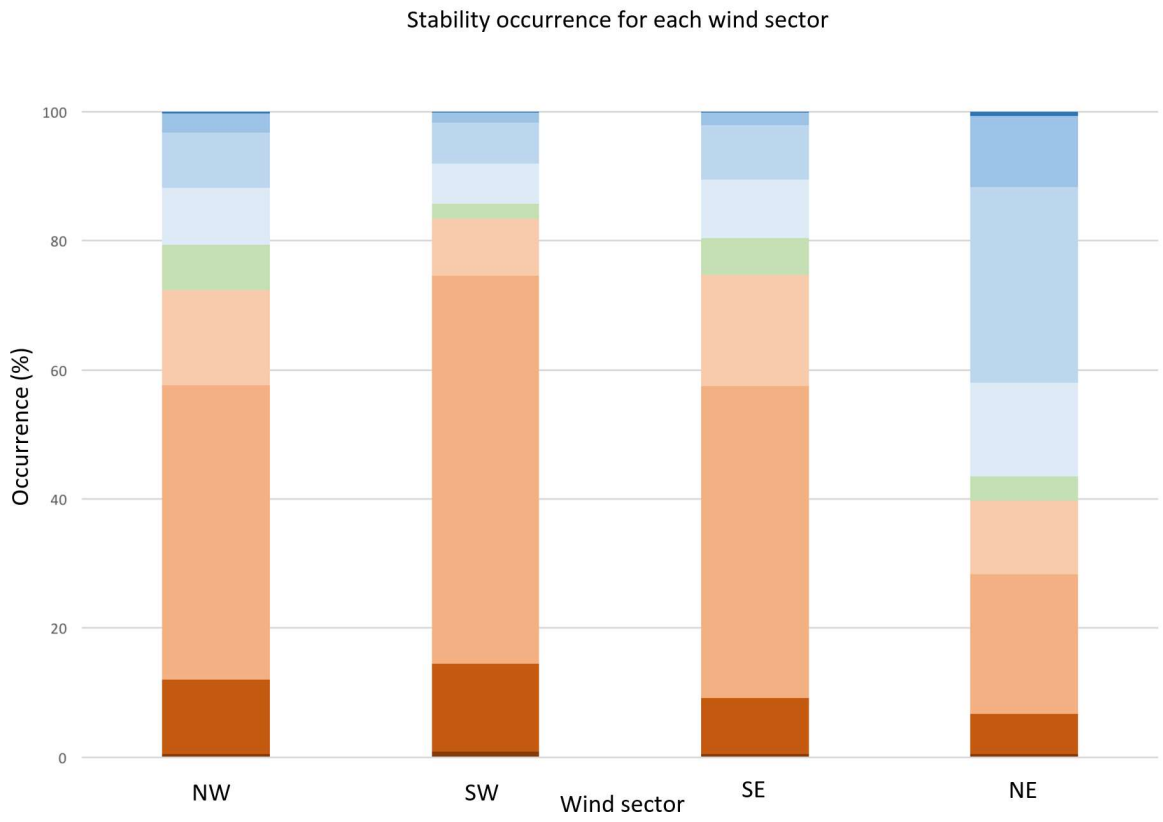

b)

$(z')/L$	Class
Less than -10	very unstable
-10 to -1	unstable
-1 to -0.1	moderately unstable
-0.1 to -0.01	slightly unstable
-0.01 to 0.01	neutral
0.01 to 0.1	slightly stable
0.1 to 1	moderately stable
1 to 10	stable
Greater than 10	very stable

Figure 3.10 a and b: Percent occurrence of unstable, stable, and neutral atmospheric conditions over the eight years of flux data measured at Vancouver-Sunset (a), with definitions of each stability class (b).

In the NW, SW, and SE wind sectors, moderately unstable conditions dominate. The NE sector contains the most frequent occurrence of stable conditions. Figure 3.9 shows that in the NE sector, stable conditions occur well into the late morning, while in most other sectors unstable conditions begin earlier. As indicated by Figure 3.2, winds typically originate from the NE sector during winter, and Figure 3.11 below shows that winter has the highest frequency of stable conditions of any time of year. Furthermore, the frequency of nighttime winds from the NE may increase the occurrence of stable conditions.

The SW wind sector presents the most frequent occurrence of unstable conditions. The sea breeze coming from the SW during day may bring with it warm air as it passes over warm urban surfaces and sources of anthropogenic heat, resulting in high occurrence of unstable (z'/L < -1) conditions.

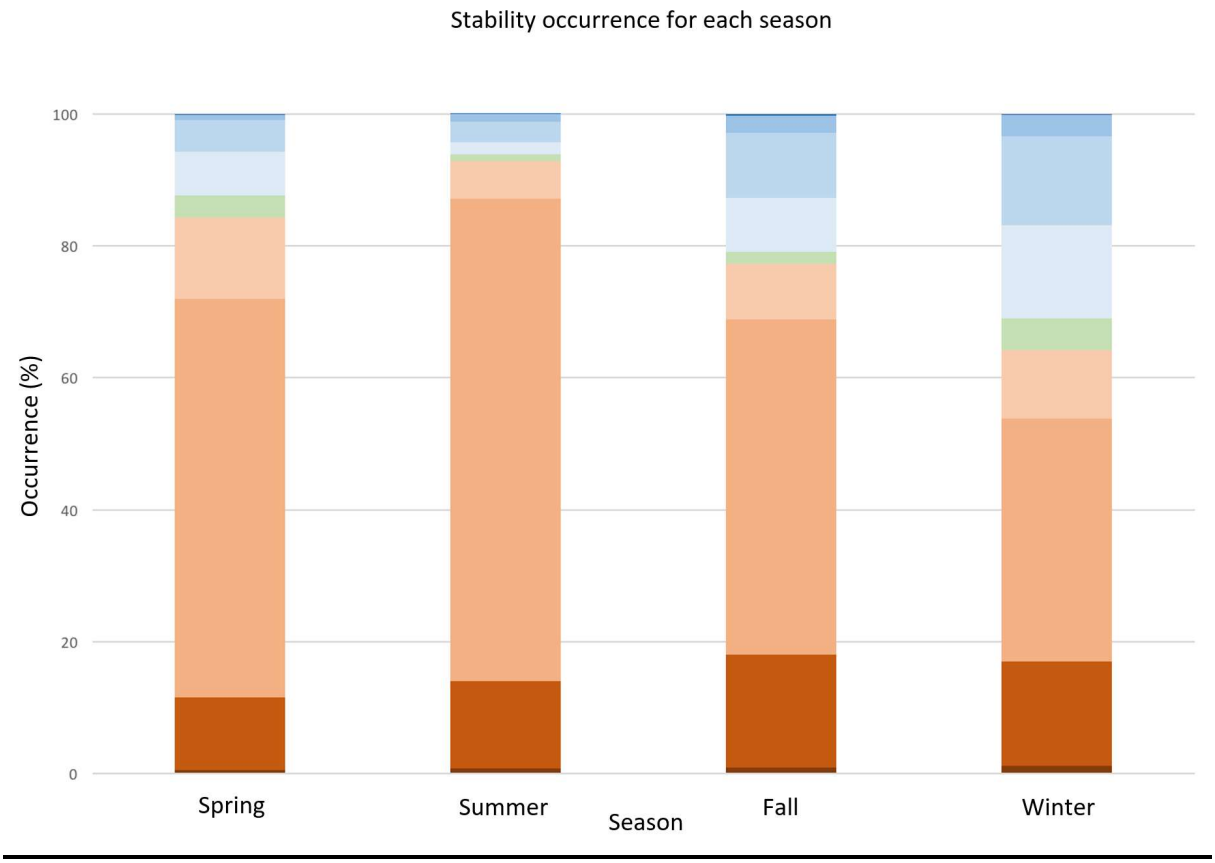

Figure 3.11: Frequency in the occurrence of each stability class, for the SW wind sector only, broken into seasons. Refer to Figure 3.10 (b) for legend of stability classes represented here.

The occurrence of each stability class over the 24 hours during each season is plotted for the SW wind direction in Figure 3.11. Stable conditions occur more frequently in the fall and winter, and unstable conditions are more frequent in spring and summer. Especially in the case of summer, when surface water availability is reduced and sensible heat dominates, thermal energy drives the productions of more unstable conditions (Nordbo et al., 2013). Moderately unstable conditions happen most frequently in summer, and least frequently in winter. In summer, days are longer with daytime hours dominating, and as Figure 3.8 indicates, unstable conditions occur mostly during the day. Similarly, stable conditions occur mostly at night, which explains the higher occurrence of stable conditions in winter, when days are shorter and night dominates. Neutral stratification is similarly frequent in spring and fall, with summer experiencing rarer occurrences of neutral conditions, and winter experiencing the most as Q_H is lower, and higher winter winds favour neutral conditions.

3.2 Effects of stability on turbulent exchange efficiency

Departures of the correlation coefficients of sensible heat, water vapour, momentum, and CO_2 (r_{wT}, r_{wh}, r_{uw}, and r_{wc}, respectively) from Monin-Obukhov similarity theory (MOS) predictions is well established over urban areas (Roth and Oke 1995, Roth 2000, Detto et al., 2008). MOS predicts that heat and passive scalars are equally exchanged by the same turbulent structure over homogeneous landscapes, but this assumption falls apart over urban areas. Studies on turbulent exchange over cities have emphasized the role of atmospheric stability in moderating source area size and orientation, which can affect the extent to which surface heterogeneity influences fluxes of energy, mass, and momentum, and can contribute to dissimilarities in momentum and scalar exchange (Roth 2000). As such, analysis of the effects of stability regimes on dissimilarities in momentum and scalar transport efficiencies is a fundamental first step in addressing spatial and temporal heterogeneity.

3.2.1 MOS predictions

MOS predicted values of r_{uw} and r_{wT} were determined using calculated normalized standard deviations for horizontal wind (A_u), vertical wind (A_w), and temperature (A_T), based on MOS-predicted semi-empirical constants a_i, b_i, and c_i for urban areas using Equations 13 and 14 (Section 2.2) following Roth (2000). Similarly, adjusted urban values, and typical surface layer values of a_i, b_i, and c_i were taken from Oke et al. (2017) and used to calculate r_{uw} only.

The exchange efficiencies for sensible heat, water vapour, momentum, and CO_2 were plotted separately for stable and unstable conditions (Figure 3.12). MOS-predicted r_{uw} and r_{wT} from Roth (2000) and Oke et al. (2017) were overlaid to compare eight years of actual flux data from Sunset Tower to the compiled values for the urban ISL and surface layer.

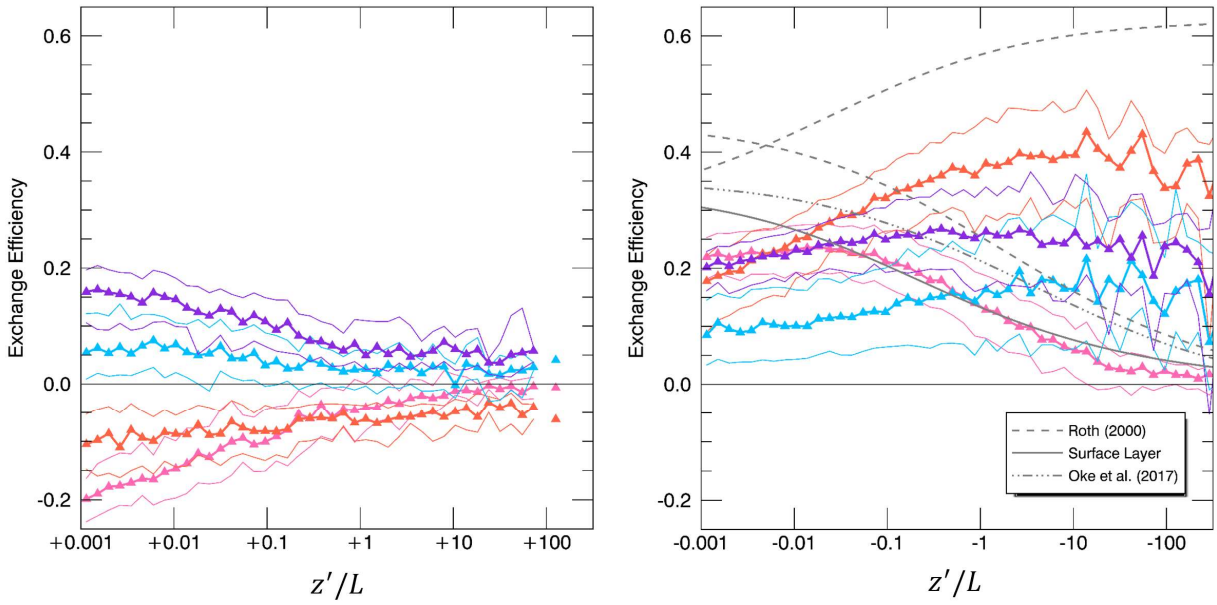

Figure 3.12: Calculated median r_{wT}, r_{wh}, r_{uw}, and r_{wc} versus log-transformed stability, for stable (left) and unstable (right) conditions, for the SE wind sector (see Appendix B for NE, SW, and NW wind sectors). Calculated values are based on all eight years of flux data. The orange, light blue, pink, and violet lines represent r_{wT}, r_{wh}, r_{uw}, and r_{wc}, respectively. The coloured bands show the 25th to 75th percentile ranges. The overlaid gray lines are the MOS-predicted values, based on compiled urban values of r_{uw} and r_{wT} following Roth 2000, the adjusted urban ISL values for r_{uw} only from Oke et al. (2017), and the surface layer values for r_{uw} only from Oke et al. (2017). Note the sign for r_{uw} has been flipped (multiplied by -1) for the unstable case.

The SE wind sector (90–180°) is pictured here as the surface layer (SL) prediction for momentum exchange conforms best to the actual measured efficiency in this wind sector. The SE wind sector has the highest roughness lengths of all wind directions, especially during the leaves-on season (other wind sectors are shown in Appendix B).

For the stable case, when conditions are close to neutral ($z'/L < 0.1$), the dissimilarity in exchange efficiency between momentum and the scalars is most evident compared to $z'/L > 0.1$. Both CO_2 and water vapour are transferred towards the atmosphere, while sensible heat and momentum move toward the surface, as previously found by other studies (Wang et al., 2014). CO_2 shows the largest positive (upward) exchange efficiency (average median value of 0.15), while momentum shows the

largest negative (downward) exchange efficiency (average median value of -0.18). Sensible heat exchange (average median value of -0.095) is slightly more efficient that water vapour exchange (average median value of 0.058), but the two are directionally opposite each other, with water vapour flowing into the atmosphere, and heat flowing toward the surface. At $z'/L > 1$, r_{wT}, r_{wh}, and r_{uw} drop below that of r_{wc} (average median values of -0.052, 0.025, -0.019, and 0.054, respectively), although downward sensible heat exchange is nearly as efficient as upward CO_2 exchange. As conditions become significantly more stable, the dissimilarity in the correlation coefficients diminishes, and efficiencies all approach zero.

The neutral limits for r_{wT}, r_{wc}, and r_{uw} have very similar values, averaging around 0.20, 0.21, and 0.22, respectively. r_{wh} has the lowest efficiency, with an average median value of 0.096. Instability influences the correlation coefficients of water vapour and sensible heat in the same way, although values of r_{wh} are much smaller in magnitude (as was found by Moriwaki and Kanda 2006). As conditions become increasingly unstable ($-100 < z'/L < -1$), exchange efficiencies exhibit greater dissimilarity, with median r_{wT} averaging at 0.38, r_{wh} at 0.17, r_{uw} at 0.047, and r_{wc} at 0.24. More generally, as instability increases, the efficiency of upward transfer of sensible heat and water vapour increases, CO_2 initially increases and then begins to drop slightly, while momentum becomes decreasingly efficient, eventually approaching zero. The increasingly disparate exchange at very unstable conditions may be attributable to the highly-variable size and shape of the turbulent source area under these conditions; Under unstable conditions, flux footprints are more constrained to the immediate vicinity of the tower, where the spatial scale of surface properties is small enough that surface source/sink heterogeneity becomes increasingly important (Roth 2000).

All three predictions (SL, Roth (2000), and Oke et al. (2017)) overestimate exchange efficiency for momentum and/or sensible heat when $z'/L > -0.01$. When $z'/L < -0.01$, the SL prediction correctly predicts r_{uw}, while the other two predictions (Roth (2000) and Oke et al. (2017)) continue to overestimate r_{uw} and/or r_{wT}.

At the neutral limit, highest correlations coefficients for momentum and scalars exists. As atmospheric conditions become increasingly unstable, the scalars (r_{wT}, r_{wh}, and r_{wc}) are exchanged more efficiently than momentum, which is consistent with previous studies (Li and Bou-Zeid 2011). Wang et al. (2014) found that r_{wh}, and r_{wc} are less affected by changes in atmospheric stability than are r_{wT} and r_{uw}. The above analysis shows this to be the case. They also found that as instability increases, r_{uw} decreases, which is likewise apparent in Figure 3.12.

r_{wT} is smaller compared to r_{wc} under stable conditions, which in part supports previous findings for an urban area (Nordbo et al., 2013). However, r_{wT} is consistently larger than r_{wh} under stable conditions. Further, while r_{wT} exhibits large variations as a function of stability, both CO_2 and water vapour change little with stability. While water vapour and CO_2 are both passive scalars, r_{wc} is consistently higher than r_{wh} over all stabilities. This is in stark contrast to the results obtained by Moriwaki and Kanda (2006) over a suburban city in Japan, where they found CO_2 to be much less efficiently transferred compared to water vapour. This implies that stability alone does not explain differences in scalar transport efficiencies, and that characteristics of the urban source/sink configurations and strengths play a key role. For example, source strength of CO_2 emissions in this study are higher compared to those in Moriwaki and Kanda (2006).

Despite surface characteristics changing significantly with each wind sector, the exchange efficiencies vary little with each sector under stable conditions (see Appendix B for plots of the NE, SW, and NW). Therefore, under stable conditions, stability primarily moderates the exchange of momentum and scalars. In contrast, under unstable conditions, r_{wT}, r_{wh}, r_{uw}, and r_{wc} vary greatly with stability between the sectors, and exhibit significant dissimilarities in exchange efficiency. Thus, it can be said that the exchange efficiency of momentum and scalars is mainly influenced by surface heterogeneity rather than stability under unstable atmospheric conditions.

This conclusion is in agreement with speculations made by a number of other studies on the dissimilarity of momentum and scalar transport. Moriwaki and Kanda (2006) explained the dissimilarity in transport efficiencies between the passive scalars, CO_2 and water vapour, and sensible heat via the presence of coherent thermal structures that consistently transport heat (under unstable conditions), but only transport CO_2 and water vapour if they are present in the source area over which the thermal structure passes.

3.2.2 Ratios of the correlation coefficients

An analysis was performed on the ratios of r_{wh}/r_{wT} and r_{wc}/r_{wT} for stable and unstable conditions to further examine the observed disparity between stability's effects on the passive scalars (r_{wc} and r_{wh}) and the active one (r_{wT}) (Figure 3.13).

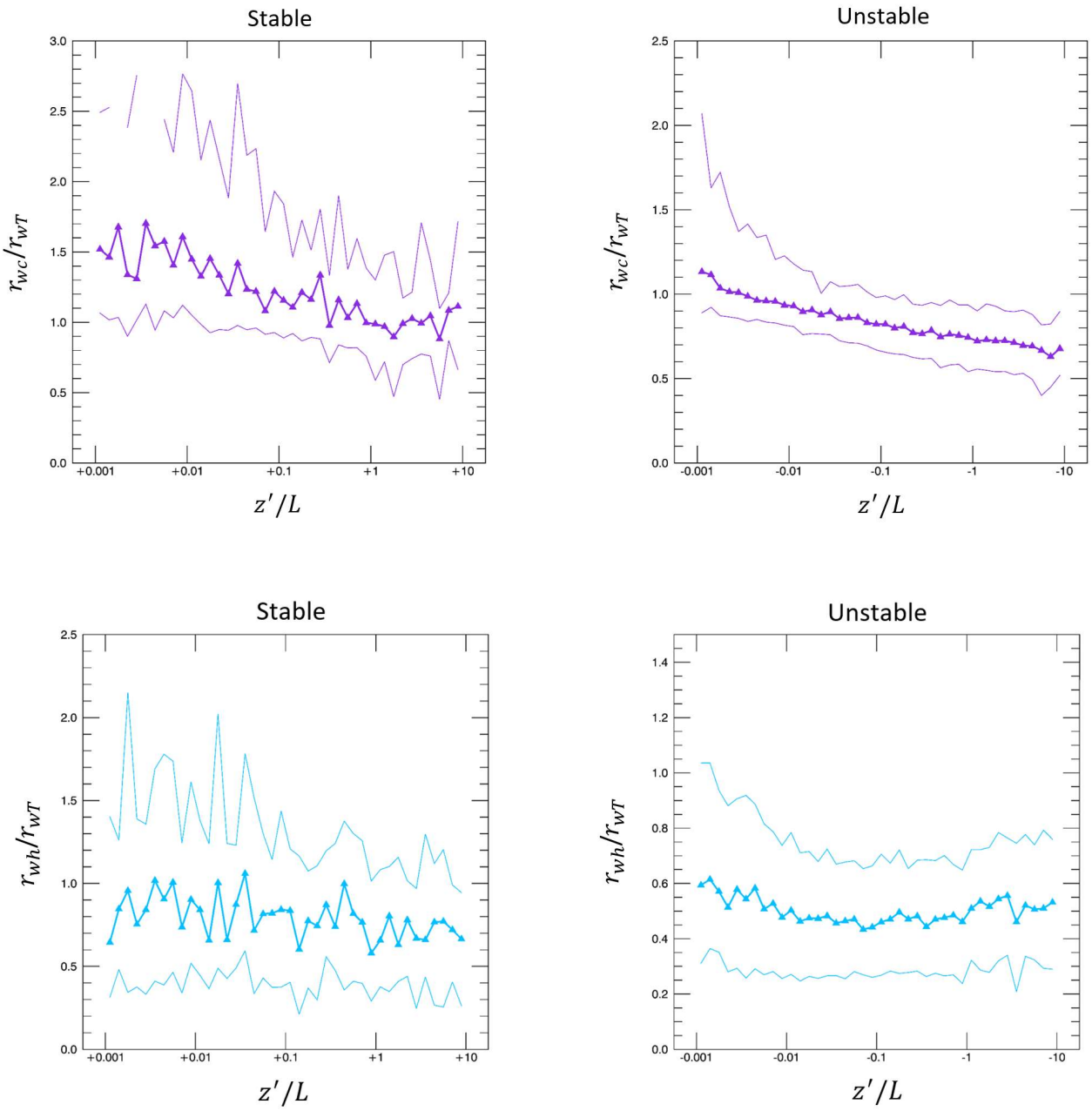

Figure 3.13: The ratios r_{wc}/r_{wT} (top) and r_{wh}/r_{wT} (bottom), for log-transformed stable (left) and unstable (right) conditions. In each case, only the SE (90–180°) wind sector was considered. Only absolute values are plotted (the directional differences in exchange efficiencies are omitted). Median values are presented, and the coloured bands represent the 25th to 75th percentile range.

Under unstable conditions, the ratios of both CO_2 and water vapour are < 1, indicating that sensible heat is being transferred more efficiently than the passive scalars. This has been attributed to the

role of buoyant thermal production, where the active nature of heat maintains highly efficient transport under unstable atmospheres (Li and Bou-Zeid 2011).

As stabilities tend towards neutral, r_{wc}/r_{wT} approaches, and exceeds 1. As stability has been shown to affect the exchange efficiency of sensible heat more than the passive scalars, which exhibit relatively little variation as a function of stability (Figure 3.12), this increase in r_{wc}/r_{wT} can be explained by a decrease in the efficiency of heat transfer, more so than an increase in the efficiency of CO_2 exchange. In the case of r_{wh}/r_{wT}, exchange remains more efficient for sensible heat than for water vapour under stable conditions, but only slightly, as median values are approaching unity. Nordbo et al. (2013) found that sensible heat is transferred less efficiently that CO_2 and water vapour under stable conditions, and Wang et al. (2014) found the opposite to be true, with water vapour being transferred slightly more efficiently than CO_2, and both less efficiently than sensible heat under stable conditions. The results presented here, however, indicate that CO_2 is transferred more efficiently than sensible heat and water vapour, and that water vapour is transferred almost as efficiently as sensible heat for stable conditions. The discrepancies between studies again highlight the effects of source/sink heterogeneity on the differences in exchange efficiencies of the scalars, as each study area and each city is different.

3.2.3 Summary of stability dependencies of turbulent exchange efficiency

1) For the SE wind sector, each of the MOS-predicted values of r_{wT} and r_{uw} from Roth (2000) and Oke et al. (2017) overestimate exchange efficiency for momentum and/or sensible heat at the neutral limit. At greater instabilities, the SL prediction conforms to r_{uw}, while predictions from Roth (2000) and Oke et al. (2017) continue to overestimate the correlation coefficients of momentum and heat. This result may be explained by the fact that Sunset Tower operates in the ISL (Giometto et al., 2017), while many urban EC studies used in the calculation of the semi-empirical constants in Roth (2000) and Oke et al. (2017) operate closer to the ground.

2) Under stable conditions, stability influences the exchange of momentum and scalars more than surface heterogeneity. Under unstable conditions, the correlation coefficients of momentum, sensible heat, water vapour, and CO_2 are more affected by changes in the source area, and this manifests in large dissimilarities in the transport efficiencies.
3) Discrepancies between urban studies on the relative efficiencies of heat, water vapour and CO_2 under the same atmospheric stability regimes indicates that differences in urban morphology and surface energy balances influence turbulent transfer efficiencies of passive scalars to a greater extent than stability.

3.3 Temporal analysis

Atmospheric stability plays an important role for the efficiency of momentum and sensible heat exchange. As outlined in Section 3.1, characteristic stability regimes occur at different times of the day and year. While passive scalars may be greatly influenced by spatial source/sink distributions at the surface, this heterogeneity also presents itself in terms of spatially-bound surface processes, which may exhibit temporal traits. For example, a vegetated area may be a net sink of CO_2 during the day, but a net source during the night, as the processes of photosynthesis and respiration fluctuate diurnally (Jarvi et al., 2012). It follows that analysis of temporal changes in transport efficiencies will reveal information that uniquely stability or spatially-focussed analyses would omit.

3.3.1 Diurnal trends

The diurnal trend of the correlation coefficients for sensible heat, water vapour, momentum, and carbon dioxide (CO_2) were examined for the eight-year study period (May 2008 – May 2016). The results (Figure 3.14) show r_{wT} displays the largest diurnal range of values, with a maximum eight-year mean of 0.34 around noon, a minimum of -0.026 in the early hours of the morning, and an average diurnal magnitude of 0.15 (considering absolute values only). Sensible heat exchange is most efficient at midday,

when solar radiation is able to interact with many surfaces, providing a more uniform distribution of heat at the surface (Arnfield 2003). Further, with strong surface heating, atmospheric stability is most unstable, lending to very efficient heat exchange. During the day, sensible heat flux (Q_H) is positive, while at night it becomes negative, and this is also reflected in the positive daytime r_{wT} and the negative nighttime r_{wT}.

Water vapour exhibits a similar diurnal trend, but r_{wh} is smaller than r_{wT}, and remains mostly positive at night. The maximum r_{wh} value of 0.18 is found just before noon, the minimum value of 0.043 around midnight, and the average diurnal magnitude is 0.10. Momentum exchange is most efficient in the late afternoon, reaching a minimum average value of -0.21. The maximum is -0.11, and the daily average is -0.16. Both r_{wh} and r_{wc} are on average positive during the night, indicating net upward transfer, while r_{wT} is transferred downward (negative values). At night, a weak sink of sources of sensible heat at the surface, and increased occurrence of stable conditions result in a reduction in the absolute value of r_{wT}. Conversely, during the night, soil respiration acts as a source of CO_2, and vegetation acts as a source of both CO_2 and water vapour, resulting in net upward transfer of both scalars.

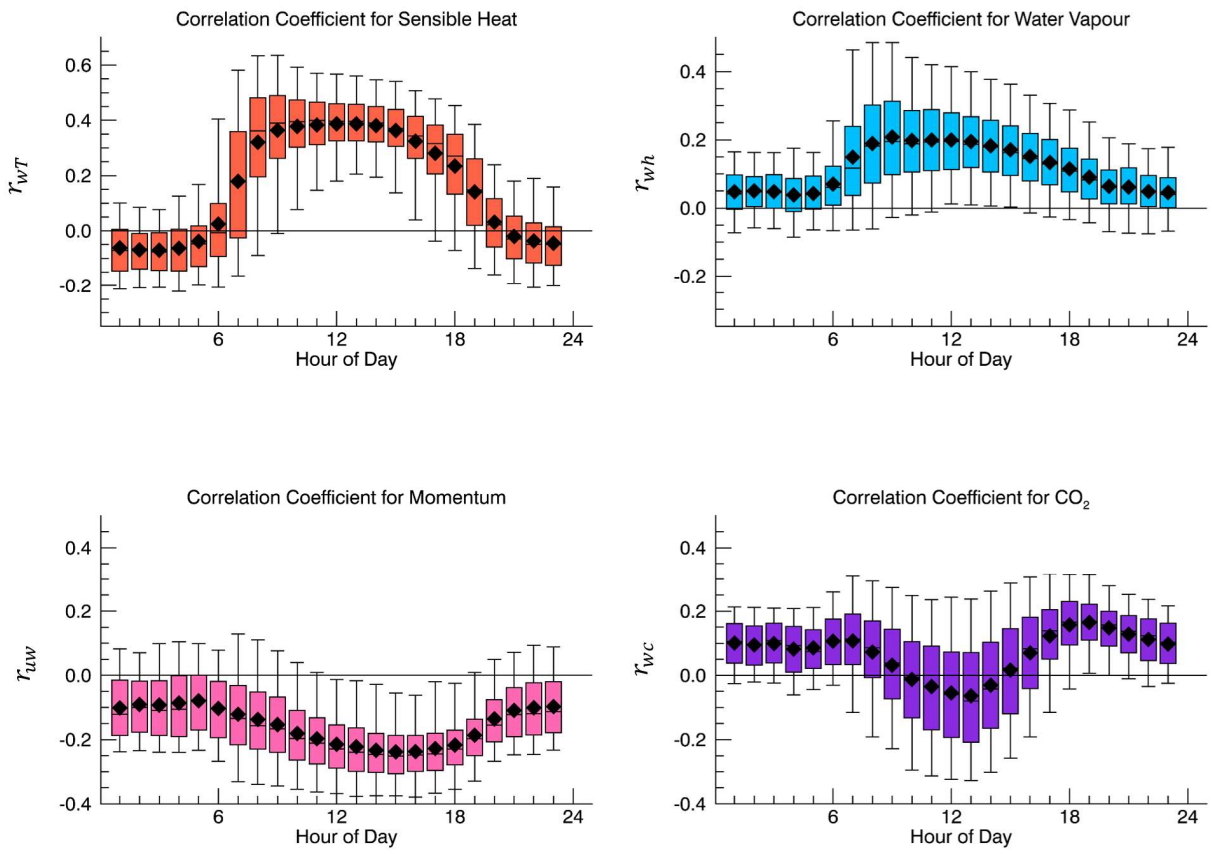

Figure 3.14: Diurnal boxplots of the correlation coefficients for sensible heat, water vapour, momentum, and CO_2 for all stabilities, and the SW wind direction, using eight years of flux data. Note the different y-axis scales.

The maximum for r_{wc} is 0.15, the minimum is 0.048, and the daily average magnitude is 0.11. The midday increase in downward-directed r_{wc} is expected for this area, as vegetation in the source area is photosynthesizing during the day. During the day, CO_2 fluxes from traffic emissions (to the atmosphere) and from photosynthesis (toward the surface) are in opposition, and this is reflected in a r_{wc} value closer to zero. Exchange efficiency of CO_2 peaks at around 8:00 PST and again between 16:00 – 17:00 PST, which corresponds well with morning and evening rush-hour times, when commuters head to and from work. At these times, the increased uniformity of traffic-emitted CO_2 sources leads to an increase in r_{wc}.

To isolate instances of weekday commuter emissions, r_{wc} during weekdays was compared to weekends (Figure 3.15). Both the NE and the SE wind sectors present large increases in the efficiency of CO_2 exchange during the daytime hours, and a decrease in the efficiency of upward CO_2 transport at night. Interestingly, the exact opposite trend is observed in the SW and NW sectors, with r_{wc} being efficiently transported towards the surface around noon, and away from the surface at night.

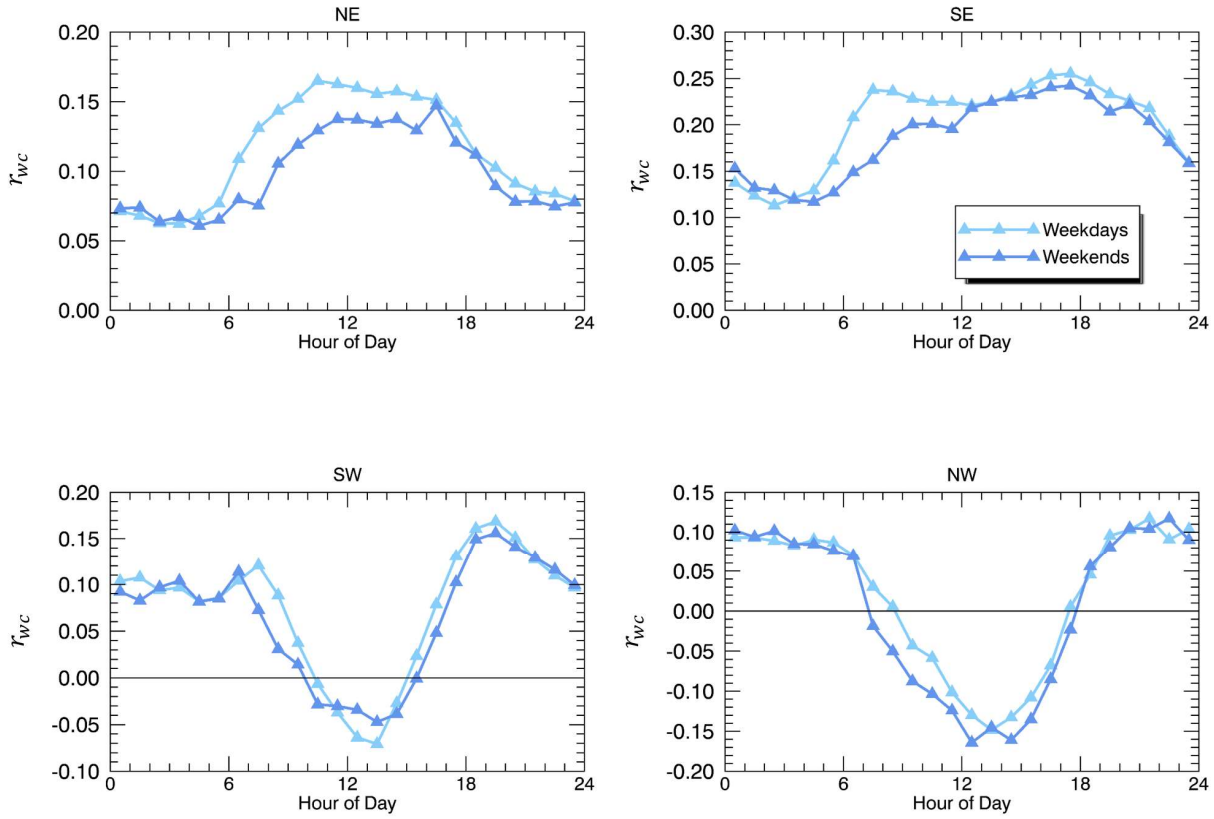

Figure 3.15: Comparison of the diurnal trend in weekday and weekend r_{wc}, for the NE, SE, SW, and NW, for all stabilities.

During the weekends, r_{wc} is on average smaller compared to weekdays. This weekday-weekend difference is most notable in the NE, where the smallest footprint-averaged vegetation fraction and the largest footprint-averaged traffic amount exist (Figure 3.1 in Section 3.1). The enhanced r_{wc} here is, hence, very likely to be the result of daytime traffic densities. While source areas and vegetation do not

fluctuate significantly between the weekdays and weekends, traffic amounts do fluctuate. The increased r_{wc} during the weekdays compared to the weekends is likely due to the increased traffic uniformity in the source area during these days. The highly-vegetated SW and NW, and the high volume of traffic in the NE and SE also explains the conflicting trends in the direction of CO_2 exchange in these areas, as daytime photosynthesis brings CO_2 towards the surface in the NW-SW, and traffic emissions enhance upward CO_2 exchange in the NE-SE. r_{wT}, r_{wh}, and r_{uw} showed no statistically significant differences between weekday and weekend values.

Seasonality in the diurnal trends was explored to observe intra-annual differences in exchange efficiencies over the course of the day (Figure 3.16). Sensible heat shows the highest exchange efficiency at all times of the day during summer, and the lowest during winter. In terms of water vapour exchange, fall shows the greatest variation between nighttime and daytime values, with a peak exchange efficiency of 0.19 at around 10:00 PST. Nighttime values are generally higher during the spring, as vegetation is present at this time of year, and nighttime anthropogenic, soil, and biomass respiration releases water vapour into the atmosphere.

At night, summertime r_{uw} values drop below those of spring, winter, and fall. This may be due to the high occurrence of unstable conditions, even at night, during the summer months, reducing momentum exchange (see Figure 3.8 in Section 3.1). Daytime momentum exchange is more efficient in spring and summer compared to winter and fall. Enhanced roughness during leaves-on seasons contributes to more efficient momentum exchange (see Section 3.4 for analysis of the relationship between roughness length and r_{uw}).

Seasonal variation in nighttime r_{wc} is small. However, daytime values are significantly different between seasons, particularly between summer and winter (t-statistic = 4.03, p = 0.0002). Summer and spring show the largest midday downward exchange efficiencies (average -0.15 for summer, -0.09 for spring at noon), as active vegetation photosynthesizes, efficiently transporting CO_2 towards the surface. In

winter, the opposite trend is observed; a slight increase in the efficiency of upward transport at midday occurs (average of 0.12 at noon). This is likely an aggregated effect of the decrease in photosynthetically active vegetation in winter, and CO_2 emissions from buildings and vehicles within this sector (Christen et al., 2011).

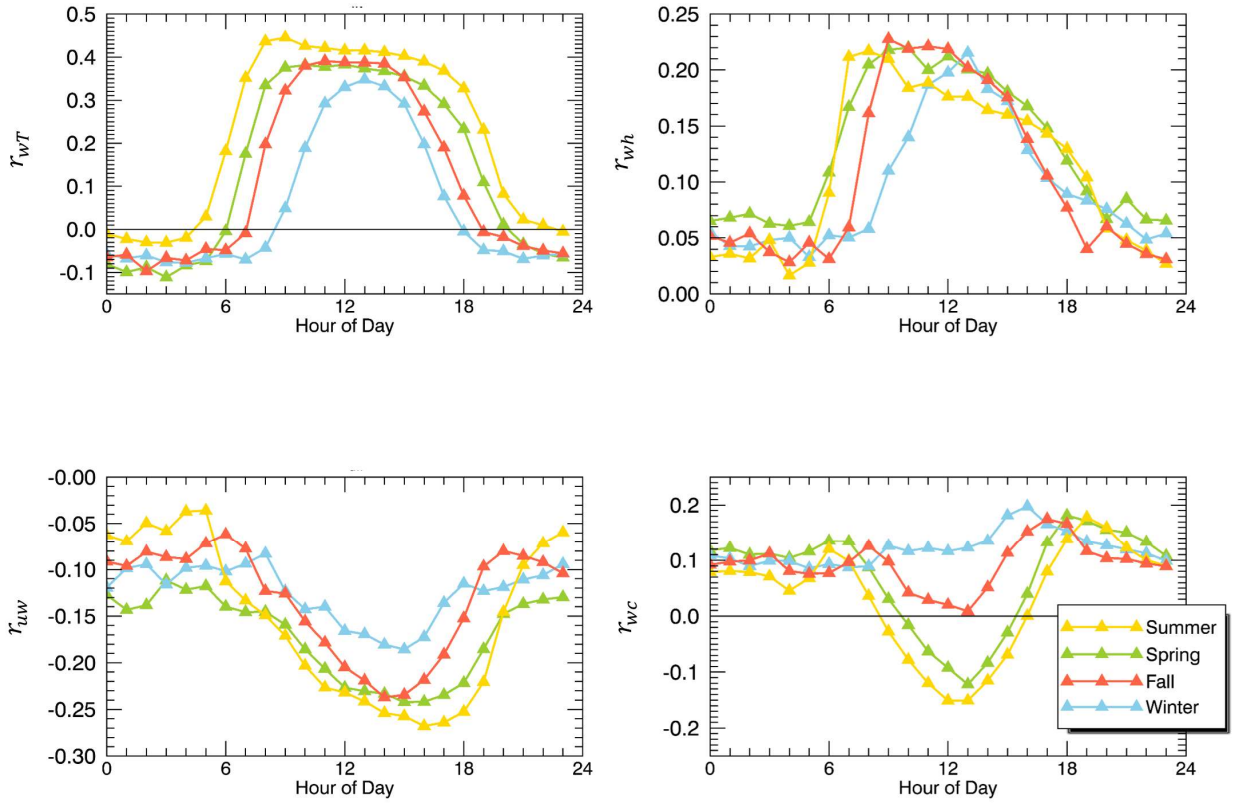

Figure 3.16: Seasonally-stratified diurnal plots of the mean hourly correlation coefficients r_{wT}, r_{wh}, r_{uw}, and r_{wc}, for all stabilities, and the SW wind sector.

3.3.2 Annual trends

Annual trends in the correlation coefficients are plotted in Figure 3.17, and monthly averages are presented in Table 3.3. Overall, sensible heat is exchanged more efficiently than momentum, water vapour, and CO_2 over the course of the year. Increased exchange of sensible heat is observed in summer when the sun is the dominant source of heat, and higher solar elevation and longer days cause more

uniform heating across the 3D urban surface. In winter, days are shorter, and lower solar elevation preferentially heats roofs causing a patchier distribution of sensible heat sources. The annual trend of r_{uw} shows that exchange is most efficient during spring, and least efficient during winter. In spring, leaves are present, increasing the roughness of the surface and facilitating drag, which increases momentum exchange efficiency (see Section 3.4).

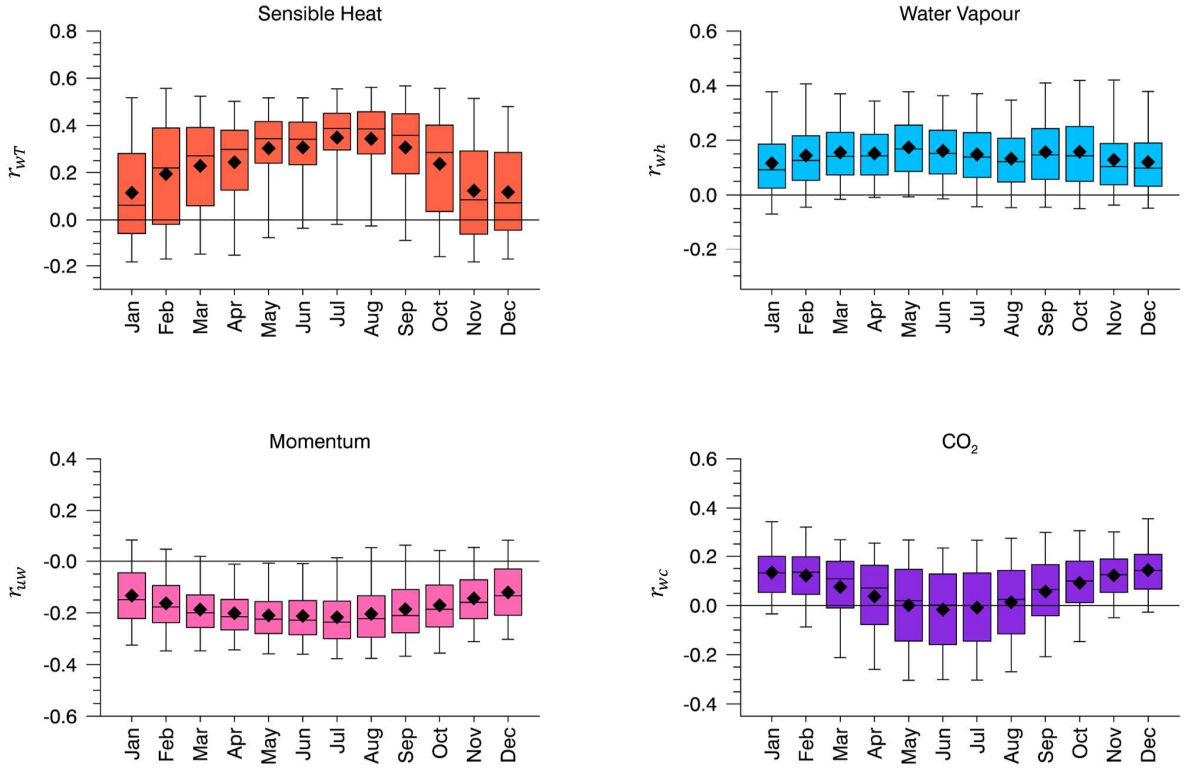

Figure 3.17: Monthly plots of the correlation coefficients r_{wT}, r_{wh}, r_{uw}, and r_{wc} for all stabilities, and the SW wind sector only.

Table 3.3: Monthly average values of the correlation coefficients, r_{wT}, r_{wh}, r_{uw}, and r_{wc} for all stabilities, and all wind directions. Annual averages for each correlation coefficient are also presented.

Month	r_{wT}	r_{wh}	r_{uw}	r_{wc}
January	0.069	0.086	-0.13	0.12
February	0.093	0.098	-0.14	0.12
March	0.11	0.11	-0.16	0.11
April	0.15	0.11	-0.17	0.094
May	0.20	0.13	-0.18	0.096
June	0.22	0.13	-0.19	0.11
July	0.24	0.10	-0.18	0.10
August	0.21	0.091	-0.17	0.11
September	0.16	0.096	-0.14	0.092
October	0.11	0.094	-0.14	0.11
November	0.054	0.093	-0.13	0.12
December	0.048	0.094	-0.14	0.13
Annual Average	0.14	0.10	-0.16	0.11

The average annual r_{wh} for the SW sector is significantly lower than r_{wT} (a t-statistic of -3.66, and a p-value of 0.0014). Exchange of water vapour is most efficient in spring, when sources of water are distributed more uniformly in the urban environment. A reduction in magnitude of the exchange efficiency of water vapour over the course of summer and into winter is observed, with a minimum summertime average in August when sources of water are patchy (see Figure 1.1).

To further investigate the effects of patchy sources of water on r_{wh} a wet and dry summer (June, July, and August) were isolated and compared. Soil volumetric water content was continuously measured in eight representative lawns within the source area, using water content reflectometers operated at a depth of 5 cm (Christen et al., 2013). Figure 3.18 shows that as soil volumetric water content increases, r_{wh} also increases, with mean values ranging from 0.10 to 0.19.

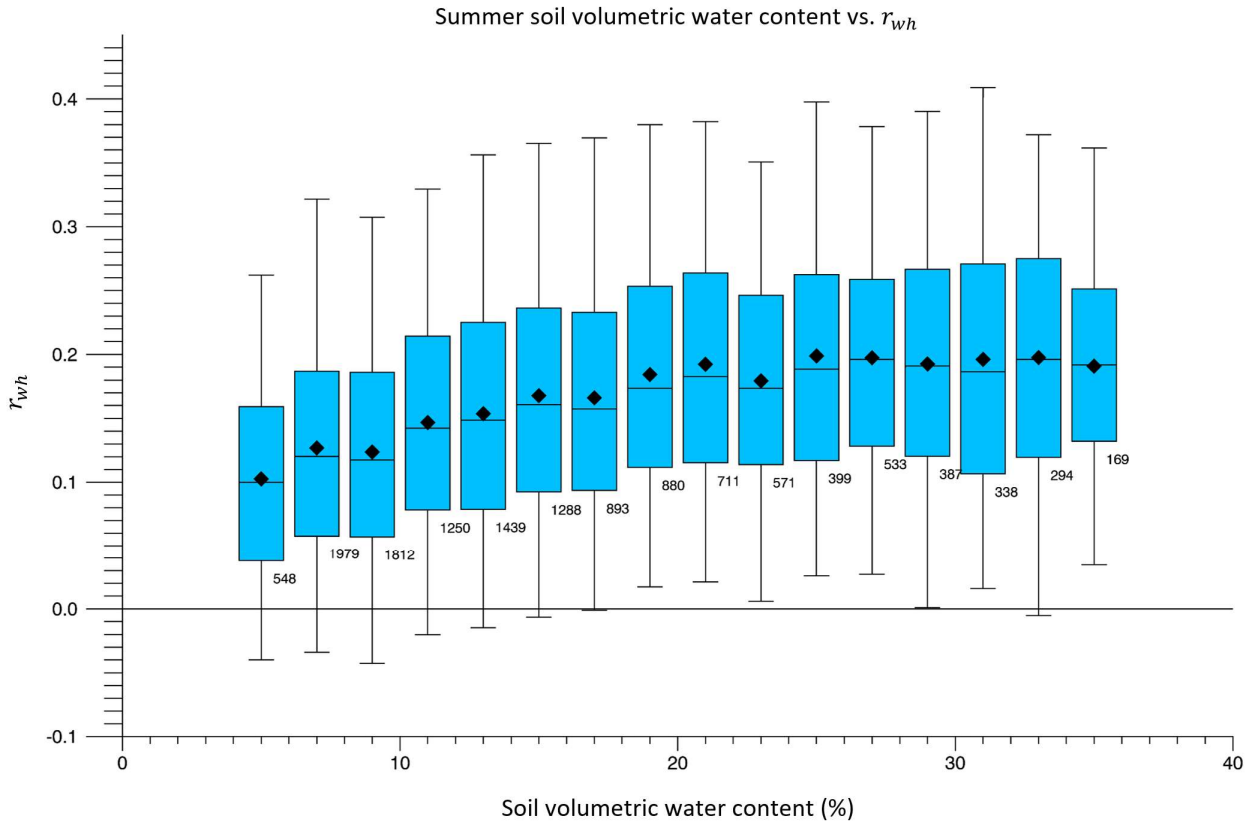

Figure 3.18: Relationship between summer soil volumetric water content measured within the study area, and r_{wh} for unstable, daytime conditions.

Summer 2014 was found to be particularly wet, with an average soil volumetric water content of 23.4%, and 2015 exhibited the lowest average summer soil water content at 11.41% (Figure 3.19). In 2014, monthly average precipitation over June, July, and August totaled 116.30 mm, while monthly average precipitation for the same months in 2015 totaled only 89.90 mm. Bowen ratios for both years were calculated based on average monthly sensible and latent heat flux densities, with a summertime value of 2.29 for 2014, and 3.41 for 2015 which is the highest recorded summer value over the eight years of flux data. In early July of 2015, a Stage 2 water restriction was mandated by the City of Vancouver, which allowed residents to irrigate their lawns only once per week. This restriction was heightened to a Stage 3 water usage restriction on July 20th which banned lawn irrigation entirely, and resulted in a highly

patchy distribution of water at the surface. Restrictions were in effect over the course of summer, and lifted at the end of September 2015. Figure 3.19 shows that in May, both years have similar r_{wh} values, followed by a clear decrease in for the dry 2015 summer (average r_{wh} of 0.16) compared to the wet 2014 summer (average r_{wh} of 0.21) over the subsequent months.

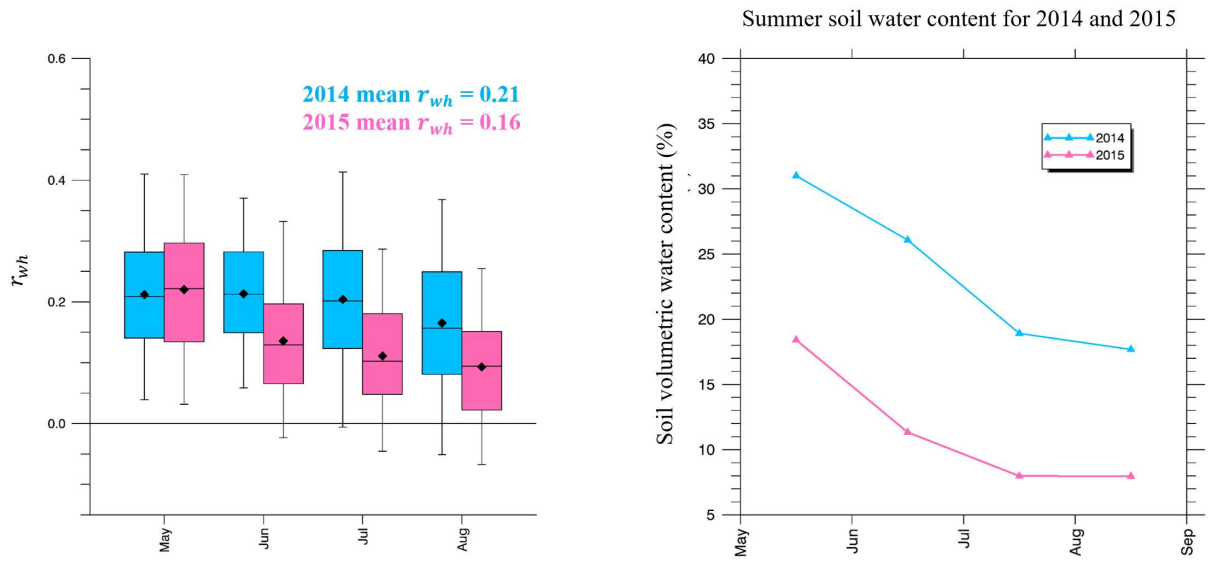

Figure 3.19: The boxplot on the left compares r_{wh} for a wet (2014) and a dry (2015) summer for unstable, daytime conditions, and the SW wind sector. The graph on the right gives the average soil volumetric water content over the course of the summer, for both years.

Non-uniformity in lawn irrigation practices, leading to spatial dissimilarities in soil water content greatly influence summertime exchange efficiency of water vapour. During the wet summer, surface water is more uniform in the source area, resulting in a higher exchange efficiency compared to the highly patchy distribution of water observed during the dry summer.

Exchange efficiency for CO_2 is highest during winter, and approaches zero (no correlation) during early spring and late summer. A slight increase in downward r_{wc} is observed in June. To investigate the high wintertime values, r_{wc} was plotted against heating degree days (HDD) (Figure 3.20). As the days get colder (HDD temperature increases), there is a steady increase in the exchange efficiency

of CO_2. In Vancouver, most homes use natural gas heating systems, which emit CO_2 when combustion occurs, thus as temperatures drop and people begin heating their homes, fluxes of CO_2 increase and sources of CO_2 become more uniform in the source area, leading to an increase in r_{wc} (Christen et al., 2011).

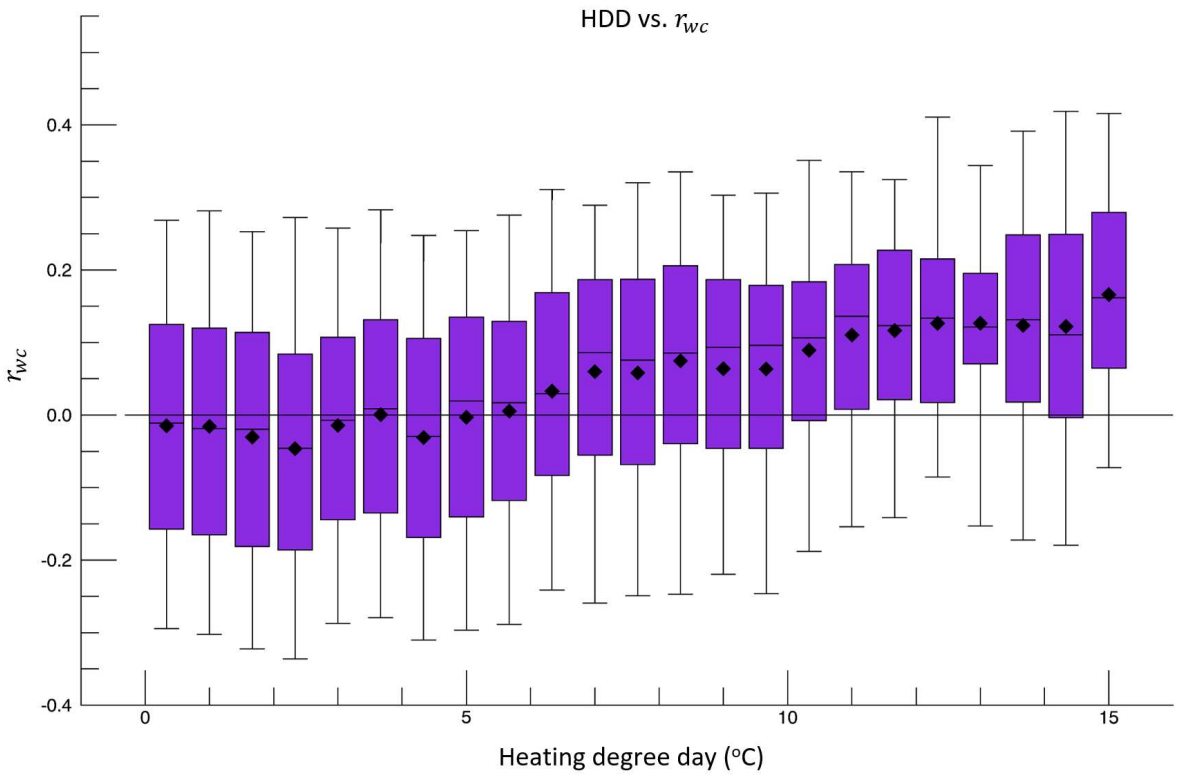

Figure 3.20: Exchange efficiency of CO_2 as a function of heating degree days (HDD), for unstable, daytime conditions, and the SW wind sector only.

3.3.3 Summary of temporal effects on turbulent exchange efficiency

1) Exchange efficiencies exhibit clear diurnal and seasonal trends in magnitude and direction (upward transfer, downward transfer). Sensible heat is more efficiently transferred compared to the other turbulent entities, and displays the largest diurnal and seasonal variation in exchange.

2) As sources of water become patchier, the exchange efficiency of water vapour decreases. For example, exchange efficiency of water vapour is lower throughout summer compared to other seasons (in dryer summer months, yard irrigation causes a patchier distribution of water which lowers r_{wh}). This is also seen in a clear positive relationship between soil volumetric water content (less than 20%) and r_{wh}.
3) Momentum exchange is more efficient during summer, when leaves are out, as a result of increased drag by vegetation, which was similarly found to be the case by Giometto et al. (2017) for the same site.
4) Upward exchange efficiency for CO_2 increases at peak traffic rush-hour times over the day, at night when biomass is respiring, and over the colder winter months when building heating is in use. CO_2 is efficiently transferred towards the surface during the daytime, especially in warm spring and summer months when vegetation is more active.

3.4 Geospatial analysis

Urban areas exhibit spatial heterogeneity at multiple scales which can affect flux measurements. For example, when the scale of surface patchiness is much smaller than the source area, it is expected that exchange efficiencies will be high, and fluxes will accurately represent the landscape. When the scale of surface patchiness is equal to or approaches the extent of the source area, exchange efficiencies will be small, and the representativeness of fluxes will be in doubt. Finally, if the scale of surface patchiness far exceeds the bounds of the turbulent source area, exchange efficiencies might be larger, but fluxes may not be accurately describing the landscape under investigation, which is the case particularly under unstable conditions (Roth 2000, Crawford and Christen 2015). At these scales, sources and sinks of momentum and scalars that are not co-located result in dissimilar transfer efficiencies (Roth and Oke 1995). Sections 3.2 and 3.3 have highlighted the centrality of analysis on surface source/sink heterogeneity; Using a combination of detailed surface cover data and flux footprints, derived footprint-averaged surface cover

fractions allow for a comprehensive investigation into the relationship between discrete surface properties and the correlation coefficients of momentum and scalars.

3.4.1 Wind direction

As a first step in investigating whether there exist significant spatial differences in exchange efficiencies, given the temporally and spatially variable surface processes and characteristics, r_{wT}, r_{wh}, r_{uw}, and r_{wc} were plotted against wind direction (Figure 3.21).

Sensible heat exchange is more efficient during day (average r_{wT} = 0.25), and in the SW sector (average r_{wT} = 0.34). The increased daytime transfer efficiency from the SW is mostly attributable to the daytime sea breeze from this direction, which is especially strong during summer. Strong winds from the SW will, therefore, become warmer as they pass over the warm urban surface, effectively transferring heat to the atmosphere. At night, r_{wT} values are closer to zero, indicating very inefficient transfer occurring at this time of day. Average nighttime r_{wT} (value of 0.038 considering all wind directions) becomes slightly negative in the NE wind sector (average nighttime r_{wT} = -0.030), but remains slightly positive in all other wind sectors. The NE is the direction from which frequent nighttime winds originate, possibly developing from cold air drainage flows, especially in winter; These frequent NE winds transfer heat energy to the cold surface (negative r_{wT} values).

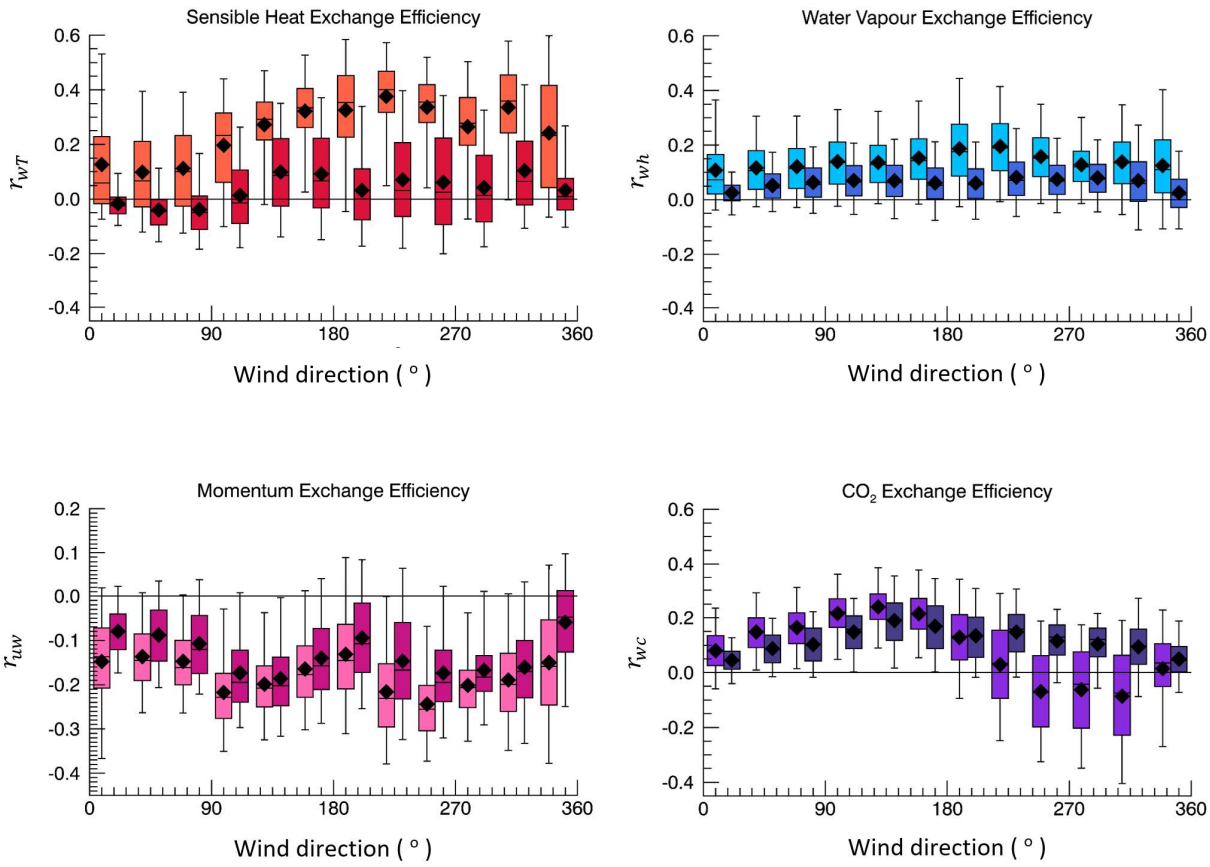

Figure 3.21: Exchange efficiencies for sensible heat (top left), water vapour (top right), momentum (bottom left), and CO_2 (bottom right) as a function of wind direction, for all stabilities. The orange, light blue, pink, and violet boxplots show the daytime r_{wT}, r_{wh}, r_{uw}, and r_{wc} values, respectively, and the darker boxes show the nighttime values.

Comparatively, water vapour exchange is less efficient than sensible heat during the day (average daytime r_{wh} = 0.14), for all wind directions. Slight daytime peaks exist in the SW and NW, which correspond with wind sectors containing the highest vegetation fractions (see Figure 3.1 in Section 3.1) resulting in enhanced daytime evapotranspiration of water vapour into the atmosphere. Unlike r_{wT}, average r_{wh} remains positive throughout the night, and varies little about a mean of 0.061. At night, moisture can originate from surface water evaporation and anthropogenic emissions, resulting in a net upward transfer of water vapour. The nighttime trend in r_{wh} follows the daytime trend closely, but

nighttime r_{wh} is not as efficient, as the buoyant thermals that transfer water vapour toward the atmosphere during day are not present at night.

To investigate how the efficiency of transfer of sensible heat and water vapour compare as sources of moisture at the surface are varied, r_{wT} and r_{wh} were plotted against soil water content (Figure 3.22).

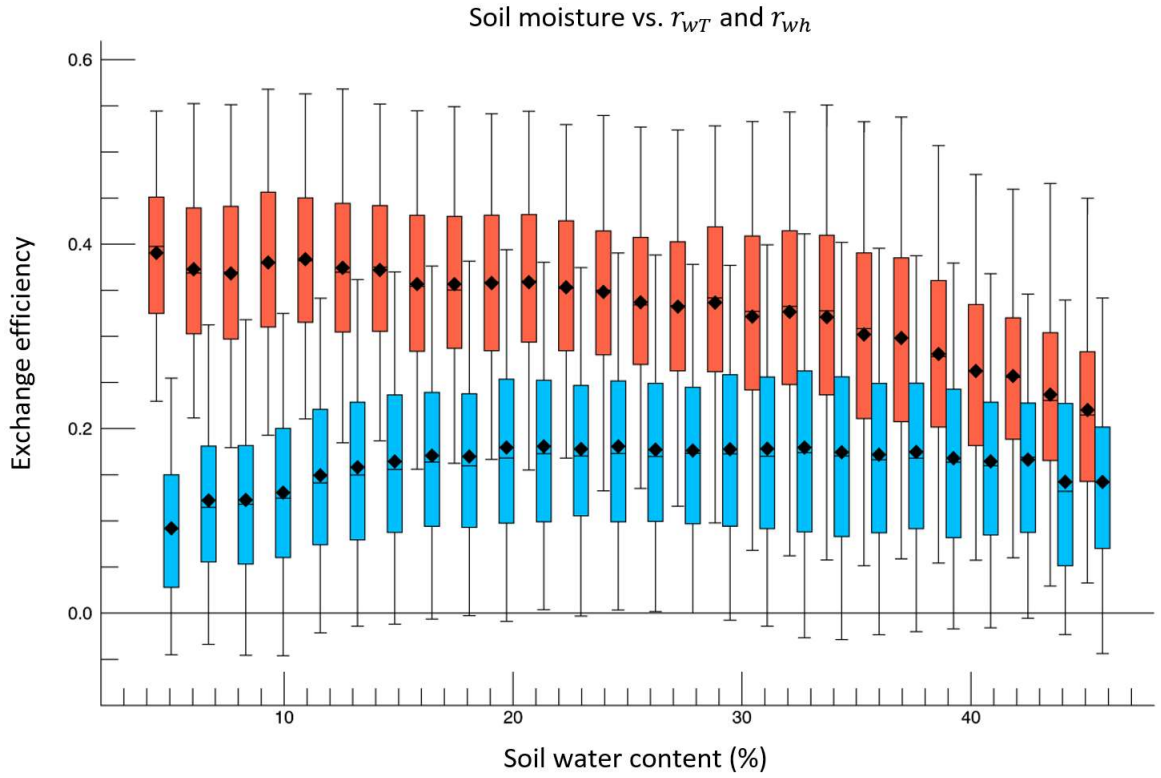

Figure 3.22: The exchange efficiencies of sensible heat (orange boxes) and water vapour (light blue boxes) as a function of soil moisture, for unstable, daytime conditions.

The results show a slight initial increase in r_{wh} under dry conditions, but then r_{wh} remains fairly constant. r_{wT}, however, consistently decreases as soil moisture increases. The observed de-correlation between r_{wT} and r_{wh} under dry soil conditions suggests that MOS may hold true under very wet conditions (> 40% soil water content), but breaks down for dry conditions (< 20%). Detto et al. (2008)

likewise found a decorrelation between r_{wT} and r_{wh} as soils become dryer. This decorrelation has been similarly analyzed in terms of the Bowen ratio, and has been linked to entrainment processes, where warm, dry air aloft is brought toward the surface. For analyses that examine the possible contribution of entrainment on dissimilarities between r_{wT} and r_{wh}, see Appendix A.

Momentum exchange efficiency shows similar trends during day and night, with enhanced efficiency in the east and west, and lowest efficiency in the north and south. In the NE, there exists an empty gravel lot which reduces friction, resulting in a smaller momentum flux, and therefore a smaller r_{uw}. Increased r_{uw} in the west corresponds well with the direction from which larger vegetation fractions are present, and increased r_{uw} in the east corresponds with taller buildings in this direction (Figure 3.23).

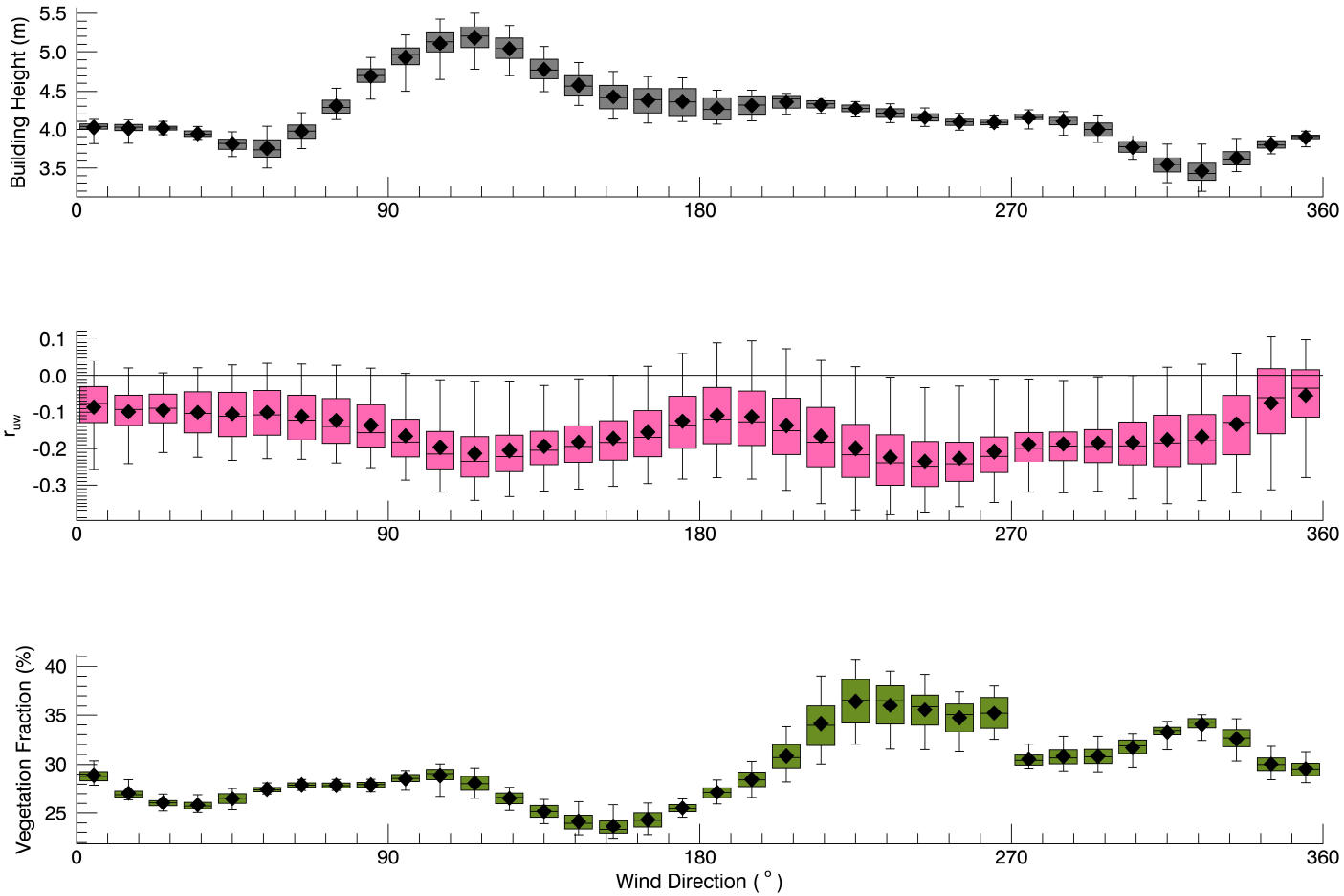

Figure 3.23: The footprint-averaged building height (top), r_{uw} (middle), and footprint-averaged vegetation fraction (bottom) as a function of wind direction, and considering all stabilities.

To further discern the effects of vegetation on the downward exchange of momentum, the roughness length (z_0), stratified by leaves-on (May to September) and leaves-off (November to March) seasons, was plotted against wind direction (Figure 3.24). Seasonal changes in r_{uw} were subsequently investigated. The results indicate that the enhanced surface roughness present during the leaves-on season is well correlated with increased r_{uw}.

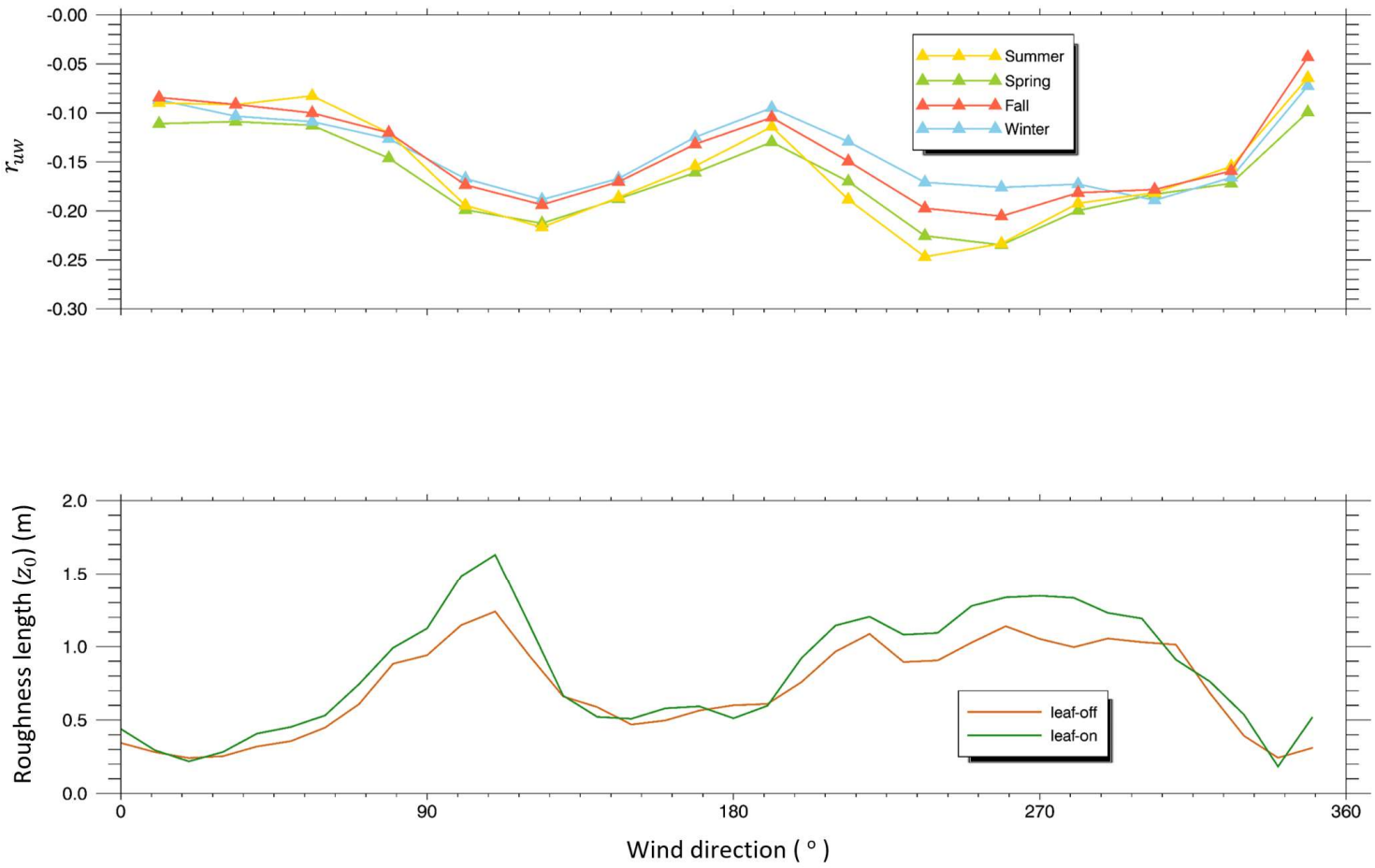

Figure 3.24: Seasonally-stratified r_{uw} as a function of wind direction (top), and the aerodynamic roughness length, stratified by leaves on/off seasons versus wind direction (bottom) for all stabilities.

The leaves-on season tends to result in rougher surfaces than the leaves-off season, as vegetation creates drag (Grimmond et al., 1998, Kent et al., 2017). Momentum exchange is most efficient from the wind directions with larger z_0, and during spring and summer (average spring and summer r_{uw} value of -0.18) relative to fall and winter (average fall and winter value of -0.15). The higher roughness lengths also correspond with the wind directions from which taller buildings occur in the footprint (see Figure 3.23 above).

The efficiency of CO_2 exchange exhibits a dramatic trend in daytime and nighttime values with wind direction. In the NE-SE, mean day and night values are consistently positive, with exchange being most efficient in the SE. In the SW to NW, however, daytime values become negative as CO_2 moves towards the surface, and nighttime values remain positive.

Figure 3.25 compares the footprint-averaged traffic count, the footprint-averaged vegetation fraction, and the day and nighttime r_{wc}, as a function of wind direction. The NE-SE contains the highest traffic amounts, while the SW-NW contains the highest vegetation fractions, and the discrepancy between the two is apparent in the daytime and nighttime r_{wc}. While daytime CO_2 is efficiently transferred away from the surface in the eastern sectors and towards the surface in the western sectors, the smaller nighttime r_{wc} remains consistently positive (net upward transfer). When r_{wc} is not isolated into day and night values, an exchange efficiency of close to zero represents the SW-NW sectors, indicating that competing diurnal sources and sinks are reflected in a lower correlation coefficient (see Figure 3.25, bottom plot).

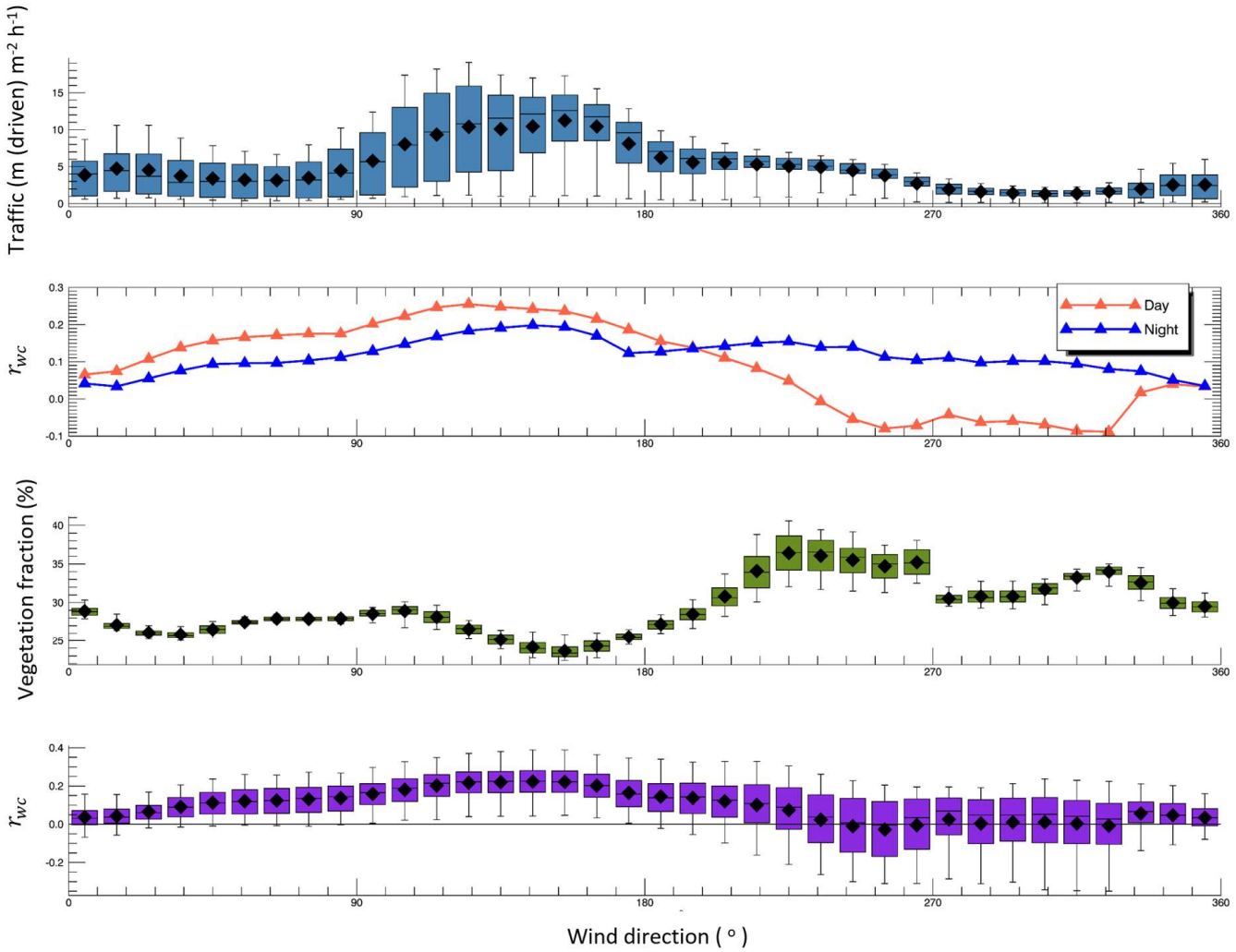

Figure 3.25: (In descending order): The footprint-averaged traffic count (top), r_{wc} broken into day and night, the footprint-averaged vegetation fraction, and r_{wc} (not isolated into day and night) (bottom), as a function of wind direction.

During the day, vegetation photosynthesizes, resulting in an efficient net downward transfer of CO_2 in the wind sectors where larger vegetation fractions exist. At night, soil, vegetation, and human respiration results in an upward transfer of CO_2 (Christen et al., 2010). Conversely, daytime and nighttime traffic loads are consistent sources of CO_2, hence upward transfer of CO_2 is observed at all times of the day in wind sectors containing higher traffic amounts.

3.4.2 Ratios of correlation coefficients

To analyze the effects of source/sink heterogeneity on the dissimilar exchange efficiencies of CO_2, water vapour, and sensible heat, the correlation coefficients (r_{wh}/r_{wT} and r_{wc}/r_{wT}) were broken into daytime and nighttime conditions, and plotted against wind direction (Figure 3.26). Both day and night values for r_{wh}/r_{wT} are < 1, meaning sensible heat is transferred more efficiently than water vapour at day and night, and under unstable and stable conditions. This result is in keeping with the results presented in Section 3.2. The NE sector shows an increase in daytime r_{wh}/r_{wT}, however, this is attributable more to a reduction in r_{wT} in this wind sector, as Figure 3.21 shows.

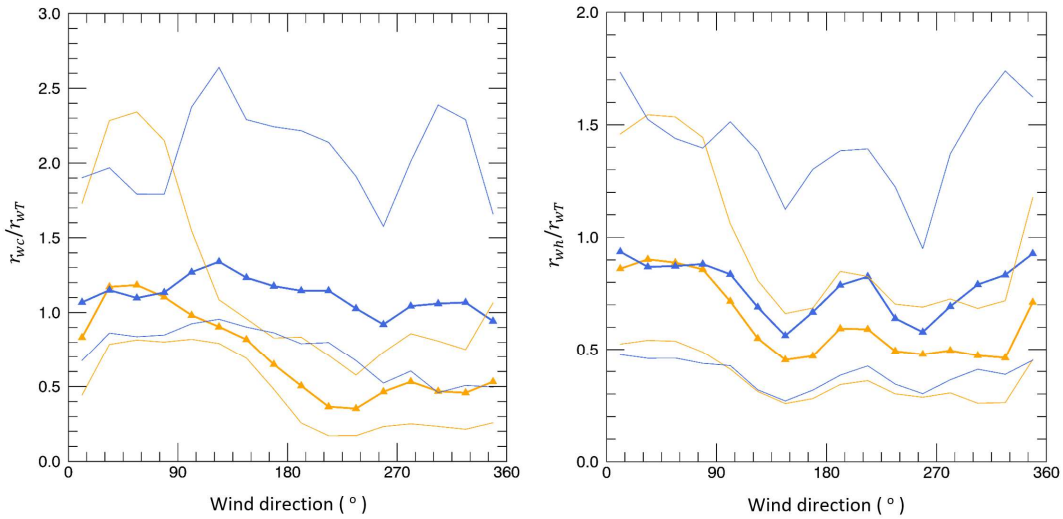

Figure 3.26: The ratio of the correlation coefficients r_{wc}/r_{wT} (left) and r_{wh}/r_{wT} (right) as a function of wind direction, broken into daytime (orange) and nighttime (dark blue) conditions. Only absolute values are plotted. Median values are presented and the coloured bands represent the 25th and 75th percentiles.

For the case of CO_2, daytime values of the ratio r_{wc}/r_{wT} are < 1 in every wind sector except the NE, signifying that sensible heat in each wind sector is, on average, being exchanged more efficiently than CO_2, except in the NE. This is expected, as previous analyse have shown that r_{wT} is heavily dependent on stability, and this dependency has a larger influence on the ratio r_{wc}/r_{wT} than stability-driven changes in r_{wc} (Section 3.2). Daytime r_{wc}/r_{wT} values close to 1 in the NE indicate nearly equal efficiency in exchange in r_{wc} and r_{wT}. For the nighttime case, r_{wc}/r_{wT} exhibits less variation as a function of wind direction, with values hovering around 1 (r_{wc} and r_{wT} are exchanged approximately equally). Nighttime values increase toward 1.5 in the SE, indicating that CO_2 is being exchanged more efficiently than sensible heat. The NE is where largest footprint-averaged traffic counts are found which acts as a large CO_2 source. A slight peak in r_{wc}/r_{wT} in the NW is observed, where large footprint-averaged vegetation fractions are found, enhancing CO_2 fluxes via respiration, again indicating that CO_2 in this wind sector is being exchanged more efficiently than heat. Thus, the increase in r_{wc}/r_{wT} in these regions is greatly dependent on the nighttime traffic and sources of respiration.

The increase in the ratio r_{wc}/r_{wT} in the NE during the day, and the peaks in nighttime values in the SE and NW show that stability alone is not responsible for the relative efficiency of scalar transport; The uniformity of sources and sinks of CO_2 at the surface contribute greatly to the efficiency with which CO_2 is transported in the atmosphere.

A more focussed analysis was performed with r_{wh}/r_{wT} to determine the effects of uniformity in sources and sinks of water vapour on the relative exchange efficiency. Figure 3.27 presents r_{wh}/r_{wT} as both a function of soil moisture, and of the footprint-averaged impervious ground fraction, for unstable, daytime conditions.

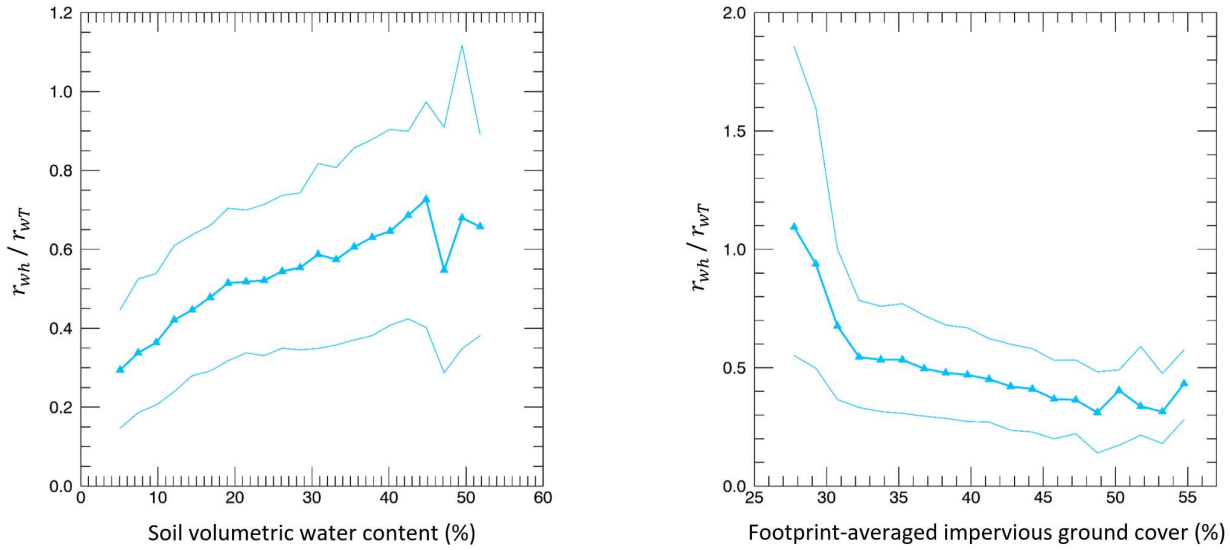

Figure 3.27: r_{wh}/r_{wT} plotted against soil volumetric water content (left) and impervious ground fraction (right), for unstable, daytime conditions. Median values are given and the coloured bands represent the 25th and 75th percentile ranges.

At low soil moisture states, r_{wh}/r_{wT} << 1, as r_{wT} is very efficiently transferred, while the unavailability of water vapour at the surface greatly reduces r_{wh}. Conversely, at high soil moisture states, the uniform distribution of water at the surface increases r_{wh}, and r_{wh}/r_{wT} approaches a value of one.

Analogously, as the footprint averaged impervious ground fraction increases, r_{wh}/r_{wT} decreases from values equal to or greater than one, to values much less than one. At high impervious ground fractions, sources of heat can be uniform during the day, while sources of water vapour are subject to spatial and temporal patchiness.

Roth and Oke (1995) link poor correlation of sensible heat and water vapour to surface heterogeneity of sources and sinks of water and heat, which is particularly likely to occur in urban environments. The availability of water sources at the surface determine the thermal characteristics of urban areas, since wet areas tend to be cool, and dry areas tend to be warm (Schmid and Oke 1992). As

Figure 3.27 shows, as sources of water at the surface become more homogeneous, the exchange of water vapour increases, and that of sensible heat decreases, resulting in a r_{wh}/r_{wT} value closer to unity.

3.4.3 Summary of spatial effects on turbulent exchange efficiency

1) As the uniformity of sources or sinks in the footprint increases, the exchange efficiencies correspondingly increase. De-correlation between heat and water vapour exchange efficiencies is due to heterogeneity in sources of water at the surface, and potentially non-local entrainment effects, especially during dry soil states. Momentum is most efficiently exchanged over areas of high roughness lengths, and during leaf-on seasons when vegetation enhances drag.
2) Spatially and temporally competing sources and sinks of CO_2 (like photosynthesis and traffic emissions) are reflected in an exchange efficiency value closer to zero.
3) Surface heterogeneity in sources and sinks influences the transfer efficiency of CO_2 and water vapour more than stability effects alone, which play a bigger role in determining efficiency of sensible heat and momentum exchange.
4) Homogeneous distributions of water at the surface (like high soil water content) is reflected in a higher ratio of r_{wh}/r_{wT}, while a patchy distribution of water at the surface leads to a smaller value of r_{wh} relative to r_{wT}, and therefore a lower r_{wh}/r_{wT} ratio.

3.5 Quadrant analysis

Coherent structures play an important role in turbulent fluxes of momentum and scalars, particularly over rough surfaces like cities (Roth and Oke 1995, Feigenwinter and Vogt 2005, Christen et al., 2007). Consideration of the effects of stability and source/sink heterogeneity on the relative contribution of ejections and sweeps, and their associated time fractions may provide insight into the established dissimilarities between momentum and scalars.

3.5.1 Stability

As a first step, the fraction of sweeps minus the fraction of ejections (ΔS_0) as well as the time fraction above which half of the flux occurs (T') were analyzed as a function of stability (Figure 3.28). Under unstable conditions, sensible heat, water vapour, and momentum exchange is primarily driven by ejections (negative ΔS_0) (Figure 3.28, top). This result is in keeping with many other studies on turbulent motion over urban areas, and is generally explained in terms of buoyant production under unstable conditions (Rotach 1993, Feigenwinter et al., 1999, Moriwaki and Kanda 2006, Christen et al., 2007, Li and Bou-Zeid 2011, and Wang et al., 2014). Sensible heat and momentum exhibit very similar trends in ΔS_0 as a function of instability, with a mean value of -0.26 for sensible heat, and -0.28 for momentum. In the case of water vapour, the difference between the fraction of sweeps minus ejections is smaller than for sensible heat and momentum, with an average value of -0.15. The relatively less negative ΔS_0 for water vapour compared to sensible heat has been proposed to result from entrainment of dry air from above, particularly when sources of water vapour at the surface are limited (Mahrt 1991, DeBruin et al., 1999, Moriwaki and Kanda, 2006). For further analysis of entrainment, see Appendix A. The mean ΔS_0 value for CO_2 is -0.049, but large variation occurs as a function of instability, with CO_2 exhibiting tendencies towards both sweeps and ejections (positive and negative ΔS_0 values). For CO_2, ejections contribute more at near-neutral conditions, and very unstable conditions. At intermediate instabilities (around z'/L = -0.1), sweeps become the dominating motion (positive ΔS_0).

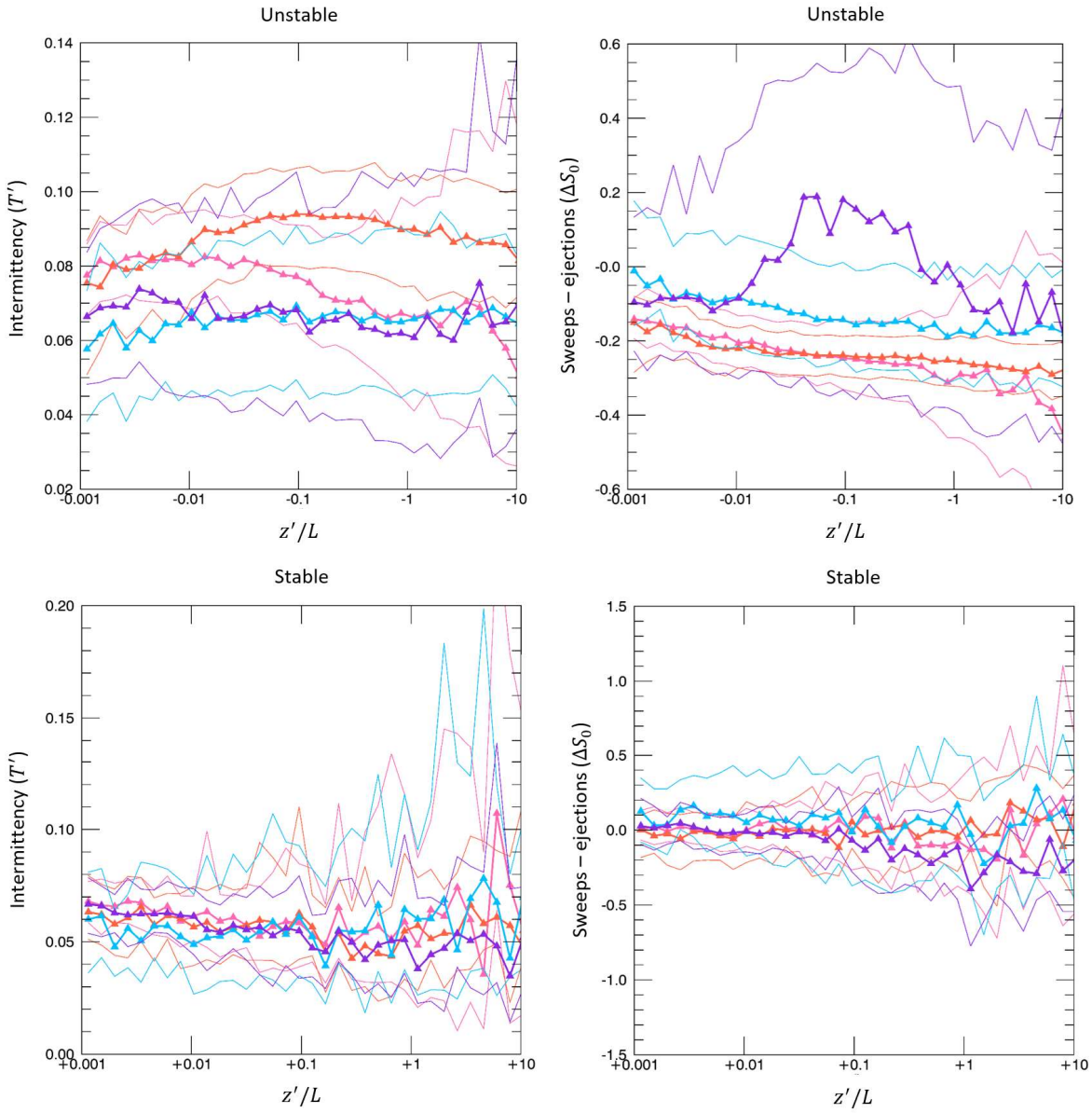

Figure 3.28: Intermittency (T') (left) and the fraction of sweeps – ejections (ΔS_0) (right) for sensible heat (orange), water vapour (light blue), momentum (pink), and CO_2 (violet) as a function of stability, for unstable conditions (top) and stable conditions (bottom), and the SW wind sector only. Plotted data represents median values, and the coloured bands show the 25th and 75th percentiles.

Under stable conditions ($0.001 < z'/L < 10$), flux contributions of ejections and sweeps are nearly equal, although greater variation arises for the very stable ($z'/L > 1$) case (Figure 3.28, bottom). This result was similarly found by Wang et al. (2014) for measurements made above the RSL. Unlike sensible

heat, momentum, and CO_2, water vapour exchange tends to exhibit more positive ΔS_0 values under stable conditions, indicating that sweeps have a greater effect on water vapour exchange than the other turbulent entities.

While sensible heat, water vapour, momentum, and CO_2 all fall below the value of Gaussian turbulence (0.1) under unstable conditions, and are therefore considered to have more intermittent exchange (Christen et al., 2007), sensible heat shows the least intermittency, with T' values reaching a maximum of (0.094) at an instability of about z'/L = -0.1. The T' of momentum exchange follows that of sensible heat for $0 > z'/L >$ -0.01, and then becomes increasingly more intermittent with instability. This means that under very unstable conditions, structures responsible for momentum exchange are rare, but contribute to most of the flux. Water vapour and CO_2 exchange lower T' values than sensible heat and momentum exchange, but change little as a function of instability. Like momentum, the intermittency of water vapour and CO_2 exchange is related to infrequent events that contribute greatly to the flux.

For the stable case, exchange is slightly more intermittent than under unstable conditions, and varies less as a function of stability for each turbulent entity. For $z'/L < 1$, T' values are similar for momentum and scalars, but at very stable conditions ($z'/L > 1$), dissimilarities in T' begin to appear, with no discernable trend, which may be partly an effect of noise in the data, since occurrences of very stable atmospheric conditions are rare.

Taken together, the intermittency with which water vapour and CO_2 ejections and sweeps occur does not vary much with increasing instability, despite the motion of exchange (sweeps or ejections) varying greatly for CO_2 with increasing instability. Conversely, increasingly continuous turbulent structures contribute to the ejecting motion of sensible heat when conditions become more unstable. While momentum and sensible heat show very similar trends in ΔS_0 as a function of stability, increasingly more continuous exchange is observed for sensible heat, and increasingly less continuous exchange is observed for momentum as stability becomes more unstable. This is expected, as under unstable conditions, buoyant production enhances heat flux. Notably, ejections and sweeps both exhibit

low T' values (below 0.1) under unstable conditions, and become more intermittent under a stable atmosphere.

3.5.2 Transfer efficiency

To investigate the relationship between the dissimilarity in the motion and intermittency of the turbulent structures responsible for the exchange of momentum and scalars, and the dissimilarity in transport efficiencies, correlation coefficients (r_{wT}, r_{wh}, r_{uw}, and r_{wc}) were plotted against ΔS_0, and T' (Figures 3.29, 3.30, and 3.31 below).

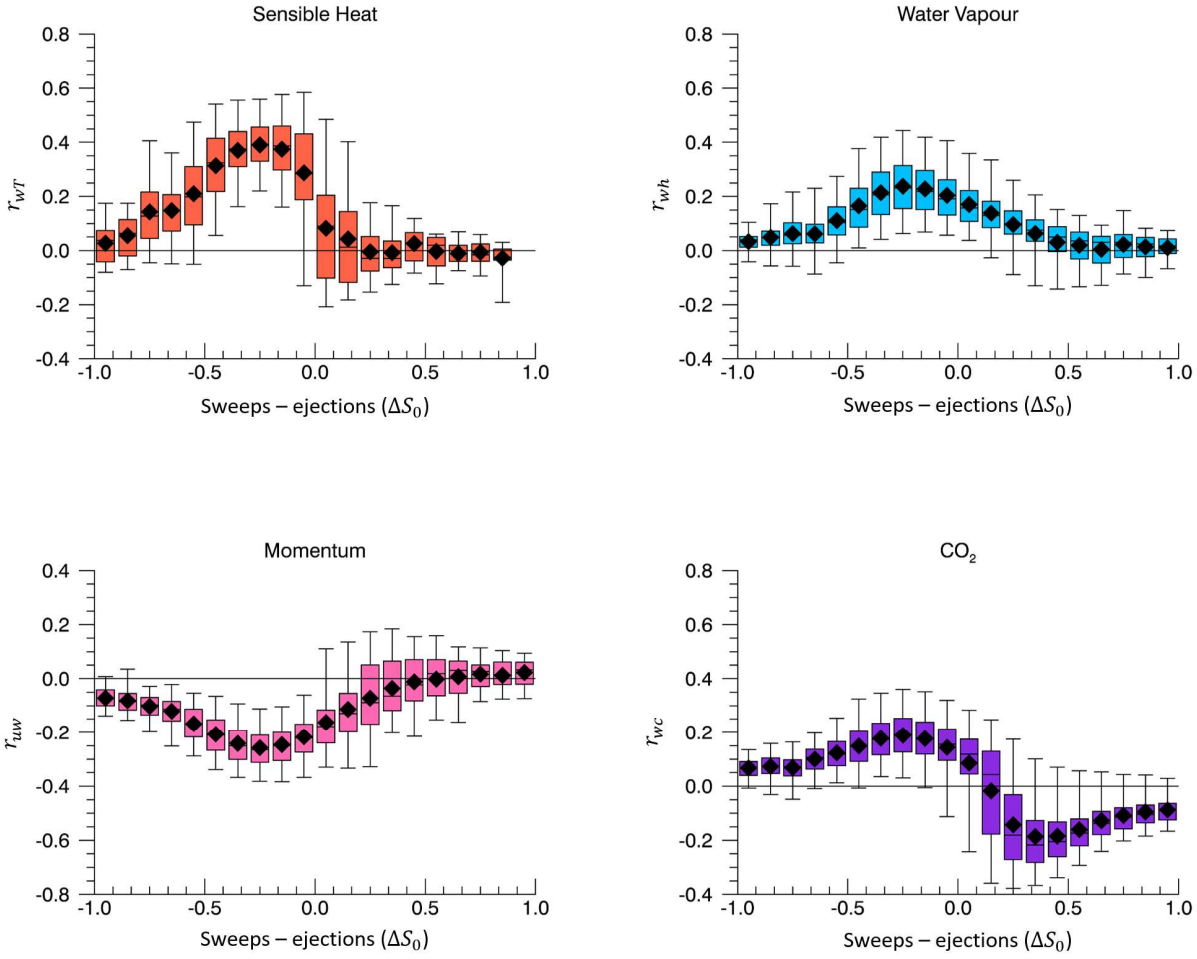

Figure 3.29: Relationship between the exchange efficiencies (r_{wT}, r_{wh}, r_{uw}, and r_{wc}) and the fraction of sweeps – ejections (ΔS_0), during the day and for the SW wind sector.

Figure 3.29 shows that sensible heat is more efficiently transferred by ejections than by sweeps for daytime conditions. This result was also found by Moriwaki and Kanda (2006), who attributed this to buoyant thermal production. Ejections are similarly responsible for the most efficient exchange of water vapour and momentum, which, in the case of momentum, is well documented above the urban canopy layer (Christen et al., 2007). Sweeps correspond with much smaller r_{wT}, r_{wh}, and r_{uw} values.

In the case of CO_2, ejections contribute nearly as equally to upward, efficient exchange, as sweeps contribute to downward, efficient exchange. This suggests that the structures responsible for efficient downward CO_2 exchange and the ones responsible for efficient upward CO_2 exchange are associated with distinct coherent sweeping and ejecting motions. When $\Delta S_0 = 0$, r_{wc} is very small, indicating very inefficient exchange. In each case, at lowest and highest ΔS_0 values, exchange efficiency begins to approach zero.

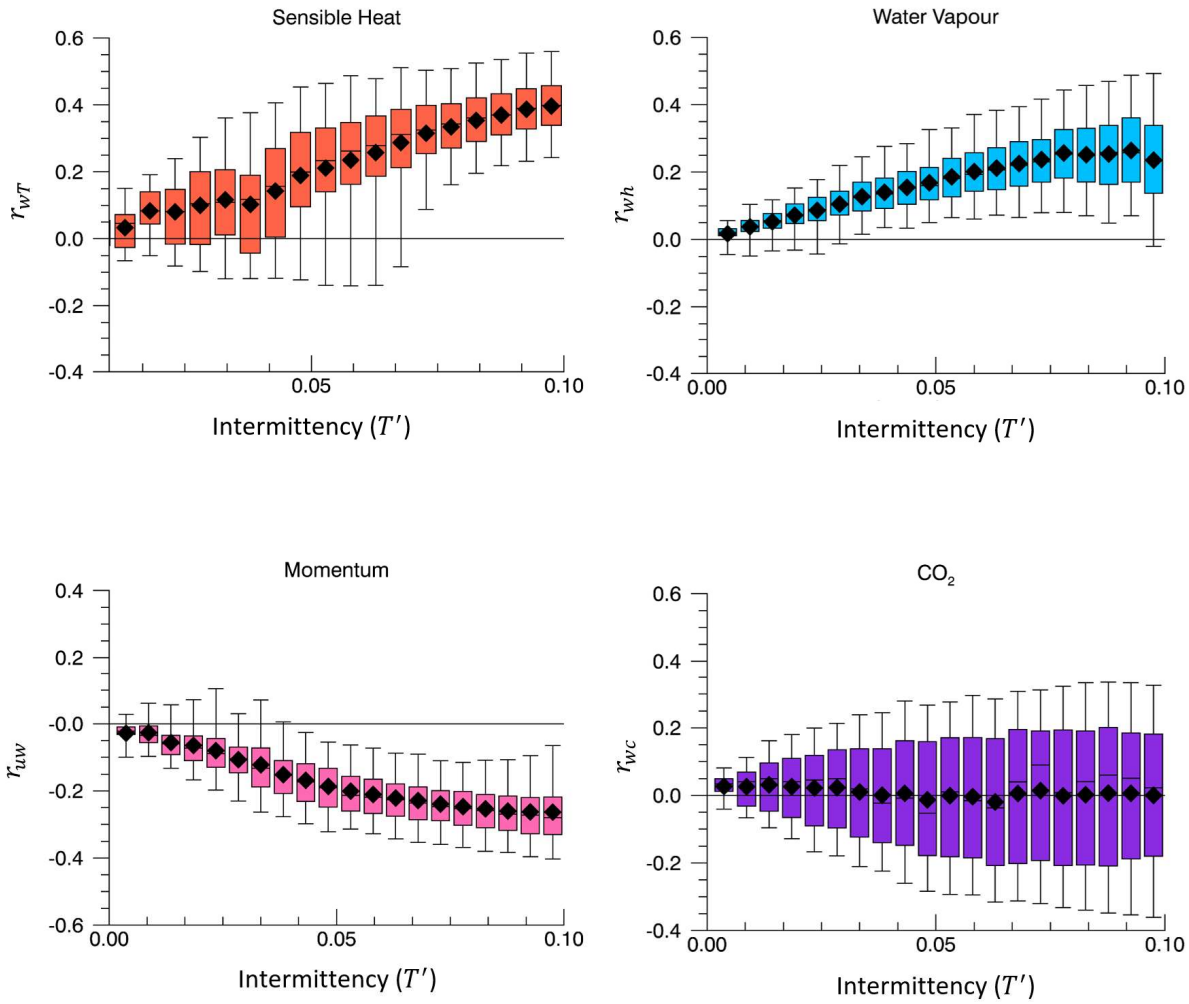

Figure 3.30: The exchange efficiencies, r_{wT}, r_{wh}, r_{uw}, and r_{wc}, versus T', for the day, and the SW wind sector.

Sensible heat exchange shows a nearly linear relationship between transfer efficiency and T'; Low exchange efficiency corresponds with very intermittent flux contributions, while high exchange efficiency corresponds with more continuous exchange. More continuous exchange means more frequent, small-scale contributions to sensible heat flux is occurring, which is expected during the day, as sources of heat at the surface are more uniform. r_{wh} and r_{uw} both show an initial increase with increasingly more continuous contributions from turbulent structures, but diminish at T' values larger than 0.1 (highly continuous exchange). CO_2 exchange efficiency remains consistent with increasing T'.

At night (Figure 3.31), the relationship between r_{wh}, and r_{uw} and T' is the same as the daytime case. For sensible heat, sources of heat at the surface still exist, as the surface cools, but exchange efficiency is close to zero, and is highly intermittent. Large (positive) r_{wT} values are observed to occur even at night, and are associated with more continuous (less intermittent) exchange. This could be the result of building heating in the SW at night. The nighttime trend for CO_2 is clearer, and shows a distinct increase in the upward-directed r_{wc} as T' increases. The discrepancy between the T' values associated with daytime and nighttime CO_2 fluxes and the exchange efficiency of CO_2 can be explained in terms of the characteristics of competing sources and sinks of CO_2. At night, CO_2 exchange is on average toward the atmosphere, as both traffic and anthropogenic and biogenic respiration emit CO_2. But during the day, exchange of CO_2 is both toward the atmosphere (traffic emissions) and toward the surface (photosynthesizing vegetation) in the SW, creating opposing influences on CO_2 flux, which lowers the magnitude of r_{wc}. Thus, the undetectable trend seen in Figure 3.30 suggests that the T' values associated with the CO_2 sinks (photosynthesis) and CO_2 sources (traffic) during the day are similar. This result coincides with the above analysis (Figure 3.29), where distinct sweeping and ejecting motions both contribute to highly efficient CO_2 exchange. In every case, T' values are below 0.1, indicating that exchange is intermittent.

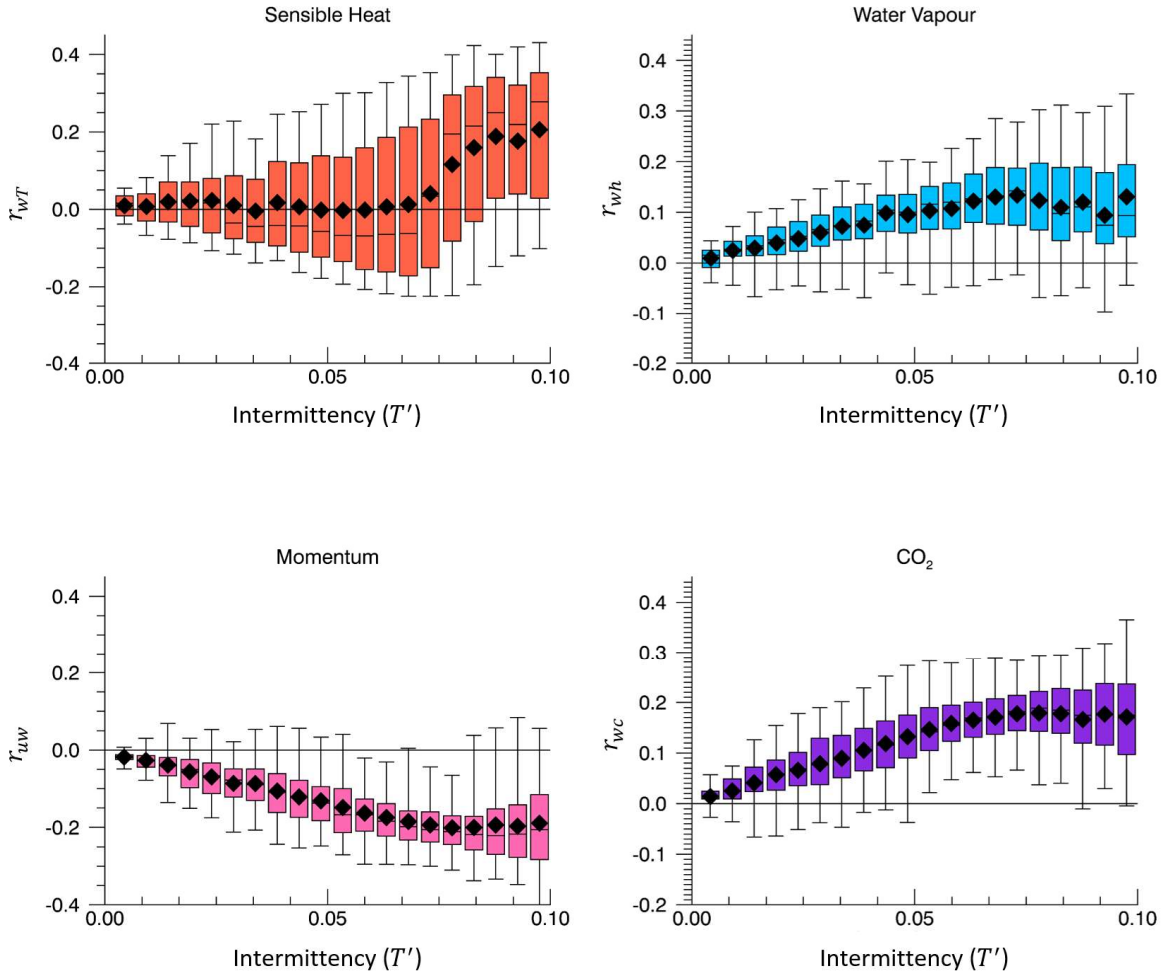

Figure 3.31: The exchange efficiencies, r_{wT}, r_{wh}, r_{uw}, and r_{wc}, versus T', for night, and the SW wind sector.

3.5.3 Surface heterogeneity

ΔS_0 was plotted as a function of wind direction to determine the effects of changing surface properties on turbulent motion (Figure 3.32). For unstable daytime conditions, CO_2 and momentum fluxes are more influenced by changes in surface properties than are water vapour and sensible heat.

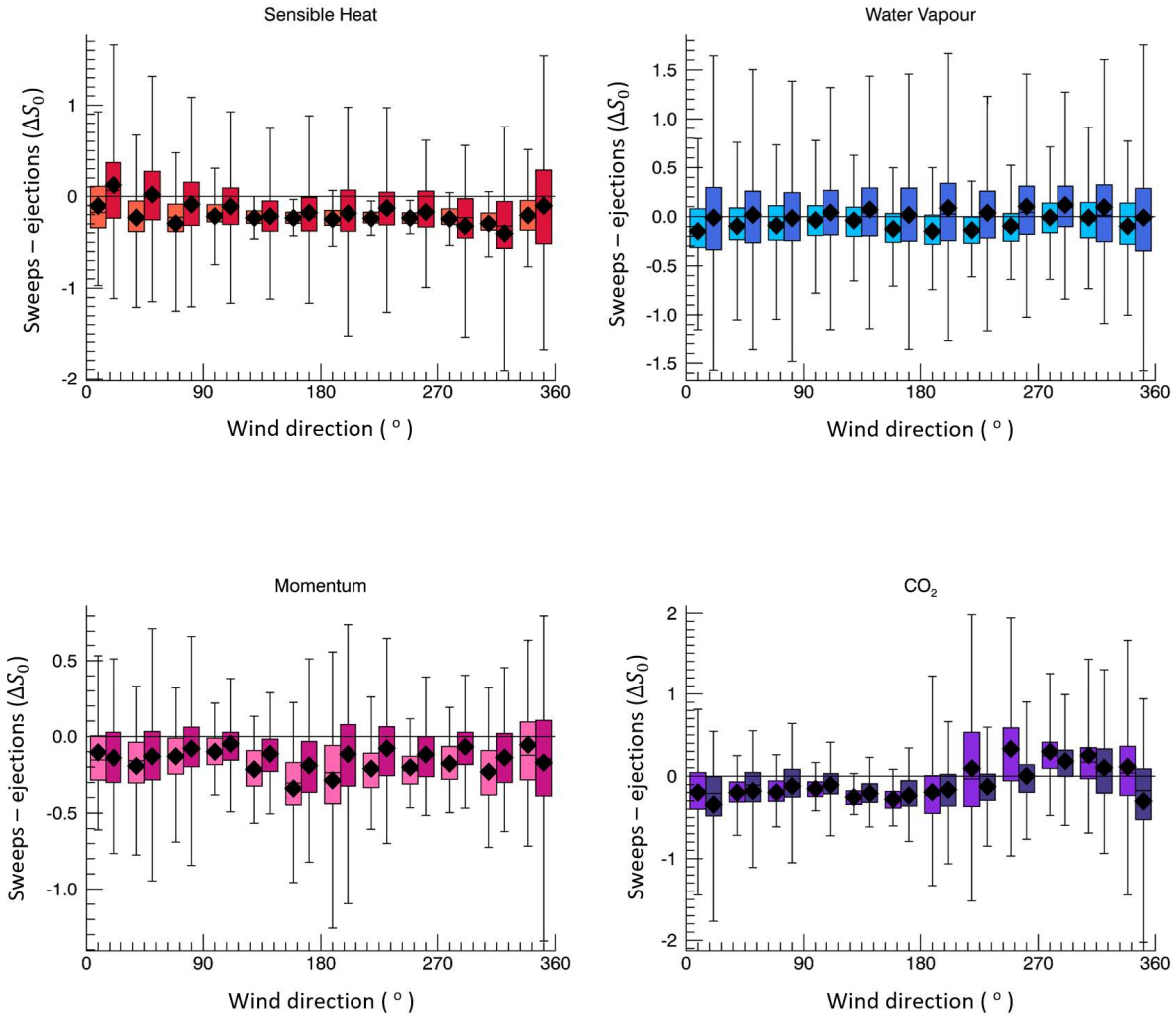

Figure 3.32: The fraction of sweeps – the fraction of ejections for sensible heat, water vapour, momentum, and CO_2, as a function of wind direction, for day and night (all stabilities). Daytime values for sensible heat, water vapour, momentum, and CO_2 are given by the light orange, light blue, pink, and violet boxes, respectively, and nighttime values are denoted by the darker boxes.

Sensible heat exchange is driven by ejections during the day, and to a lesser extent at night, with little variation in the fraction of sweeps and ejections as a function of wind direction. Water vapour similarly exhibits little variation with wind direction, with a very slight exception in the NW, where the daytime ΔS_0 approaches zero.

Momentum exchange remains fairly consistently ejection-dominated, with slight variation as a function of wind direction. To investigate surface characteristics influencing the relative contribution of ejections and sweeps for momentum exchange, ΔS_0 for momentum was plotted against roughness length (Figure 3.33).

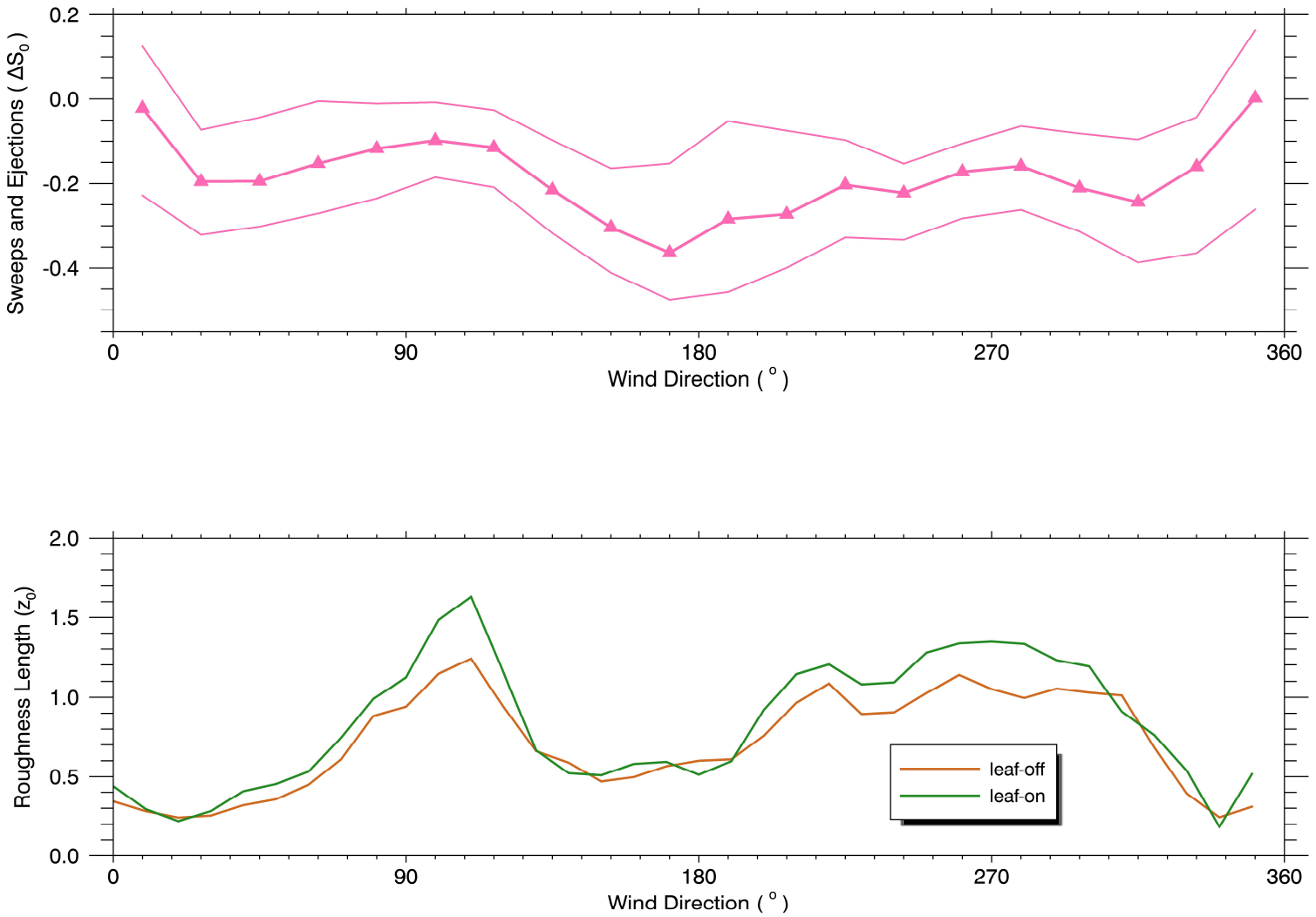

Figure 3.33: ΔS_0 for momentum, and roughness length broken into leaf-on and leaf-off seasons, as a function of wind direction, for daytime conditions (all stabilities). The coloured bands in the top graph represent the 25th and 75th percentiles.

While momentum exchange is ejection-dominated, sweeps become more important over areas of higher roughness, effectively resulting in a ΔS_0 closer to zero. For momentum, sweeps represent the downward transport of high-momentum flows (Christen et al., 2007). Therefore, rougher surfaces lend to enhanced downward movement of momentum, which is further associated with increased momentum exchange efficiency (Figure 3.24 in Section 3.4). While surface roughness in the NW is low, ΔS_0 values nevertheless increase, seemingly contrasting with the overarching trend, but this may be an effect of flow distortion created by the presence of the EC tower itself, as winds from the NW must flow through the tower mast. Smoother surfaces result in a much larger fraction of ejections compared to sweeps. This finding is in keeping with that of previous studies which determined that ΔS_0 for momentum is highly dependent on the roughness of the surface, as well as the density of roughness elements in the source area (Raupach 1981, Rotach 1993).

Daytime ejecting motions are more common for CO_2 in the NE-SE wind sectors, while sweeping motions are more common in the SW-NW. These fluctuations correspond with the spatial mismatch between regions with higher traffic amounts (NE-SE) and regions with large vegetation fractions (SW-NW) (Figure 3.34). During the day, photosynthesis from urban vegetation takes up CO_2, bringing it toward the surface. Conversely, traffic in the NE-SE is responsible for the emission of CO_2 into the atmosphere, producing enhanced upward transport of CO_2 to the atmosphere when energetic thermals transport it. The nighttime trend follows the daytime trend closely for CO_2.

These results suggest that dissimilarities in intermittency and ΔS_0 for heat, mass, and momentum is related to dissimilarities in exchange efficiencies of sensible heat, water vapour, momentum, and CO_2, which was also found to be the case by Wang et al. (2014).

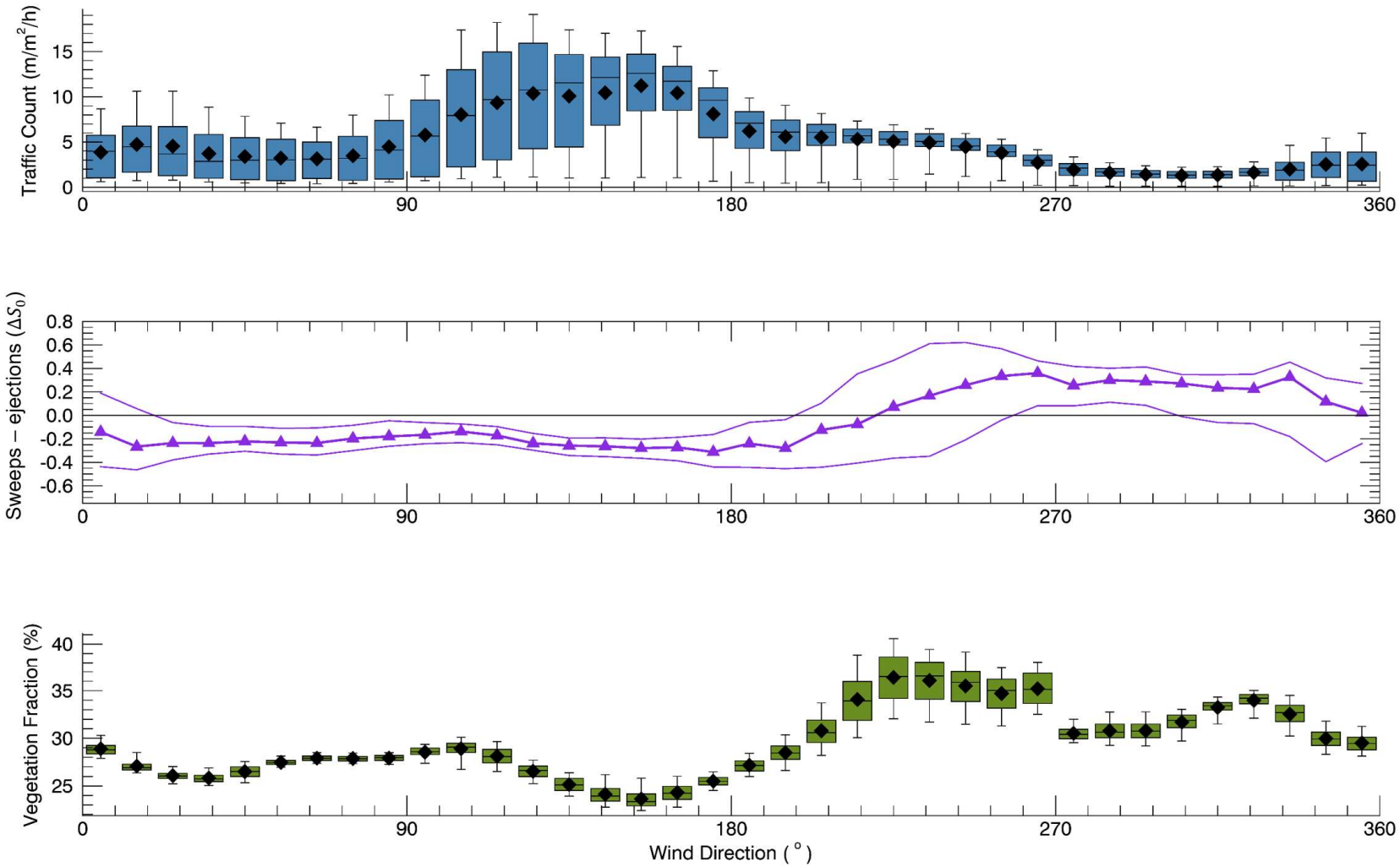

Figure 3.34: ΔS_0 for CO_2 (daytime conditions), footprint-averaged traffic amounts, and vegetation fractions, all plotted against wind direction, considering all stabilities.

3.5.4 Summary of the relationship between organized motion and dissimilar turbulent exchange

1) Under unstable conditions, exchange is dominated by intermittent ejections. T' values of sensible heat exchange are slightly larger than momentum, water vapour, and CO_2. Under near-neutral and stable conditions, the contribution of ejections is comparable to that of sweeps, and exchange is more intermittent than the unstable case. Under stable conditions, the time fraction above which half of the flux occurs is similar for heat, water vapour, momentum, and CO_2.
2) Surface roughness is primarily responsible in determining the relative contribution of sweeps to ejections on momentum fluxes, and spatial and temporal heterogeneity in sources and sinks of CO_2 at the surface greatly affect the fraction of ejections and sweeps acting on CO_2.

Chapter 4: Conclusions

This research sought to investigate and characterize the effects of spatial and temporal source/sink heterogeneity on energy and mass exchange over a complex urban landscape in Vancouver, Canada ("Vancouver-Sunset", Fluxnet ID "Ca-VSu"). This was achieved through combined use of detailed remotely-sensed imagery, geospatially-referenced land cover datasets, modelled flux footprints, and eight years of continuous flux data from an urban eddy covariance (EC) tower. Relationships between exchange efficiencies of sensible heat, water vapour, momentum, and CO_2 were examined diurnally, seasonally, under varied atmospheric stability regimes, and as a function of discrete surface characteristics within the constantly changing turbulent source area. Presented here is a summary of key conclusions:

1) The Monin-Obukhov similarity theory is expected to be valid when predicting values of exchange efficiencies in the inertial sublayer (ISL), as the distance from the complex surface is sufficiently large enough that the effects of individual surface characteristics are averaged away (Al-Jiboori 2008). Flux measurements made at Vancouver-Sunset are within the ISL (Giometto et al., 2017), and therefore MOS-predicted values of sensible heat and momentum exchange should conform to MOS scaling if surface source/sink distributions are homogeneous, or at a much smaller scale than the footprint. Stability analysis demonstrated that under stable conditions, atmospheric stability primarily moderates the exchange of momentum and scalars, with surface heterogeneity of secondary importance due to the larger flux footprint and the existence of a temperature inversion under stable conditions which restricts exchange (Mahrt et al., 1998). In contrast, under neutral and unstable conditions, exchange efficiencies of momentum and scalars are mainly influenced by surface heterogeneity, rather than stability. This result brings into question the reliability of MOS over heterogeneous urban landscapes, even within the ISL.

2) As sources and sinks become more homogeneous in the source area, exchange efficiencies of relevant turbulent entities increase. The opposite is true as increasingly patchy distributions of sources and sinks in the flux footprint result in increasingly less efficient turbulent transport. For example, a patchy distribution of water at the surface during a summertime drought, especially when garden irrigation is restricted, results in a much smaller water vapour exchange efficiency compared to a particularly wet summer.

The effect of spatially and temporally competing sources and sinks acting on a turbulent entity simultaneously is reflected in (although not indicated by) an exchange efficiency closer to zero. For instance, Figure 4.1 shows that during the day, photosynthesis from urban vegetation acts as a net sink of CO_2, increasing the downward-directed (negative) CO_2 exchange efficiency. Daytime traffic emissions, however, act as a CO_2 source, represented by an upward-directed (positive) exchange efficiency. These opposing sources and sinks are characterized by an apparent CO_2 exchange efficiency close to zero for sources areas in which traffic and vegetation coincide.

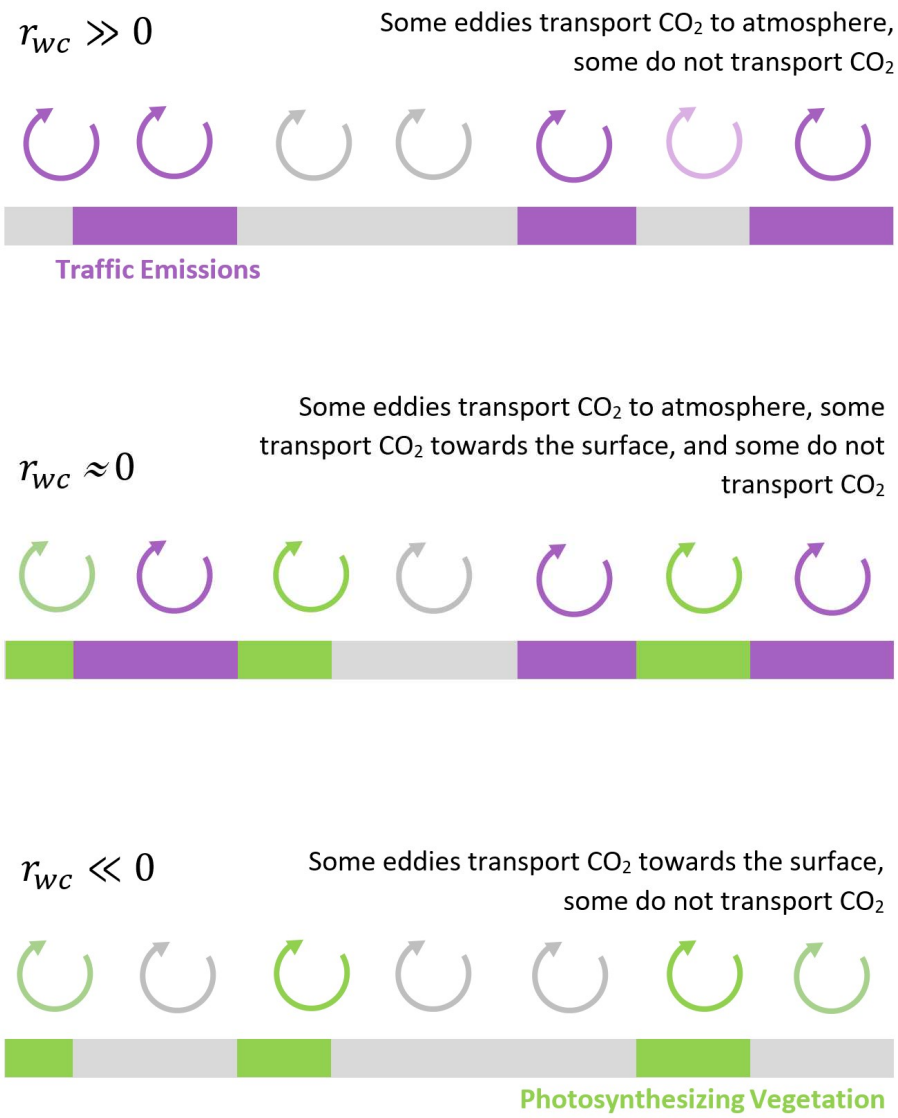

Figure 4.1: Example of how different surfaces with varying levels of source/sink heterogeneity may influence turbulent exchange efficiency of CO_2 (represented by the variable r_{wc}). Photosynthesizing vegetation during the day represents a sink of CO_2 (negative r_{wc} value), and traffic emissions represent a source (positive r_{wc}), while the combined effects result in a net r_{wc} closer to zero (see Section 3.4).

3) Conditional sampling of turbulence affecting momentum and scalar transfer, represented by sweeps, ejections, and flux intermittency, can be related to the same processes that govern dissimilarities between and among momentum and scalar transport efficiencies - namely,

temporal and spatial surface heterogeneity, and atmospheric stability. For example, momentum exchange exhibits sweeping and ejecting tendencies not characteristic of the other turbulent entities as a function of surface roughness; Over areas of high roughness, the fraction of ejections is reduced, and is further associated with an increase in the efficiency of momentum exchange.

4) Very broadly, sensible heat exchange efficiency exhibits dependencies on stability, time of day and year, and surface heterogeneity. Momentum exchange efficiency is mostly affected by atmospheric stability and surface roughness, and both passive scalars, water vapour and CO_2, are chiefly moderated by the patchiness of sources and sinks at the surface, and its diurnal/seasonal fluctuations.

4.1 Limitations

A major weakness in urban eddy covariance studies is the lack of long-term datasets, as these are crucial for resolving seasonal and annual trends in flux data, and permitting data to be rigidly constrained to particular atmospheric and surface conditions. This research utilized eight years of continuous flux data, in conjunction with detailed, satellite and LiDAR-derived gridded geospatial information on the surface characteristics present in the source area. This allowed for thorough analysis of temporally changing stability regimes, the effects of seasonality on surface processes, and subsequent influences on exchange efficiency of momentum and scalars for an urban environment. Nevertheless, limitations exist within this work, and this section will aim to address many of them.

Sunset Tower was erected in 1978 in the "Sunset" neighbourhood of Vancouver, as this area was considered to have a source area most representative of typical Vancouver and North American neighbourhoods, with relatively homogeneous surface characteristics. The presented research, as well as past investigation by Schmid et al. (1991), indicates that the site is not homogeneous, and experiences spatially and temporally changing surface properties, and altered exchanges of energy and gases. To an extent, this is unavoidable in urban areas. However, the representativeness of raw flux data from this site

should be addressed, especially in terms of time, stability, and source area, if it is to be used in dispersion models, air pollution meteorology, or weather forecasting. The methods presented in this research do, however, provide a way of directly linking measured fluxes to surface heterogeneity; Using remotely-sensed surface data and source area models, and applying a quality flag approach like those proposed by Foken and Wichura (1996) and Gockede et al. (2004) would allow flux data quality to be thoroughly assessed.

LiDAR data used in this research was taken at a 1 m resolution, over a domain of 1900 m x 1900 m, centered on the tower. To make use of the footprint model, however, a 2025 m x 2025 m domain with cell resolution of 25 m was needed, so the resolution of the input raster files was reduced from 1m to 25 m, inherently incorporating some filtering as fine-scale differences in discrete land cover fractions were averaged out.

The LiDAR imagery is unable to resolve non-vegetated surface cover types underneath overhanging trees, thus presented vegetation fractions may be overestimated. Additionally, different types of trees and different tree heights will have varying effects on the exchange of momentum and scalars, and this is not accounted for in the land cover data (Christen et al., 2010, Crawford 2014). Traffic count data does not account for differing vehicle or fuel types, but it is known that a large variety of vehicles including small cars and large, cargo-carrying trucks often drive through the source area (Christen et al., 2011). This will influence the relative contribution of traffic-emitted CO_2 fluxes measured at the tower over time, and more generally.

Orography in the study area (and the resulting flow regimes) is not quantitatively accounted for in this work. The existence of cold air drainage flows is speculated to exist, and have an influence on the amount and timing of flux measurements (Crawford and Christen, 2014), but no assessment of this potential contribution was performed in the analysis.

The footprint model used in this research was developed for homogeneous and smoother landscapes, and aside from its ability to account for the displacement height offset resulting from

roughness elements, the model essentially treats the source area as a flat, uniform surface from which flux contributions are equal. This is unrealistic for urban areas, which are comprised of an array of spatially-variable and different-sized roughness elements, street canyons and other aspects of urban morphology that significantly alter surface flows (Christen et al., 2009). This research may lend to the development of footprint models that account for some of these surface characteristics. For example, Hellsten et al. (2015) imbedded a footprint model into a large eddy simulation (LES) model that incorporates some flow heterogeneity, and found that the footprint shape changed significantly compared to the shape the conventional model outputs.

Contributions to surface roughness from large elements are considered in the LiDAR data, but the influence of small roughness elements, such as individual lamp posts or individual trees, remains unresolved. The effects of individual trees and their seasonally-dependent leaf area densities, for example, have been shown to directly affect the dispersion of air pollutants (Giometto et al., 2017). This highlights the need for more intelligent models that are able to interpret individual roughness elements in source area calculations and flux modelling.

4.2 Implications

As eddy covariance studies become more widely-applied to cities, where the majority of people live, and where weather forecasting and pollution dispersion modelling are most important, similarity theories and underlying assumptions of the EC method that do not hold true over heterogeneous environments need to be addressed. This work provides insight into the processes responsible for dissimilarities in momentum and scalar exchange over complex landscapes, and provides a framework from which more thorough quality assessments can be made, and more intelligent models can be built. The work presented here can further serve to better inform air pollution modelling, urban planning, and EC site selection in other cities around the world.

4.3 Further research

1) Long-Term EC Data

This research provides a framework for investigating the effects of temporal and spatial source/sink heterogeneity on urban eddy covariance flux measurements, and advancing our understanding of turbulence over patchy urban landscapes. While maintaining long-term flux data in urban areas is logistically difficult, it is nevertheless essential; Most the world's population lives within cities where a substantial fraction of the global anthropogenic GHG emissions originate (Satterthwaite 2008). In these areas, understanding of the processes that moderate surface-atmosphere exchange is imperative for accurate weather forecasting and pollution dispersion modelling (Roth 2000, Grimmond and Christen 2012). Diurnal and seasonal changes in surface characteristics and processes has been shown to greatly influence turbulent exchange, either through changes in stability regimes, or by introducing spatial heterogeneity. The seasonally-dependent effect of vegetation with leaves on the exchange of momentum is one example of how exchange efficiencies change as a function of time. Long term studies also permit the rigid stratification of flux data into discrete instances of particular conditions (for example, stability, time of year, or wind direction) without losing a representative sample size with which to perform reliable analyses. Therefore, it is encouraged that more urban EC studies span the seasons, and incorporate nighttime into analyses, as instances of stable atmospheric conditions, which are rarer in cities, are not well studied. This may also allow for the study of unorganized, inward and outward interactions of turbulent fluxes, of which few studies have addressed (Katsouvas et al., 2007).

2) Inter-City Representativeness

While the neighbourhood-scale characteristics of this study site are considered representative of most cities in North America, results are not directly applicable to other cities. Future EC studies should take place in areas that are currently underrepresented in the literature, such as those in the Southern Hemisphere (Crawford 2014).

3) Clumping

This research aimed to characterize the effects of source area "patchiness" on flux data, however the effects of "clumping" have not been considered; While a source area may contain a small or large footprint-averaged surface cover fraction, the relative distribution of this fraction within the footprint was not considered. Therefore, future studies should aim to address how the relative proximity and arrangement of surface cover properties in the footprint affect flux measurements. One way this might be accomplished is through the use of plan-area cover values based on variance, rather than mean values. This study calculates the footprint-averaged fraction by multiplying the source area weighting (ϕ) by the total plan-area cover fraction (λ) in each cell, over the entire footprint domain. If, instead, the source area weighting was multiplied by the total λ minus the average λ (the variance of λ), information on whether surface cover properties are more clustered together or more dispersed throughout the footprint could be determined. This would not provide information on where in the footprint "clumping" might be occurring, it would only indicate the extent to which clumping may exist.

4) Fine-Scale Resolution

Surface heterogeneity exists at much finer resolution than is allowed for by the data used in this research. More detailed, high-resolution remote-sensing data, more intelligent footprint models that account for small roughness elements, and more thorough representation of emission sources not herein accounted for would be a tremendous asset (Giometto et al., 2017).

5) "Large Project" Studies

To date, few studies have combined remote-sensing, source area models, and emissions inventory models to evaluate flux measurements and describe turbulent exchange. As heterogeneity exists both spatially and temporally, detailed information on physical urban morphology, in conjunction with temporally changing urban function and emission processes is necessary for accurate assessment of the

factors influencing flux data. More “large project” studies that allow for collaborative efforts between researchers will provide better insight on the influence of urban areas on EC measurements (Grimmond 2006, Barlow et al., 2017).

Bibliography

Al-Jiboori, M. H., Xu, Y., & Qian, Y. (2002). Local similarity relationships in the urban boundary layer. *Boundary-Layer Meteorology, 102*(1), 63-82.

Al-Jiboori, M. H. (2008). Correlation coefficients in urban turbulence. *Boundary-Layer Meteorology, 126*(2), 311-323.

Arnfield, A. J. (2003). Two decades of urban climate research: A review of turbulence, exchanges of energy and water, and the urban heat island. *International Journal of Climatology, 23*(1), 1-26.

Aubinet, M., Vesala, T., Papale, D. (2012). Eddy covariance: A practical guide to measurement and data analysis. *Earth and Environmental Science*. Dordrecht, New York. Springer.

Barlow, J., M. Best, S. Bohnenstengel, P. Clark, S. Grimmond, H. Lean, A. Christen, S. Emeis, M. Haeffelin, I. Harman, A. Lemonsu, A. Martilli, E. Pardyjak, M. Rotach, S. Ballard, I. Boutle, A. Brown, X. Cai, M. Carpentieri, O. Coceal, B. Crawford, S. Di Sabatino, J. Dou, D. Drew, J. Edwards, J. Fallmann, K. Fortuniak, J. Gornall, T. Gronemeier, C. Halios, D. Hertwig, K. Hirano, A. Holtslag, Z. Luo, G. Mills, M. Nakayoshi, K. Pain, K. Schlünzen, S. Smith, L. Soulhac, G. Steeneveld, T. Sun, N. Theeuwes, D. Thomson, J. Voogt, H. Ward, Z. Xie, and J. Zhong, (2017). Developing a research strategy to better understand, observe and simulate urban atmospheric processes at kilometre to sub-kilometre scales. *Bull. Amer. Meteor. Soc*. doi:10.1175/BAMS-D-17-0106.1, in press.

Burba, G., (2013). Eddy Covariance Method for Scientific, Industrial, Agricultural, and Regulatory Applications: A Field Book on Measuring Ecosystem Gas Exchange and Areal Emission Rates. LI-COR Biosciences, Lincoln, NE, USA, 331.

Canadell, J. G., et al. (2009). The human perturbation of the carbon cycle. Paris, France: UNESCO-SCOPE-UNEP.

Cermak, J. E., Davenport, A. G., Plate, E. J. (1995). Wind climate in cities. *English/International Collection (Archive),* Netherlands. Springer.

Chen, B., Coops, N., Fu, D., Margolis, H., Amiro, B., Barr, A., Black, T., et al. (2011). Assessing eddy-covariance flux tower location bias across the Fluxnet-Canada Research Network based on remote sensing and footprint modelling. *Agricultural and Forest Meteorology*, *151*(1), 87–100.

Chen, X., Zhao, H., Li, P., & Yin, Z. (2006). Remote sensing image-based analysis of the relationship between urban heat island and land use/cover changes. *Remote Sensing of Environment, 104*(2), 133-146.

Christen, A., and Vogt, R. (2004). Energy and radiation balance of a central European city. *International Journal of Climatology*, 24: 1395–1421.

Christen, A., van Gorsel, E., Vogt, R. (2007). Coherent structures in urban roughness sublayer turbulence. *International Journal of Climatology, 27*(14), 1955-1968.

Christen A., Crawford B., Goodwin N., Tooke R., Coops N., Grimmond C.S.B., Oke T.R., Voogt J.A. (2009). The EPiCC Vancouver experiment - how do urban vegetation characteristics and garden irrigation control the local-scale energy balance? Proc. of the AMS Eighth Conference on the Urban Environment, Phoenix, AZ, January 11-15, 2009.

Christen, A., Coops N., Kellett R., Crawford B., Heyman E., Olchovski I., Tooke R., van der Laan M. (2010). A LiDAR-based urban metabolism approach to neighbourhood scale energy and carbon emissions modelling. *University of British Columbia, 2010* Technical report prepared for Natural Resources Canada, 104pp.

Christen, A., Coops, N. C., Crawford, B. R., Kellett, R., Liss, K. N., Olchovski, Voogt, J. A. (2011). Validation of modeled carbon-dioxide emissions from an urban neighborhood with direct eddy-covariance measurements. *Atmospheric Environment, 45*(33), 6057-6069.

Christen A., Crawford B., Liss K., Siemens C. (2013). Soil Properties at the Vancouver EPiCC experimental sites. EPiCC Technical Report No. 2, Technical Report of the Department of Geography, University of British Columbia. http://circle.ubc.ca/, 28pp, Version 1.4.

Coceal, O., Dobre, A., Thomas, T. G., & Belcher, S. E. (2007). Structure of turbulent flow over regular arrays of cubical roughness. *Journal of Fluid Mechanics, 589*, 375-409.

Crawford, B. (2014). Measurements of carbon dioxide fluxes and concentrations at multiple scales in Vancouver, Canada. *PhD Thesis in Geography*.

Crawford, B., Christen, A. (2014). Spatial variability of carbon dioxide in the urban canopy layer and implications for flux measurements. *Atmospheric Environment, 98*, 308-322.

Crawford, B., Christen, A. (2015). Spatial source attribution of measured urban eddy covariance CO2 fluxes. *Theoretical and Applied Climatology*, *119*(3-4), 733–755.

DeBruin, H.A.R., Kohsiek, W., & Hurk, v.d., B.J.J.M. (1993). A verification of some methods to determine the fluxes of momentum, sensible heat and water vapour using standard deviation and structure parameter of scalar meteorological quantities. *Boundary-Layer Meteorology, 63*(3), 231-257.

DeBruin, H.A.R, Hurk, v.d., B.J.J.M, & Kroon, L.J.M. (1999). On the temperature-humidity correlation and similarity. *Boundary-Layer Meteorology, 93*(3), 453-468.

Dupont, S., & Patton, E. G. (2012). Momentum and scalar transport within a vegetation canopy following atmospheric stability and seasonal canopy changes: The CHATS experiment. *Atmospheric Chemistry and Physics, 12*(13), 5913-5935.

Famulari, D., Nemitz, E., Marco, C., Phillips, G., Thomas, R., House, E., Fowler, D. (2010). Eddy-Covariance Measurements of Nitrous Oxide Fluxes above a City. *Agricultural and Forest Meteorology,* 150 (6), 786–93.

Feigenwinter, C., Vogt, R., Parlow, E. (1999). Vertical structure of selected turbulence characteristics above an urban canopy. *Theoretical and Applied Climatology, 62*(1), 51-63.

Feigenwinter, C., & Vogt, R. (2005). Detection and analysis of coherent structures in urban turbulence. *Theoretical and Applied Climatology, 81*(3), 219-230.

Feigenwinter et al. (2012). Eddy covariance measurements over urban areas. In: Aubinet, M., Vesala, T., Papale, D., Eddy covariance: A practical guide to measurement and data analysis. *Earth and Environmental Science* (2012th ed.). Dordrecht, New York, 438.

Figueroa-Espinoza, B., & Salles, P. (2014). Local Monin–Obukhov similarity in heterogeneous terrain. *Atmospheric Science Letters, 15*(4), 299-306.

Finnigan, J. J. (1979). Turbulence in waving wheat: II. structure of momentum transfer. *Boundary-Layer Meteorology, 16*(2), 213-236.

Finnigan, J.J., Shaw, R.H., Patton, E.G. (2009). Turbulence structure above a vegetation canopy. *Journal of Fluid Mechanics, 637*, 387-424.

Flesch, T.K. (1996). The footprint for flux measurements, from backward Lagrangian stochastic models. *Boundary-Layer Meteorology* 78, 399-404.

Foken, T., Wichura, B. (1996). Tools for quality assessment of surface-based flux measurements. *Agricultural and forest meteorology* 78(1-2), 83-105.

Foken, T. (2006). 50 years of the Monin–Obukhov similarity theory. *Boundary-Layer Meteorology, 119*(3), 431-447.

Francone, C., Katul, G. G., Cassardo, C., Richiardone, R. (2012). Turbulent transport efficiency and the ejection-sweep motion for momentum and heat on sloping terrain covered with vineyards. *Agricultural and Forest Meteorology, 162-163*, 98-107.

Gao, W., Shaw, R. H., & Paw U, K. T. (1989). Observation of organized structure in turbulent flow within and above a forest canopy. *Boundary-Layer Meteorology, 47*(1-4), 349-377.

Gioli, B., Toscano, P., Lugato, E., Matese, A., Miglietta, F., Zaldei, A., Vaccari, F. P. (2012). Methane and carbon dioxide fluxes and source partitioning in urban areas: The case study of Florence, Italy. *Environmental Pollution*, 164, 125-131.

Giometto, M.G., Christen, A., Egli, P.E., Schmid, M.F., Tooke, R.T., Coops, N.C., Parlange, M.B. (2017). Effects of trees on mean wind, turbulence and momentum exchange within and above a real urban environment. *Advances in Water Resources,* 106, 154-168.

Göckede, M., Rebmann, C., Foken, T. (2004). A combination of quality assessment tools for eddy covariance measurements with footprint modelling for the characterisation of complex sites. *Agricultural and Forest Meteorology, 127*(3), 175-188.

Goodwin, N.R. Coops, N.C, Tooke, R.T., Christen, A., Voogt, J.A (2009). Characterising urban surface cover and structure with airborne LiDAR technology. *Canadian Journal of Remote Sensing*, 35 (3), 297-309.

Grimmond, C. S. B. (1998). Aerodynamic roughness of urban areas derived from wind observations. *Boundary-Layer Meteorology*, 89(1), 1-24.

Grimmond, C. S. B., & Oke, T. R. (2002). Turbulent heat fluxes in urban areas: Observations and a local-scale urban meteorological parameterization scheme (LUMPS). *Journal of Applied Meteorology, 41*(7), 792-810.

Grimmond, S., Salmond, J. A., Oke, T. R., Offerle, B., Lemonsu, A. (2004). Flux and turbulence measurements at a densely built-up site in Marseille: Heat, mass (water and carbon dioxide), and momentum. *Journal of Geophysical Research - Atmospheres, 109*(D24), *D24101.*

Grimmond, S. (2006). Progress in measuring and observing the urban atmosphere. *Theoretical and Applied Climatology, 84*(1), 3-22.

Grimmond, S., Blackett, M., Best, M., Barlow, J., Baik, J., Belcher, S., Bohnenstengel, S., et al. (2010). The International Urban Energy Balance Models Comparison Project: First Results from Phase 1. *Journal of Applied Meteorology and Climatology,* 49(6), 1268–92.

Grimmond, S., Christen, A. (2012). Flux measurements in urban ecosystems. *Fluxletter – The Newsletter of FLUXNET,* 5(1), 1-8.

Hansen, J., Ruedy, R., Sato, M., Imhoff, M., Lawrence, W., Easterling, D., Karl, T. (2001). A closer look at united states and global surface temperature change. *Journal of Geophysical Research, 106*(D20), 23947-23963.

Helfter, C., Tremper, A. H., Halios, C. H., Kotthaus, S., Bjorkegren, A., Grimmond, C. S. B., Nemitz, E. (2016). Spatial and temporal variability of urban fluxes of methane, carbon monoxide and carbon dioxide above london, UK. *Atmospheric Chemistry and Physics Discussions*, 1-31.

Hellsten, A., Luukkonen, S., Steinfeld, G., Kanani-Sühring, F., Markkanen, T., Järvi, L., …. Raasch, S. (2015). Footprint evaluation for flux and concentration measurements for an urban-like canopy with coupled lagrangian stochastic and large-eddy simulation models. *Boundary-Layer Meteorology, 157*(2), 191-217.

IPCC (2013). Climate Change 2013: The Physical Science Basis. Contribution of Working Group I to the Fifth Assessment Report of the Intergovernmental Panel on Climate Change [Stocker, T.F., D. Qin, G.K. Plattner, M. Tignor, S.K. Allen, J. Boschung, A. Nauels, Y. Xia, V. Bex and P.M. Midgley (eds.)]. Cambridge University Press, Cambridge, United Kingdom and New York, NY, USA, 1535.

IPCC (2014). Climate Change 2014: Impacts, Adaptation, and Vulnerability. Part A: Global and Sectoral Aspects. Contribution of Working Group II to the Fifth Assessment Report of the Intergovernmental Panel on Climate Change [Field, C.B., V.R. Barros, D.J. Dokken, K.J. Mach, M.D. Mastrandrea, T.E. Bilir, M. Chatterjee, K.L. Ebi, Y.O. Estrada, R.C. Genova, B. Girma, E.S. Kissel, A.N. Levy, S. MacCracken, P.R. Mastrandrea, and L.L. White (eds.)]. Cambridge University Press, Cambridge, United Kingdom and New York, NY, USA.

Järvi, L., Grimmond, C., & Christen, A. (2011). The surface urban energy and water balance scheme (SUEWS): Evaluation in Los Angeles and Vancouver. *Journal of Hydrology, 411*(3-4), 219-237.

Järvi, L., Nordbo, A., Junninen, H., Riikonen, A., Moilanen, J., Nikinmaa, E., & Vesala, T. (2012). Seasonal and annual variation of carbon dioxide surface fluxes in Helsinki, Finland, in 2006-2010. *Atmospheric Chemistry and Physics,* 12(18), 8475.

Kanda, M. (2005). Large Eddy Simulations on the Effects of Surface Geometry of Building Arrays on Turbulent Organized Structures. *Boundary-Layer Meteorology*. In press.

Kanda, M., & Moriizumi, T. (2009). Momentum and heat transfer over urban-like surfaces. *Boundary-Layer Meteorology, 131*(3), 385-401.

Katsouvas, G. D., Helmis, C. G., & Wang, Q. (2007). Quadrant analysis of the scalar and momentum fluxes in the stable marine atmospheric surface layer. *Boundary-Layer Meteorology*, 124(3), 335-360.

Katul, G., Kuhn, G., Schieldge, J., & Hsieh, C. (1997). The ejection-sweep character of scalar fluxes in the unstable surface layer. *Boundary-Layer Meteorology, 83*(1), 1-26.

Katul, G., Poggi, D., Cava, D., & Finnigan, J. (2006). The relative importance of ejections and sweeps to momentum transfer in the atmospheric boundary layer. *Boundary-Layer Meteorology, 120*(3), 367-375.

Kent, C.W., Grimmond, S., Gatey, D. (2017). Aerodynamic roughness parameters in cities: inclusion of vegetation. *Journal of Wind Engineering and Industrial Aerodynamics*, 169, 168-176.

Kljun, N., Rotach, M. W., & Schmid, H. P. (2002). A three-dimensional backward lagrangian footprint model for A wide range of boundary-layer stratifications. *Boundary-Layer Meteorology, 103*(2), 205-226.

Kordowski, K., Kuttler, W. (2010). Carbon dioxide fluxes over an urban park area. *Atmospheric Environment, 44*(23), 2722-2730.

Kormann R, Meixner F (2001). An analytical footprint model for nonneutral stratification. *Bound Layer Meteorology*, 99(2), 207–224.

Kotthaus, S., Grimmond, S. (2012). Identification of micro-scale anthropogenic CO2, heat and moisture sources – processing eddy covariance fluxes for a dense urban environment. *Atmospheric Environment, 57*, 301-316.

Krayenhoff, E. S., Voogt, J. A. (2007). A microscale three-dimensional urban energy balance model for studying surface temperatures. *Boundary-Layer Meteorology, 123*(3), 433-461.

Roth, M., Oke, T.R. (1993). Turbulent transfer relationships over an urban surface. I. Spectral characteristics. *Quarterly Journal of the Royal Meteorological Society* 119, 1071–1104.

Roth, M., Oke, T.R. (1995). Relative efficiencies of turbulent transfer of heat, mass and momentum over a patchy urban surface. *Journal of the Atmospheric Sciences*, 52, 1863-1874.

Roth, M. (2000). Review of atmospheric turbulence over cities. *Quarterly Journal of the Royal Meteorological Society, 126*(564), 941-990.

Lamaud, E., & Irvine, M. (2006). Temperature–Humidity dissimilarity and heat-to-water-vapour transport efficiency above and within a pine forest canopy: The role of the bowen ratio. *Boundary-Layer Meteorology, 120*(1), 87-109.

Leclerc, M.Y., Shen, S., Lamb, B. (1997). Observations and large-eddy simulation modeling of footprints in the lower convective boundary layer. *Journal of Geophysics,* 102(D8), 9323–9334.

Leclerc, M. Y., Foken, T. (2014). Footprints in micrometeorology and ecology. *Earth and Environmental Science,* (1;2014 ed). Berlin, Heidelberg. Springer.

Leroyer, Sylvie, Stéphane Bélair, Syed Z Husain, and Jocelyn Mailhot. (2014). Subkilometer numerical weather prediction in an urban coastal area: a case study over the Vancouver metropolitan area. *Journal of Applied Meteorology and Climatology* 53 (6): 1433–53.

Li D., Bou-Zeid, E. (2011). Coherent structures and the dissimilarity of turbulent transport of momentum and scalars in the unstable atmospheric surface layer. *Boundary-Layer Meteorology*, 140(2), 243–262.

Liss K., Tooke R., Coops N., Christen, A., (2010). Vegetation Characteristics at the Vancouver EPiCC experimental sites. EPiCC Technical Report No. 3, Technical Report of the Department of Geography, University of British Columbia, 38pp.

Lloyd, C. R. (1995). The effect of heterogeneous terrain on micrometeorological flux measurements: A case study from HAPEX-sahel. *Agricultural and Forest Meteorology, 73*(3), 209-216.

Mahrt, L. (1991). Boundary-layer moisture regimes., 151.

Mahrt, L. (1998). Flux sampling errors for aircraft and towers. *Journal of Atmospheric and Oceanic Technology, 15*(2), 416-429.

Masson, V., Grimmond, S., Oke, T. R. (2002). Evaluation of the town energy balance scheme with direct measurements from dry districts in two cities. *Journal of Applied Meteorology, 41*(10), 1011.

Mazhar, N., Brown, R., Kenny, N., Lenzholzer, S. (2015). Thermal comfort of outdoor spaces in Lahore, Pakistan: Lessons for bioclimatic urban design in the context of global climate change. *Landscape and Urban Planning, 138*, 110-117.

Moriwaki, R., & Kanda, M. (2004). Seasonal and diurnal fluxes of radiation, heat, water vapor, and carbon dioxide over a suburban area. *Journal of Applied Meteorology, 43*(11), 1700-1710.

Moriwaki, R., Kanda, M. (2006). Local and Global Similarity in Turbulent Transfer of Heat, Water Vapour, and CO 2 in the Dynamic Convective Sublayer Over a Suburban Area. *Boundary-Layer Meteorology*, *120*(1), 163–179.

Nelson, M. A., Pardyjak, E. R., Klewicki, J. C., Pol, S. U., & Brown, M. J. (2007). Properties of the wind field within the oklahoma city park avenue street canyon. part I: Mean flow and turbulence statistics. *Journal of Applied Meteorology and Climatology, 46*(12), 2038-2054.

Nordbo, A., Järvi, L., Haapanala, S., Moilanen, J., Vesala, T. (2013). Intra-City Variation in Urban Morphology and Turbulence Structure in Helsinki, Finland. *Boundary-Layer Meteorology*, *146*(3), 469–496.

Nordbo, A., Järvi, L., Vesala, T. (2012). Revised eddy covariance flux calculation methodologies - effect on urban energy balance. *Tellus, B, 64*, 1-20.

Oikawa, S., Meng, Y. (1995). Turbulence characteristics and organized motion in a suburban roughness sublayer. *Boundary-Layer Meteorology* 74, 289–312.

Oke, T.R. (1982). The energetic basis of the urban heat island. *Quarterly Journal of the Royal Meteorological Society* 108, 1–24.

Oke T.R., Mills G., Christen A. and Voogt J.A. (2017). Urban Climates, Cambridge University Press. ISBN 9781107429536.

Park, M.-S., Joo, S. J., Lee, C. S. (2013). Effects of an urban park and residential area on the atmospheric CO2 concentration and flux in Seoul, Korea. *Advanced Atmospheric Science*, 30(2), 503–514.

Paw U, K. T., Brunet, Y., Collineau, S., Shaw, R. H., Maitani, T., Qiu, J., Hipps, L. (1992). On coherent structures in turbulence above and within agricultural plant canopies. *Agricultural and Forest Meteorology, 61*(1), 55-68.

Ramamurthy, P., Pardyjak, E. R. (2015). Turbulent transport of carbon dioxide over a highly vegetated suburban neighbourhood. *Boundary-Layer Meteorology, 157*(3), 461-479.

Raupach, M. R., & Thom, A. S. (1981). Turbulence in and above plant canopies. *Annual Review of Fluid Mechanics, 13*(1), 97-129.

Raupach MR, Coppin PA, Legg BJ. (1986). Experiments on scalar dispersion within a model-plant canopy. I. The turbulence structure. *Boundary-Layer Meteorology* 35, 21–52.

Rotach, M. W. (1993). Turbulence close to a rough urban surface part I: Reynolds stress. *Boundary-Layer Meteorology, 65*(1-2), 1-28.

Rotach, M. W. (1999). On the influence of the urban roughness sublayer on turbulence and dispersion. *Atmospheric Environment, 33*(24), 4001-4008.

Satterthwaite, D. (2008). Cities' contribution to global warming: notes on the allocation of greenhouse gas emissions. *Environ Urban,* 20(2), 539–549.

Schmid, H. P., Cleugh, H. A., Grimmond, C. S. B., & Oke, T. R. (1991). Spatial variability of energy fluxes in suburban terrain. *Boundary-Layer Meteorology, 54*(3).

Schmid, H.P. and T.R. Oke, (1992). Scaling North American urban climates by lines, lanes and rows, *Geographical Snapshots of North America*, Janelle, D.G. (ed.), Guilford Press, New York, 395-399.

Schmid, H. P. (1997). Experimental design for flux measurements: Matching scales of observations and fluxes. *Agricultural and Forest Meteorology, 87*(2), 179-200.

Schmid, H. P., Lloyd, C. R. (1999). Spatial representativeness and the location bias of flux footprints over inhomogeneous areas. *Agricultural and Forest Meteorology, 93*(3), 195-209.

Schmid, H. P. (2002). Footprint modeling for vegetation atmosphere exchange studies: A review and perspective. *Agricultural and Forest Meteorology, 113*(1), 159-183.

Soux, A., Voogt, J. A., Oke, T. R. (2004). A model to calculate what a remote sensor `Sees' of an urban surface. *Boundary-Layer Meteorology, 111*(1), 109-132.

Stewart, I.D., and T.R. Oke, (2009). Newly developed "thermal climate zones" for defining and measuring urban heat island magnitude in the canopy layer. Preprints, T.R. Oke Symposium & Eighth Symposium on Urban Environment, January 11–15, Phoenix, AZ.

Stewart, I. D., & Oke, T. R. (2012). Local Climate Zones for Urban Temperature Studies. *Bulletin of the American Meteorological Society, 93*(12), 1879.

Steyn, D.G. (1992). Micro- and mesoclimatology. *Progress in Physical Geography,* 16, 101-105.

Steyn, D., Faulkner, D. (1986). The climatology of sea-breezes in the lower Fraser Valley. *Climatology Bull.* 20(3), 21–39.

Stull, R. B. (1988). An introduction to boundary layer meteorology. *English/International Collection (Archive),* Dordrecht, Boston. Kluwer Academic Publishers. Springer.

Taylor, G.I. (1938). The spectrum of turbulence. *Proc R Soc Lond,* A164(919), 476-490.

Tooke, T., Coops, N., Goodwin, N., and Voogt, J. (2009). Extracting urban vegetation characteristics using spectral mixture analysis and decision tree classifications. Remote Sensing of Environment, 113(2):398–407.

Twine, T. E., Kustas, W. P., Norman, J. M., Cook, D. R., Houser, P. R., Meyers, T. P., Wesely, M. L. (2000). Correcting eddy-covariance flux underestimates over a grassland. *Agricultural and Forest Meteorology, 103*(3), 279-300.

UN (2014). World Urbanization Prospects, the 2014 Revision. http://esa.un.org/unpd/wup/highlights/wup2014-highlights.pdf. Accessed 8 November 2015.

Van der Kamp, D., & McKendry, I. (2010). Diurnal and seasonal trends in convective mixed-layer heights estimated from two years of continuous ceilometer observations in Vancouver, BC. *Boundary-Layer Meteorology, 137*(3), 459-475.

van der Laan M, Tooke R., Christen A., Coops N., Heyman E., Olchovski I. (2010). Statistics on the built infrastructure at the Vancouver EPiCC experimental sites. EPiCC Technical Report No. 4, 30pp.

van der Laan, M. (2011). Scaling urban energy use and greenhouse gas emissions through LiDAR. Master's thesis, University of British Columbia.

Velasco, E., Roth, M. (2010). Cities as Net Sources of CO2: Review of Atmospheric CO2 Exchange in Urban Environments Measured by Eddy Covariance Technique. *Geography Compass*, *4*(9), 1238–125.

Vesala, T., Kljun, N., Rannik, Ü., Rinne, J., Sogachev, A., Markkanen, T., Leclerc, M. Y. (2008). Flux and concentration footprint modelling: State of the art. *Environmental Pollution, 152*(3), 653-666.

Voogt, J. A., & C S B Grimmond (2000). Modeling surface sensible heat flux using surface radiative temperatures in a simple urban area. *Journal of Applied Meteorology, 39*(10), 1678.

Walsh C (2005). Fluxes of radiation, energy, and carbon dioxide over a suburban area of Vancouver, Master's thesis. Department of Geography, University of British Columbia.

Wang, L., Li, D., Gao, Z., Sun, T., Guo, X., & Bou-Zeid, E. (2014). Turbulent transport of momentum and scalars above an urban canopy. *Boundary-Layer Meteorology, 150*(3), 485-511.

Zhao, Z., Gao, Z., Li, D., Bi, X., Liu, C., & Liao, F. (2013). Scalar Flux–Gradient relationships under unstable conditions over water in coastal regions. *Boundary-Layer Meteorology, 148*(3), 495-516.

Appendices

Appendix A Entrainment analysis

MOS predicts that sensible heat and water vapour should be transferred with equal efficiency in the ISL, but the results presented in this thesis indicate that assumption of MOS do not necessarily hold true over cities, as a result of the dissimilar behaviour of momentum and scalars (and between scalars) under different atmospheric stabilities, and as a result of spatial heterogeneity in the distribution of sources and sinks at the surface (Roth and Oke 1995). In particular, dissimilarities between the efficiency of water vapour and sensible heat exchange have been the focus of many urban studies and, aside from the effects of surface patchiness, the potentially important role of entrainment in the r_{wh} and r_{wT} decorrelation has been highlighted.

Entrainment is the process whereby highly energetic thermals are able to penetrate the capping inversion, transporting warm, dry air from above toward the surface. A number of studies have compared correlation coefficients of water vapour to sensible heat (Mahrt 1991, DeBruin et al., 1993, Roth and Oke 1995, DeBruin et al., 1999, Lamaud and Irvine 2006, Detto et al., 2008) in order to examine the possible influence of entrainment on the relative transfer of these turbulent entities, rather than attributing all dissimilarity to stability and surface heterogeneity.

Roth and Oke (1995) observed that decorrelation between heat and water vapour exchange (attributable mostly to a decrease in r_{wh}) was in part due to large, thermally-produced eddies that penetrated the capping inversion, and brought warm, dry air from the mixed layer toward the surface, which is common in well-developed convective cells (Stull 1988). They found that this entrained air from above accounted for, and drove most of the evaporation occurring at the surface, an observation for which low r_{wh} values were associated.

DeBruin et al. (1993) found that dry surface conditions led to buoyancy-driven, large eddy production, especially over cities, as the presence of large roughness elements increases the displacement height. Detto et al. (2008) investigated the effects of dry and wet surface conditions on the exchange efficiency of water vapour, and found that when soil moisture is low, r_{wh} decreased substantially, leading to a decorrelation between sensible heat and water vapour exchange. Figure 3.22 in Section 3.4 shows that at low soil volumetric water content, r_{wT} is efficiently exchanged, while r_{wh} is decreasingly efficient. Mahrt (1991) suggested that when surface evaporation is weak (a lack of water sources at the surface), entrainment is more likely to occur, and subsequent decorrelation between r_{wT} and r_{wh} is found.

Lamaud and Irvine (2006) presented evidence of the possibility of entrainment via analysis of the Bowen ratio, rather than soil moisture. The Bowen ratio, given by Equation 7, represents the ratio of sensible heat flux to latent heat flux. They found that for Bowen ratio values < 1, MOS generally holds true (r_{wT} and r_{wh} are transferred with similar ease). However, as the Bowen ratio increases, as is often found to be the case over cities, they found that r_{wT} increased significantly, while r_{wh} varied little. Figure A.1 shows r_{wT} and r_{wh} as a function of the Bowen ratio.

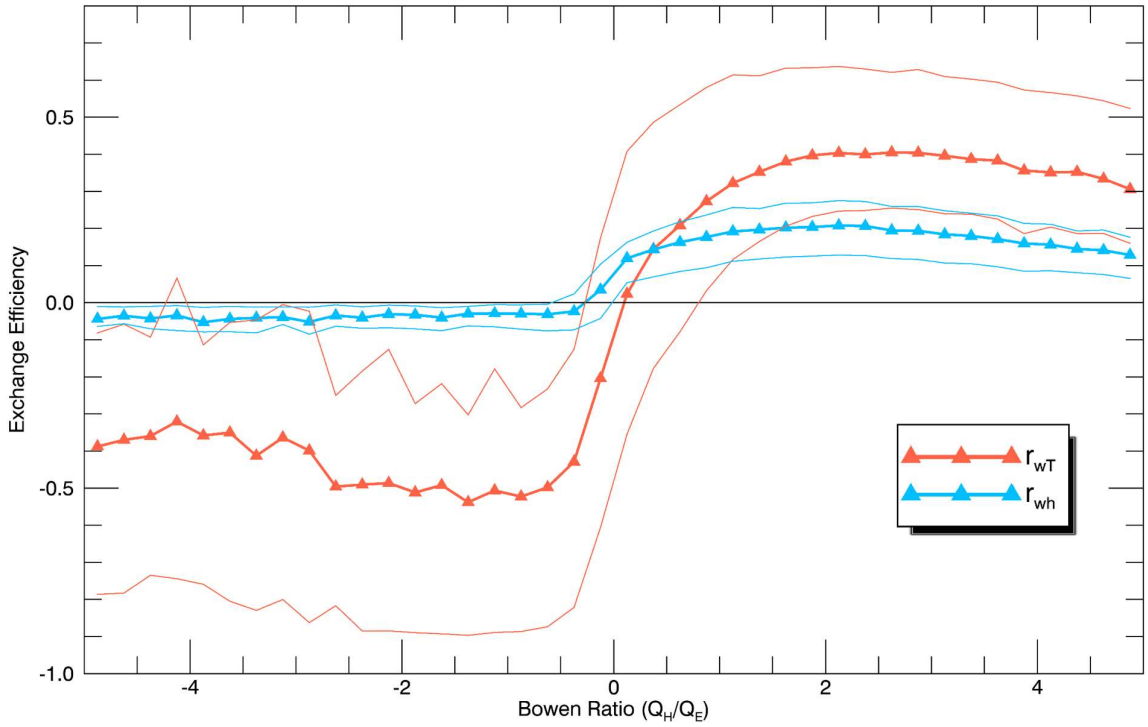

Figure A.1: The mean exchange efficiencies of sensible heat and water vapour as a function of the Bowen ratio, measured at Vancouver-Sunset. The thinner coloured bands represent the 25th and 75th percentiles.

While r_{wh} varies very little with the Bowen ratio, sensible heat exchange increases significantly with increases in the Bowen ratio. This supports the observation made by Lamaud and Irvine (2006) over a forest canopy.

Roth and Oke (1995) note that when the correlation coefficient of temperature and humidity (r_{Th}, see Equation 12) is close to unity, the characteristics of r_{wT} and r_{wh} are similar, but at low r_{Th} values, r_{wh} is small. De Bruin et al. (1999) similarly found r_{Th} is more likely to be negative when the Bowen ratio is large. And Lamaud and Irvine (2006) noticed that r_{Th} tends to increase slightly when the Bowen ratio less than 1, but then steadily decreases for Bowen ratios greater than 1 (see Figure A.2). The decrease in the positive r_{Th} value is similarly hypothesized to be the result of entrainment processes (Mahrt 1991).

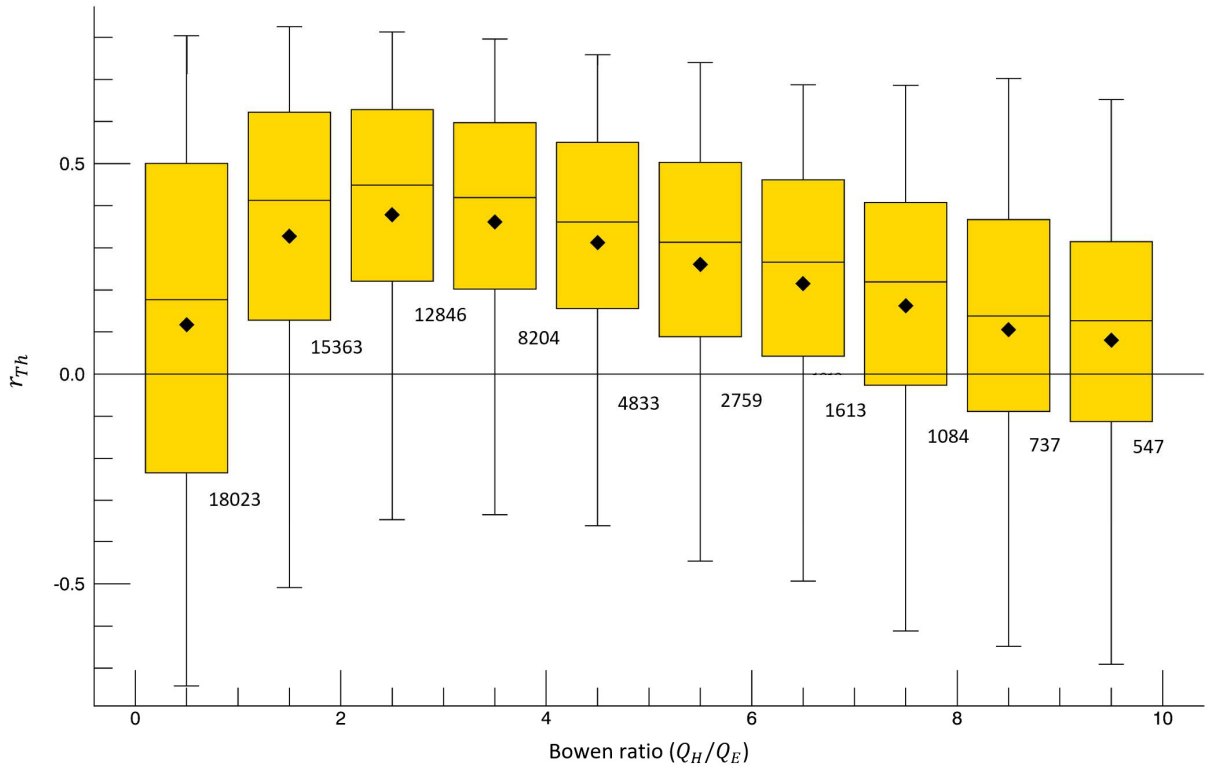

Figure A.2: The correlation coefficient of temperature and humidity (r_{Th}) as a function of the Bowen ratio for the eight years of flux data from Vancouver-Sunset. The values under each box reflect the number of data points within the corresponding box and whiskers.

Figure A.2 shows the correlation coefficient of temperature and humidity (r_{Th}) as a function of the Bowen ratio. The figure confirms both findings by De Bruin et al. (1999) and Lamaud and Irvine (2006), and indicates that entrainment may be acting as a source of sensible heat, and depleting water at the surface.

Roth and Oke (1995) determined that dry surface conditions are observed at a Bowen ratio of approximately 2 for the Vancouver-Sunset study area. Figure A.1 shows a clear decorrelation between r_{wT} and r_{wh} at a Bowen ratio of 2, and Figure A.2 shows that r_{Th} begins steadily decreasing as the Bowen ratio > 2. Thus, as surfaces become dryer, r_{wT} and r_{wh} are exchanged with increasingly dissimilar efficiency, and r_{Th} values subsequently decrease. The increased ΔS_0 for water vapour relative to sensible

heat observed under unstable conditions (Figure 3.32 in Section 3.5), when buoyantly-produced, large eddies may penetrate the capping inversion, may suggest that sweeps (downward-moving moisture-depleted air) are enhancing evaporation at the surface, and increasing the heterogeneity in the distribution of water sources at the surface, which manifests in a decorrelation between r_{wT} and r_{wh}.

While results presented here do not confirm the existence of entrainment processes, it does complement results found by previous studies on the subject. Entrainment may be indirectly contributing to dissimilar exchange of sensible heat and water vapour by depleting sources of water at the surface, increasing surface heterogeneity, and consequently affecting the reliability of MOS predictions of scalar unity.

Appendix B Supplementary material

Figure B.1 shows that, under stable conditions, the footprint-averaged surface cover fractions change very little in magnitude and direction compared to the unstable case (Figure 3.1), despite the size and orientation of the source area changing under stable and unstable conditions. Notably, traffic amounts show the most variation, however small, compared to the unstable case; Mean and median traffic amounts decrease by about 5 m (driven) m^{-2} h^{-1} in the SE sector compared to unstable conditions. This is attributable to the fact that stable atmospheric conditions primarily occur at night, when the number of vehicles moving through the source area has reduced.

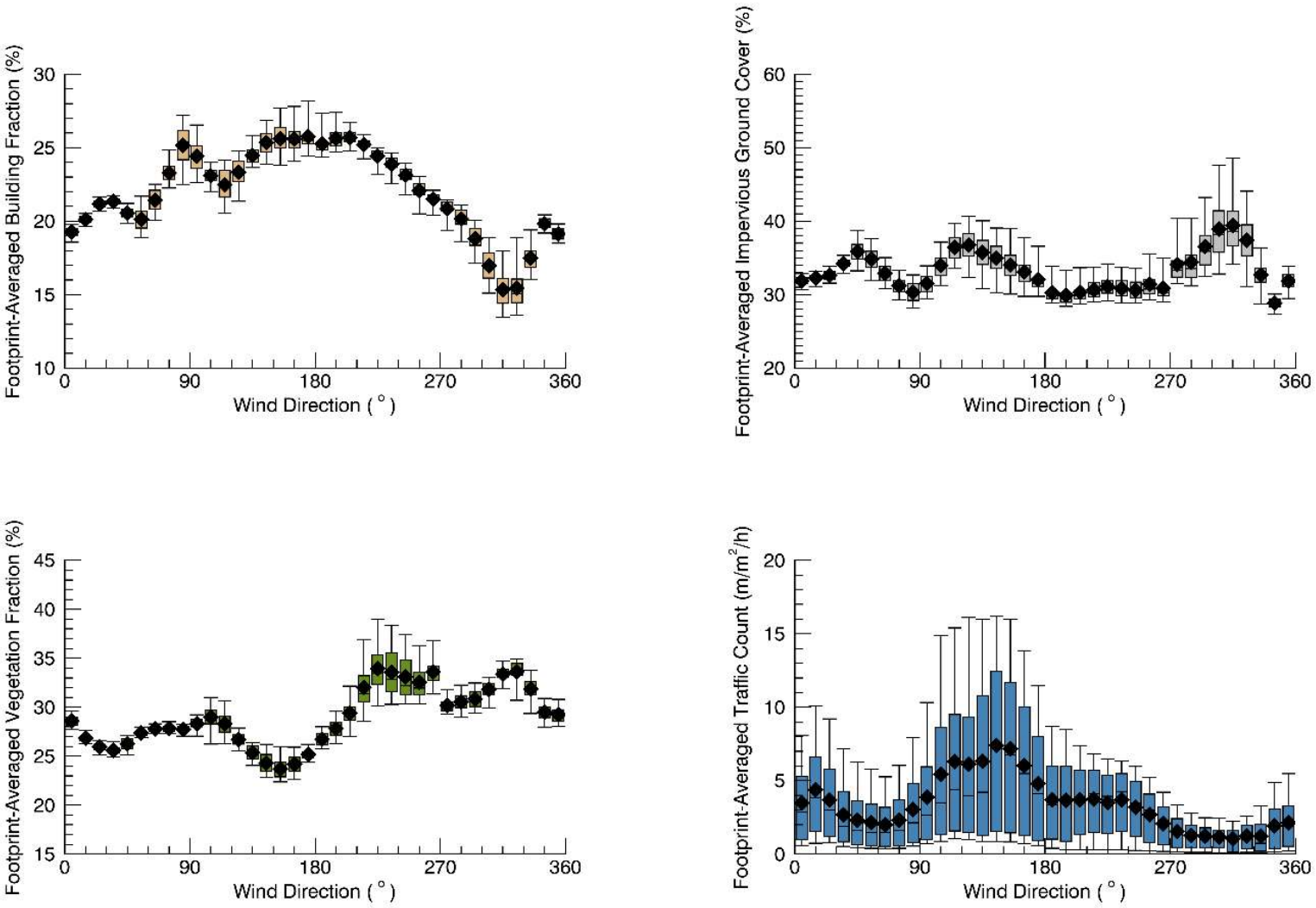

Figure B.1: Footprint-averaged land-cover fractions and traffic amounts as a function of wind direction, for stable conditions ($z'/L > 0.1$).

Figure B.2 (a, b, and c) shows the trend in exchange efficiencies of sensible heat, water vapour, momentum, and CO_2 for stable and unstable, as well as the MOS-predicted values of r_{uw} and r_{wT} from Roth (2000) and Oke et al. (2017) (the overlaid gray lines). For the unstable case, the sign of r_{uw} has been reversed for better comparison.

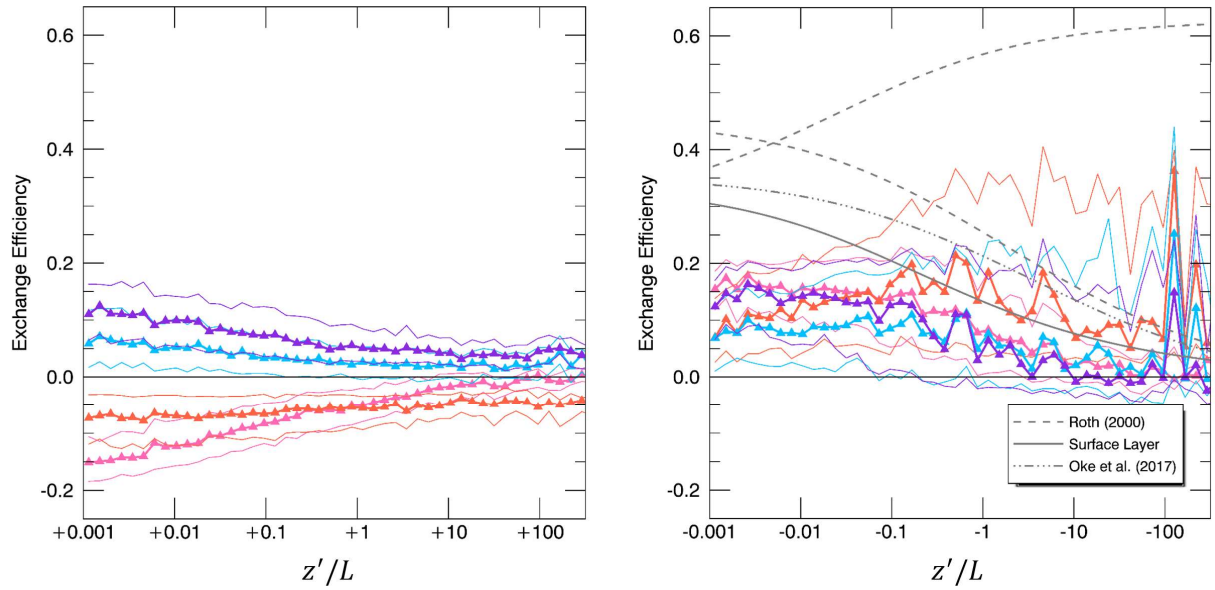

Figure B.2 (a): Median r_{wT}, r_{wh}, r_{uw}, and r_{wc} (given by the bold orange, light blue, pink, and violet lines, respectively) versus stability, for stable (left) and unstable (right) conditions, for the NE wind sector. The thinner coloured bands represent the 25th and 75th percentiles.

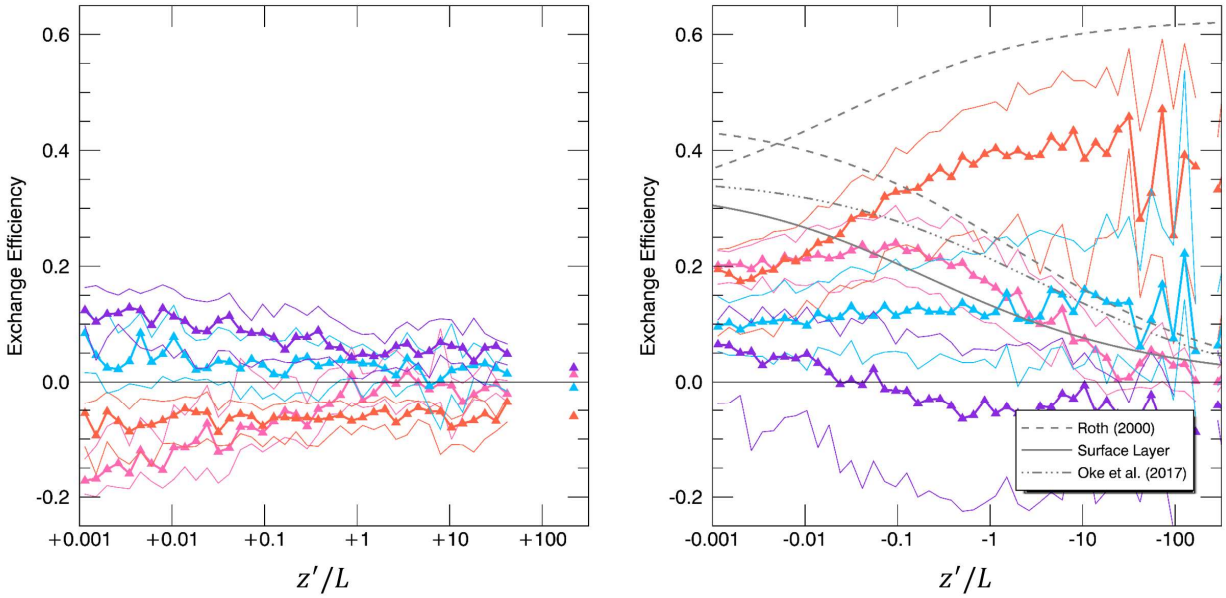

Figure B.2 (b): Median r_{wT}, r_{wh}, r_{uw}, and r_{wc} (given by the bold orange, light blue, pink, and violet lines, respectively) versus stability, for stable (left) and unstable (right) conditions, for the NW wind sector. The thinner coloured bands represent the 25th and 75th percentiles.

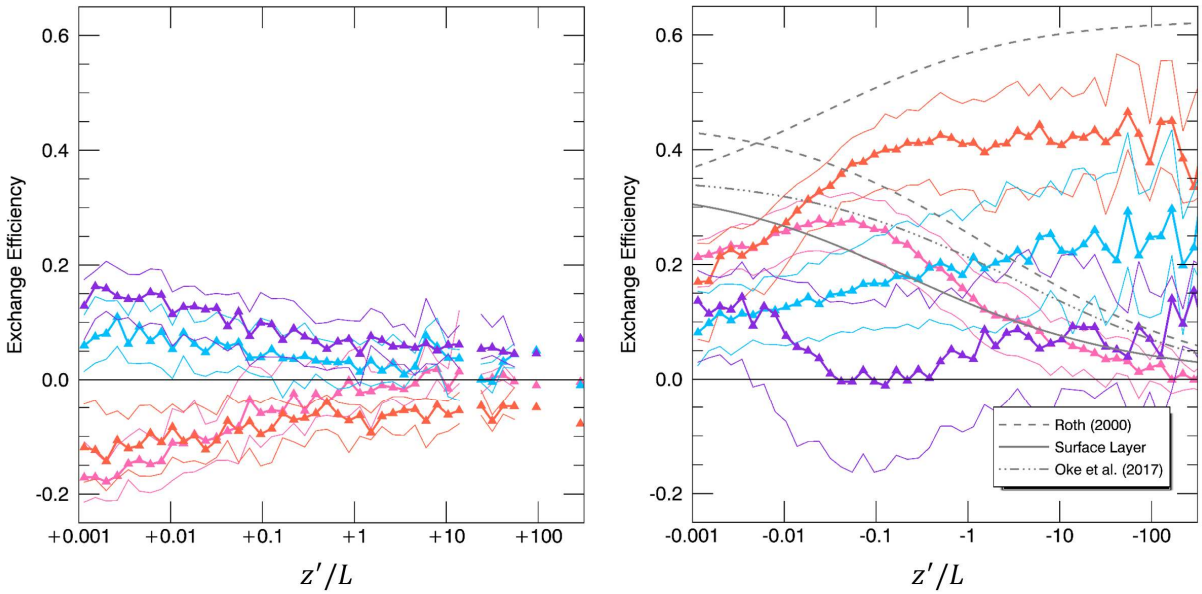

Figure B.2 (c): Median r_{wT}, r_{wh}, r_{uw}, and r_{wc} (given by the bold orange, light blue, pink, and violet lines, respectively) versus stability, for stable (left) and unstable (right) conditions, for the SW wind sector. The thinner coloured bands represent the 25th and 75th percentiles.

Under stable conditions, the exchange efficiencies of momentum and scalars shows the same trend with stability for each of the wind sectors. Greater variation is observed in for the unstable case, especially in the NE (B.2 a) where exchange of all four turbulent entities have similarly low efficiency values, and follow the same trend with stability. Winds typically occur from the NE sector at night, when sensible heat and water vapour exchange efficiencies are lowest. The empty gravel lot present from this direction also significantly reduces momentum exchange efficiency. CO_2 exchange efficiency, while low, remains fairly consistent in this wind sector compared to the SE wind sector. The decrease in CO_2 exchange efficiency in the NW and SW sectors under unstable conditions results from the large fraction of vegetation, which enhances the downward transport of CO_2 during daytime photosynthesis.